Chapter 9
Multiphase and Multicomponent Flows

Abstract After reading this chapter, you will be able to expand lattice Boltzmann simulations by including non-ideal fluids, using either the free-energy or the Shan-Chen pseudopotential method. This will allow you to simulate fluids consisting of multiple phases (e.g. liquid water and water vapour) and multiple components (e.g. oil and water). You will also learn how the surface tension between fluid phases/components and the contact angle at solid surfaces can be varied and controlled.

We start by introducing the physical basis of multiphase and multicomponent flows in Sect. 9.1. In particular, we cover the concepts of the order parameter, surface tension, contact angle and thermodynamic consistency, and we discuss the differences between sharp and diffuse interface models. We then introduce and analyse two popular classes of LB multiphase and multicomponent models: the free-energy model in Sect. 9.2 and the pseudopotential (or Shan-Chen) model in Sect. 9.3. Section 9.2 and Sect. 9.3 can be read independently, but the prior study of Sect. 9.1 is strongly recommended. In Sect. 9.4 we will discuss limitations and extensions of both models, e.g. how to increase the range of physical parameters and how to improve accuracy and numerical stability. Finally, in Sect. 9.5, we provide a few example applications demonstrating the usefulness and suitability of LB multiphase and multicomponent methods.

There exist even more LB methods for multiphase and multicomponent problems. We cannot review all of them here. The most popular of those methods is the colour method [1–6]. Being rooted in lattice gas automata, the colour method is in fact the earliest multicomponent extension to the LBM. Other multiphase and multicomponent methods have also been suggested, e.g. [7–10].

Apart from reading this chapter, we recommend the study of a number of recent articles. Scarbolo et al. [11] developed a unified framework to analyse the similarities and differences of the free-energy and the Shan-Chen models. Chen et al. [12] performed a critical and topical review of the Shan-Chen method. Liu et al. [13] provide an extensive overview of the colour, the Shan-Chen and the free-energy models. The book by Huang, Sukop and Lu [14] is also dedicated to multiphase LB methods.

T. Krüger et al., *The Lattice Boltzmann Method*, Graduate Texts in Physics,
DOI 10.1007/978-3-319-44649-3_9

9.1 Introduction

One of the most popular applications of the LBM is simulating *multiphase* and *multicomponent* flows.

Multiphase and multicomponent flows refer to flows comprising two (or more) different fluids which differ by their physical properties, such as density, viscosity, conductivity *etc.* For single-component multiphase flows, the liquid and gas phases of the same substance are in coexistence. These two phases can interconvert from one to another: the gas can condense to form more liquid, and the liquid can evaporate. A typical example is liquid water and water vapour. Contrarily, multicomponent flows contain two (or more) different substances, for example water and oil. In a multicomponent flow, the substances do not interconvert. Instead, we have to account for the diffusion between these components.

Multiphase and multicomponent flows are important for a wide range of applications [15]. For example, emulsions are formed when one attempts to mix several immiscible liquids [16]. This is ubiquitously exploited in the food, pharmaceutical and personal care industries. Other examples include enhanced oil recovery [17], high-performance heat exchangers [18], polymer processing [19] and microfluidics [20].

In practice, the distinction between multiphase and a multicomponent flows can be quite blurry. Many flows are in fact a mixture between the two, where the liquid and gas phases can separately comprise of several components. One example is cooking: boiling water (liquid water and water vapour) with olive oil. In cases where there is no transfer of material between the different fluid domains and inertia plays a negligible role (e.g. low Reynolds number flow), equivalent results are obtained whether we are using a single-component multiphase or a multicomponent model [21], assuming the material parameters (e.g. viscosity, surface tension, *etc.*) used in the two types of simulations are equivalent. In this chapter, we will focus on two-phase and two-component flows, but not a mix between them.

To distinguish the two fluid phases in a multiphase flow, or similarly the two components in a multicomponent flow, we introduce a concept called the *order parameter*.[1] For multiphase flows, this order parameter is the fluid density. The gas and liquid phases are uniquely characterised by their values of density ρ_g and ρ_l.

For multicomponent flows, density is often not a suitable parameter. For example, the densities of water and oil are quite similar. Instead, a more effective order

[1]This concept can easily be extended to systems with more than two components by introducing more order parameters.

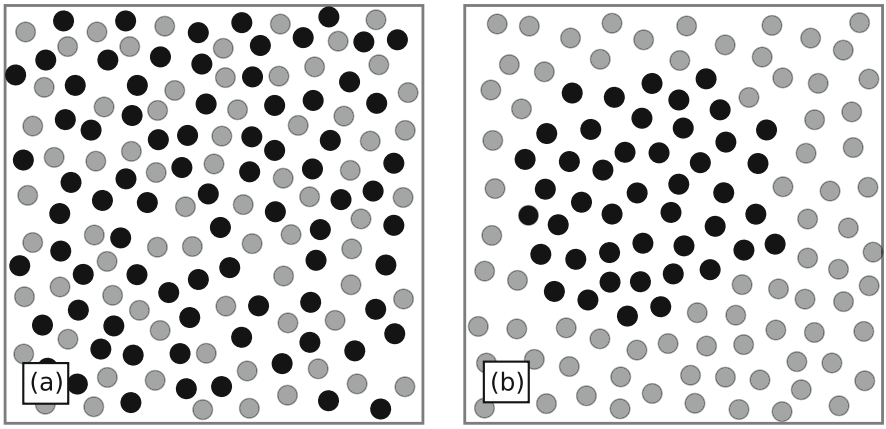

Fig. 9.1 Illustrations of binary fluid mixtures which are (**a**) miscible and (**b**) immiscible. In (**b**), the fluid particles separate into regions which are black-rich and grey-rich. At the interface, the black (grey) particles lose favourable interactions with black (grey) particles and gain less favourable interactions with grey (black) particles, resulting in an excess energy for forming the interface

parameter ϕ is given by

$$\phi = \frac{\rho^{(1)} - \rho^{(2)}}{\rho^{(1)} + \rho^{(2)}} \tag{9.1}$$

where $\rho^{(1)}(\boldsymbol{x}, t)$ and $\rho^{(2)}(\boldsymbol{x}, t)$ are the local densities of components 1 and 2. We denote the densities of the pure components $\rho_{\mathrm{b}}^{(1)}$ and $\rho_{\mathrm{b}}^{(2)}$. These values are also called *bulk densities*. The two *bulk phases* correspond to cases where (i) $\rho^{(1)} = \rho_{\mathrm{b}}^{(1)}$, $\rho^{(2)} = 0$ and (ii) $\rho^{(1)} = 0$, $\rho^{(2)} = \rho_{\mathrm{b}}^{(2)}$, respectively.[2] It is easy to verify that this leads to two distinct bulk values for the order parameter:

$$\phi = \begin{cases} +1 & \text{for component 1,} \\ -1 & \text{for component 2.} \end{cases} \tag{9.2}$$

Multicomponent fluids, i.e. systems comprising different fluids, can be *miscible* or *immiscible*. Miscible fluids can form a completely homogeneous mixture without internal interfaces, as illustrated in Fig. 9.1a. For example, ideal gases are always miscible. Water and ethanol are also miscible, at least over a wide range of

[2] In reality we cannot write $\rho^{(1)} = 0$ or $\rho^{(2)} = 0$ since the local density of a given component is never exactly zero. For example, in a water-oil mixture, one can always find a few water molecules in the oil-rich phase and the other way around. However, these minority densities are usually so small that we can neglect them here.

concentrations. Immiscible fluids, however, are characterised by inhomogeneity. One example is an oil-water mixture that forms some regions that are rich in oil and others that are rich in water. These regions are separated by internal interfaces that are characterised by surface tension, as shown in Fig. 9.1b.

9.1.1 *Liquid-Gas Coexistence and Maxwell Area Construction Rule*

When dealing with a multiphase system, such as liquid water and water vapour, the key question is what the condition for liquid-vapour equilibrium is. How are the liquid and vapour (gas) densities ρ_l and ρ_g related? And how does the pressure depend on the densities?

In nature we observe many situations with coexisting fluid phases or components. The physical requirement of having coexisting phases or components puts a constraint on the **equation of state**, which describes a complex interdependency between pressure p, molar volumes υ (alternatively: density $\rho \propto 1/\upsilon$) and order parameter ϕ for a given temperature T. (We introduced the concept of equations of state in Sect. 1.1.3.) The equation of state $p = p_\mathrm{b}(\rho, \phi, T, \ldots)$ uniquely defines the bulk (i.e. the region not close to any interface) thermodynamic state of the multiphase and multicomponent system.

Let us now focus on one of the most commonly used equations of state, namely the *van der Waals equation* for a liquid-vapour system, shown in Fig. 9.2. We can see that the pressure-molar volume curve has a minimum and a maximum. Any equation of state that displays this property allows for two coexisting bulk fluids. In fact, the thermodynamic states between these two extrema are unstable. If the system is prepared at any of these intermediate states, it will spontaneously phase separate into liquid and gas domains [22]. For a given pressure p_0, the molar volumes of the liquid and gas phases are, respectively, υ_l and υ_g.

From Fig. 9.2, we see that there is a range of pressures for which two distinct molar volumes υ can be adopted for the same bulk pressure value p_b. To decide which exact pressure value the system will adopt (i.e. which p_0 the system will relax to) and, correspondingly, which values of molar volumes the liquid and gas phases will assume, we need to use the so-called Maxwell area construction rule [22].

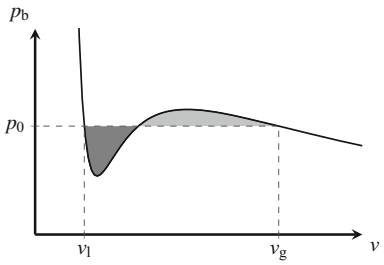

Fig. 9.2 Maxwell area construction rule for the van-der-Waals equation of state for a fixed temperature T. Note that the phase transition occurs at a pressure p_0 that equalises the areas below (*dark grey*) and above (*light grey*) the pressure curve

The **Maxwell area construction rule** postulates that, for a given temperature T, the liquid-gas coexistence happens at a pressure p_0 such that both shaded areas in Fig. 9.2 are identical:

$$\int_{\upsilon_g}^{\upsilon_l} \left(p_0 - p_b(\upsilon', T)\right) \mathrm{d}\upsilon' = 0. \tag{9.3}$$

The molar volumes of the gas and the liquid both satisfy

$$p_0 = p_b(\upsilon_g, T) = p_b(\upsilon_l, T). \tag{9.4}$$

In essence, the Maxwell area construction rule states that, at coexistence, the Gibbs free energy G, or equivalently the chemical potential μ, of the liquid and gas phases must be equal.[3] To see this, we note that the difference in the Helmholtz free energy F in both fluid phases is given by [22]

$$F_l - F_g = -\int_{\upsilon_g}^{\upsilon_l} p_b(\upsilon', T)\, \mathrm{d}\upsilon' \tag{9.5}$$

and that the Gibbs free energy is [22]

$$G_{l/g} = F_{l/g} + p_0 \upsilon_{l/g}. \tag{9.6}$$

[3] For readers unfamiliar with Gibbs and Helmholtz free energies, their descriptions can be found in most textbooks on thermodynamics, e.g. [22]. Briefly, Gibbs free energy is usually used when the system is under constant pressure and temperature, while the Helmholtz free energy is taken when the system is under constant volume and temperature.

Equation (9.3) essentially states that the Gibbs free energy of the system obeys $G = G_\mathrm{l} = G_\mathrm{g}$ (see Exercise 9.1). The chemical potential is the molar Gibbs free energy at constant pressure and temperature, $G = \mu n$, where n is the number of moles. Therefore, an equivalent statement is that the chemical potential in the liquid and gas phases are equal: $\mu_\mathrm{l} = \mu_\mathrm{g}$. If the chemical potentials of the liquid and gas phases are not the same, either the liquid will evaporate or the gas will condense.

Exercise 9.1 Starting from the definitions in (9.5) and (9.6), show that (9.3) leads to the condition that $G_\mathrm{l} = G_\mathrm{g}$.

The molar volume υ is not a convenient parameter to use in LB simulations. Since it is proportional to the inverse of density, $\upsilon \propto 1/\rho$, the Maxwell area construction rule can easily be rewritten in terms of the density:

$$\int_{\rho_\mathrm{g}}^{\rho_\mathrm{l}} \left(p_0 - p_\mathrm{b}(\rho', T)\right) \frac{\mathrm{d}\rho'}{\rho'^2} = 0, \quad p_0 = p_\mathrm{b}(\rho_\mathrm{g}, T) = p_\mathrm{b}(\rho_\mathrm{l}, T). \tag{9.7}$$

Equation (9.7) provides three equations for the three unknowns p_0, ρ_g and ρ_l. Given the form of the equation of state $p_\mathrm{b}(\rho, T)$ at a fixed temperature T, this system of equations can be uniquely solved.

Any model for the equation of state that satisfies (9.7) is *thermodynamically consistent*. Ideally all models should follow this requirement, which is the case for free-energy multiphase and multicomponent models (cf. Sect. 9.2). However, this is not necessarily true for the Shan-Chen model. In practice, this means that the recovered liquid and vapour densities do not exactly assume their expected values. We will elaborate on this issue in Sect. 9.3.

All these considerations are valid for the bulk, far away from any interface. Now we have to look closer at the effect interfaces have on the thermodynamic behaviour.

9.1.2 Surface Tension and Contact Angle

The richness of the multiphase and multicomponent flow behaviour comes, among others, from the interfaces formed between the bulk fluid phases. The presence of surface tension gives rise to complex viscoelastic behaviour, even though each phase/component in the flow itself may be a simple Newtonian fluid [23, 24].

A key concept for multiphase and multicomponent flows is the *surface tension* γ. It is the energy per unit area required to form the interface between the two fluid phases or components.[4] Therefore, surface tension is often given in Joule per square metre or, more commonly, Newton per metre.

[4]This definition is strictly valid only for simple liquids. More generally, the energy per unit area for stretching the interface is given by $\Gamma = \gamma + \mathrm{d}\gamma/\mathrm{d}\epsilon$ where ϵ is the strain. For simple liquids we have $\mathrm{d}\gamma/\mathrm{d}\epsilon = 0$ and $\Gamma = \gamma$.

Surface tension is caused by molecular interactions. Like molecules in a fluid typically attract each other. As illustrated in Fig. 9.1b, if such a molecule is in the bulk region, it will interact on average with z molecules of the same species, where z is the coordination number or the average number of neighbours. If this molecule is at an interface, it will lose interactions with approximately $z/2$ neighbours of like molecules. Furthermore, for multicomponent systems, the molecule will pick up less favourable interactions with molecules of a different species at the interface. This excess energy associated with an interface is usually positive, and it is a function of temperature. Thermodynamically, any physical system will prefer to minimise the amount of surface energy and therefore the total interface area.

If the volume bounded by the interface is not constrained, for example in the case of soap films, the shape of the interface will adopt one of the so-called *minimal surfaces*. Examples of well-known minimal surfaces include the plane (which is the trivial case), the catenoids, and the Schwarz triply periodic minimal surfaces [25]. For minimal surfaces, the surface is locally flat and there is no pressure jump across the interface. More precisely, the mean curvature of the surface is zero, although the Gaussian curvature may assume a non-zero value.[5]

For many multiphase and multicomponent flows, however, we find closed interfaces that enclose a certain volume, e.g. oil droplets in a pot of water or rain drops in air. In general, at mechanical equilibrium, the pressures on either side of these interfaces are different; the pressure at the inside is higher than the pressure outside. The pressure difference satisfies the so-called Laplace pressure [26].

Consider a droplet of one fluid (e.g. a liquid) suspended in another fluid (e.g. a gas). The **Laplace pressure** is

$$p_{\mathrm{l}} - p_{\mathrm{g}} = \gamma_{\mathrm{lg}} \left(\frac{1}{R_1} + \frac{1}{R_2} \right) \tag{9.8}$$

where R_1 and R_2 are the local curvature radii and γ_{lg} is the liquid-gas surface tension. This is illustrated in Fig. 9.3a.

Equation (9.8) has two important physical interpretations. First, it is a consequence of the force balance between the work done by the pressures on either side of the interface, and the energy penalty from changing the interfacial area. Secondly, it states that in equilibrium the mean curvature of the interface between the two fluid phases is constant. If this condition is not satisfied, it results in a force in the

[5] At a given point on a surface, we can define two radii of curvature, as shown in Fig. 9.3a. The mean curvature is simply defined as the average $(1/R_1 + 1/R_2)/2$, while the Gaussian curvature is the product $1/(R_1 R_2)$. Since one of the curvature radii can be negative and the other positive (e.g. a saddle surface), the mean curvature can vanish, even for a non-planar surface.

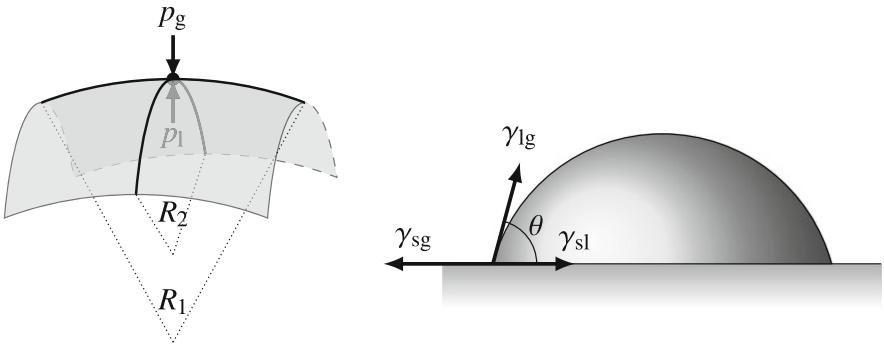

(a) $p_l - p_g = \gamma_{lg}\,(1/R_1 + 1/R_2)$ (b) $\gamma_{lg}\cos\theta = \gamma_{sg} - \gamma_{sl}$

Fig. 9.3 Schematic diagrams for (**a**) the Laplace pressure and (**b**) Young's contact angle. Each point at the interface can be characterised by two independent radii of curvature that can be positive or negative. In (**a**), the surface is convex and both radii are positive. The average curvature $(1/R_1 + 1/R_2)/2$ and the surface tension γ_{lg} are related to the pressure jump (Laplace pressure) $p_l - p_g$ across the interface. In (**b**), a liquid droplet is in contact with a surface and forms a contact angle θ. For this angle, all surface tension force components tangential to the surface are in mechanical equilibrium

hydrodynamic equations of motion, driving the system towards equilibrium. We will see later how this is accounted in the Navier-Stokes equation.

In many (if not most) situations, multicomponent and multiphase flows are also confined by solid surfaces, e.g. in porous media and microfluidics. The different fluid phases may have different affinities to these surfaces. This is usually quantified by a material property called the contact angle θ as shown in Fig. 9.3b.

For a droplet of one fluid (e.g. a liquid) surrounded by another fluid (e.g. a gas), we write

$$\cos\theta = \frac{\gamma_{sg} - \gamma_{sl}}{\gamma_{lg}} \tag{9.9}$$

for the **contact angle**. Here, γ_{sl}, γ_{sg} and γ_{lg} are, respectively, the solid-liquid, solid-gas and liquid-gas surface tensions. The contact angle is usually defined with respect to the liquid phase. We can understand the contact angle as a consequence of mechanical stability at the contact line where all three phases are in contact with each other [27, 28].

When $\theta < 90°$ in (9.9), the liquid phase preferably wets the solid surface. Such a surface is usually called a *hydrophilic*, or more generally a *lyophilic* surface. In contrast, a surface is called *hydrophobic* or *lyophobic* when $\theta > 90°$, i.e. when the gas phase has a favourable interaction with the solid. In the wetting literature,

special terms are also reserved for $\theta = 0°$ (complete wetting), $\theta = 90°$ (neutral wetting) and $\theta > 160°$ (*superhydrophobic*).

The wetting properties can significantly affect the fluid flow near a solid boundary [29, 30]. Furthermore, it has been demonstrated that we can take advantage of surface patterning, both chemical and topographical, to control the motion of fluids [31, 32].

9.1.3 Sharp and Diffuse Interface Models

There are two different approaches to model multiphase and multicomponent flows: (i) sharp and (ii) diffuse interface models.

In the *sharp interface model*, the interface is a 2D boundary which is usually represented by a distinct computational mesh. The motion of this interface needs to be explicitly tracked, and we require a Navier-Stokes solver on either side of the boundary. Furthermore, the fluid velocity at the boundary must be continuous, and there is a stress jump normal to the interface corresponding to the Laplace pressure in (9.8). There are various publications describing in detail how such a sharp interface model can be efficiently implemented, which include volume-of-fluid [33], front-tracking [34], and immersed boundary [35] methods.

Contrarily, the models employed in the LB community usually belong to the *diffusive interface approach*. A typical 1D order parameter profile (density for multiphase flow; ϕ as defined in (9.2) for multicomponent flow) across a diffuse interface is shown in Fig. 9.4. Far from the interface, for $x \to \pm\infty$, the order parameter approaches the bulk values. The order parameter profile smoothly varies across the interface between the two bulk values.

The length scale that characterises the variation in the density profile across the interface is called the *interface width*. For a real physical system, this is usually of the order of nanometres. In the computational domain, the interface width is chosen to be several lattice spacings for the simulations to be stable. However, this does not necessarily mean that the grid spacing in multiphase and multicomponent simulations is assigned to several nanometres; this would limit the applicability of those simulations to nanoscale systems. Instead, we take advantage of the separation

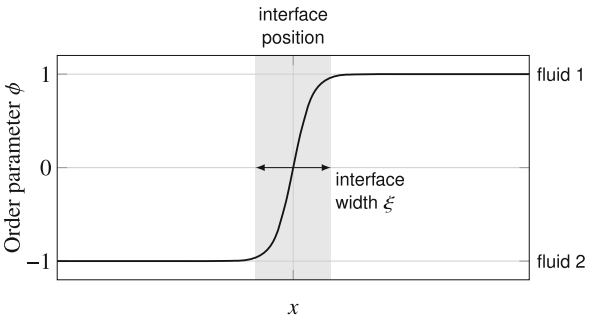

Fig. 9.4 A typical interface profile in the diffuse interface model. The order parameter varies smoothly across the interface to assume its bulk value on either side of the interface. For a multiphase system, the density varies from the gas density ρ_g to the liquid density ρ_l across the interface

of length scales. Ideally we work in a regime where the simulation results do not depend on the interface width. This can be achieved when the interface width is small enough, typically by an order of magnitude smaller than the first important length scale (e.g. the diameter of a droplet). It is often not necessary to truthfully represent the ratio between the physical length scale and the interface width, which makes diffuse-interface multiphase simulations possible in the first place.

The **key advantage of diffuse interface models** is that the motion of the interface need not be tracked explicitly. All fluid nodes can be treated on an equal footing, whether they are in the bulk of the fluid or at the interface. There is no need to introduce any additional mesh for the interface. Thus, diffuse interface models are convenient for studying problems with complex surface geometries.

The density (or order parameter) variation in diffuse interface models is smooth. This allows us to incorporate the description of surface tension into the bulk fluid equations of motion, more specifically in the description of the *pressure tensor* $\boldsymbol{P}$ that also varies smoothly across the interface.

In the definition of pressure as a tensor, $P_{\alpha\beta}$ corresponds to force per unit area in the β-direction on a surface pointing in the α-direction. For a homogeneous and isotropic fluid, which is the case we encountered up to this point, the pressure is the same in all directions. This isotropy means the pressure tensor is given by $P_{\alpha\beta} = p_{\mathrm{b}}\delta_{\alpha\beta}$, and we can treat pressure as a scalar.

When an interface is involved, isotropy is clearly broken: the directions normal and tangential to the interface do not behave in the same way. The fluid equations of motion for diffuse interfaces are given by none other than the continuity and Navier-Stokes equations with a modified pressure tensor[6]:

$$\partial_t \rho + \partial_\alpha(\rho u_\alpha) = 0, \tag{9.10}$$

$$\partial_t(\rho u_\alpha u_\beta) = -\partial_\beta P_{\alpha\beta} + \partial_\beta \eta(\partial_\beta u_\alpha + \partial_\alpha u_\beta). \tag{9.11}$$

It is important to note that the divergence of the pressure tensor, $-\partial_\beta P_{\alpha\beta}$, is equivalent to a body force density F_α. Therefore, the multiphase and multicomponent behaviour can be included in the governing equations in different ways as we will discuss in Sect. 9.2.

We have not yet specified how the pressure tensor looks like, in particular, how it depends on the density (or order parameter). Indeed, this is where the different LB

[6]For multicomponent flows, an additional equation of motion is needed to describe the evolution of the order parameter. This is usually given by the Cahn-Hilliard or Allen-Cahn equation, see e.g. Sect. 9.2.2.3.

models distinguish themselves. Broadly speaking, these models can be categorised into a bottom-up or a top-down approach.

In a **bottom-up approach**, the starting point is often kinetic theory, and some form of interactions are postulated between the fluids at the level of the Boltzmann equation. Similar to many other lattice- and particle-based simulation techniques, separation between different fluid phases and components can be induced by tuning the interaction potentials. The Shan-Chen method (cf. Sect. 9.3) is one famous example. In particular, the Shan-Chen model makes use of an additional body force density rather than a modified pressure tensor.

In a **top-down approach**, we start by writing down the free energy of the fluids (cf. Sect. 9.2). The form of the free energy functional should capture intended features of the thermodynamics of the system, e.g. phase separation and surface tension between different fluids. The corresponding chemical potential and pressure tensor can then subsequently be derived.

9.1.4 Surface Tension and Young-Laplace Test

While the detailed form of the pressure tensor is model specific, irrespective of the model, the pressure tensor must describe an equation of state that allows for phase coexistence between several fluid phases/components, and it must account for the surface tension. In Sect. 9.1.1 we discussed the van der Waals equation of state, one of the most popular equations of state for a multiphase flow. Other equations of states are possible and will be discussed later in this chapter.

The surface tension, in diffuse interface models, is typically introduced *via* a surface tension force given by [36, 37]

$$\boldsymbol{F} = \kappa\rho\nabla\Delta\rho. \tag{9.12}$$

For a multicomponent flow, the same form applies except we replace the density ρ by the order parameter ϕ.

At this point, it is also useful to recognise that the relevant term in the Navier-Stokes equation is the divergence of the pressure tensor, not the pressure tensor itself. In this context, we can immediately show that

$$\begin{aligned}
\partial_\alpha p_\mathrm{b} - F_\alpha &= \partial_\alpha p_\mathrm{b} - \kappa\rho\partial_\alpha\partial_\gamma\partial_\gamma\rho = \partial_\alpha p_\mathrm{b} - \kappa\partial_\alpha(\rho\partial_\gamma\partial_\gamma\rho) + \kappa(\partial_\alpha\rho)\partial_\gamma\partial_\gamma\rho \\
&= \partial_\alpha p_\mathrm{b} - \kappa\partial_\alpha(\rho\partial_\gamma\partial_\gamma\rho) + \kappa\partial_\gamma\left((\partial_\alpha\rho)(\partial_\gamma\rho)\right) - \kappa(\partial_\gamma\rho)\partial_\alpha\partial_\gamma\rho \\
&= \partial_\alpha p_\mathrm{b} - \kappa\partial_\alpha(\rho\partial_\gamma\partial_\gamma\rho) + \kappa\partial_\gamma\left((\partial_\alpha\rho)(\partial_\gamma\rho)\right) - \frac{\kappa}{2}\partial_\alpha\left((\partial_\gamma\rho)^2\right)
\end{aligned}$$

$$= \partial_\beta \left[\left(p_\mathrm{b} - \frac{\kappa}{2}(\partial_\gamma \rho)^2 - \kappa \rho \partial_\gamma \partial_\gamma \rho \right) \delta_{\alpha\beta} + \kappa (\partial_\alpha \rho)(\partial_\beta \rho) \right]$$
$$= \partial_\beta P_{\alpha\beta}. \tag{9.13}$$

The term in the square bracket defines the pressure tensor $P_{\alpha\beta}$: it contains information about the equation of state and the fluid-fluid surface tension. We also note that it is the $\kappa(\partial_\alpha \rho)(\partial_\beta \rho)$ term that causes the pressure tensor to be anisotropic.

Given the pressure tensor $\boldsymbol{P}$, the surface tension can be computed. It is defined as the mismatch between the normal and transversal components of the pressure tensor, integrated across the interface in its normal direction [28, 38]:

$$\gamma = \int_{-\infty}^{\infty} (P_\mathrm{n} - P_\mathrm{t}) \, \mathrm{d}\hat{n} \tag{9.14}$$

where $\hat{\boldsymbol{n}}$ is a unit vector normal to the interface.

To clarify the notation, let us take an example where the interface is located at $x = 0$ and spans across the y-z plane. In such a case, $\hat{\boldsymbol{n}}$ is in the x-direction, $P_\mathrm{n} = P_{xx}$ and $P_\mathrm{t} = P_{yy} = P_{zz}$. Using the definition of the pressure tensor in (9.13), we can show that

$$P_\mathrm{n} = P_{xx} = \left(p_\mathrm{b} - \frac{\kappa}{2}(\partial_\gamma \rho)^2 - \kappa \rho \partial_\gamma \partial_\gamma \rho \right) + \kappa (\partial_x \rho)(\partial_x \rho), \tag{9.15}$$

$$P_\mathrm{t} = P_{yy} = P_{zz} = \left(p_\mathrm{b} - \frac{\kappa}{2}(\partial_\gamma \rho)^2 - \kappa \rho \partial_\gamma \partial_\gamma \rho \right), \tag{9.16}$$

$$\gamma = \int_{-\infty}^{\infty} (P_\mathrm{n} - P_\mathrm{t}) \, \mathrm{d}x = \kappa \int_{-\infty}^{\infty} \left(\frac{\mathrm{d}\rho}{\mathrm{d}x} \right)^2 \mathrm{d}x. \tag{9.17}$$

Note that we can also compute the interface profile $\rho(x)$ or $\phi(x)$, given the functional form of the pressure tensor. This is demonstrated in Appendix A.7 and Appendix A.8.

The surface tension as defined in (9.14) is not always straightforward to compute in simulations. There is, however, a simpler way to measure γ by exploiting the Laplace pressure relation in (9.8). In practice, this is usually achieved by simulating a spherical domain of fluid 1 with radius R, surrounded by fluid 2. Depending on the system of interest, this can be (i) a liquid droplet in a gas phase, (ii) a gas bubble in a liquid phase or (iii) a liquid droplet in another liquid phase. This procedure is called the *Young-Laplace test* or just *Laplace test*.

We have to distinguish between a spherical droplet/bubble in 3D and a circular droplet/bubble in 2D. While in 3D we have two principal curvature radii, there is only a single radius in 2D. Therefore, the pressure difference between the inside

(phase/component 1) and the outside (phase/component 2) assumes the form

$$p^{(1)} - p^{(2)} = \begin{cases} \gamma/R & \text{(2D)}, \\ 2\gamma/R & \text{(3D)}. \end{cases} \tag{9.18}$$

By computing the pressure values at the centre of the droplet/bubble, i.e. $p^{(1)}$, and far away from the interface in the exterior phase/component, i.e. $p^{(2)}$, we can then obtain the surface tension γ.

For this test to be successful we have to be aware of several issues. First, it is crucial to use a sufficiently large droplet/bubble. If it is too small, the interior will be dominated by the shape of the diffuse interface and the measured pressure $p^{(1)}$ will not represent the correct value of the bulk pressure in the interior phase. A reasonable radius to start with is $R \sim 10\Delta x$, assuming the interface width is 2–4 grid nodes. Secondly, it is not obvious how to define the radius of a droplet/bubble with a diffuse interface. Many researchers define the interface as the surface where either the order parameter becomes zero or the density reaches the average of the bulk gas and liquid densities. It is good practice to run several simulations with different droplet radii to show that the measured curve $p^{(1)} - p^{(2)}$ *vs.* $1/R$ is linear, with the gradient of the curve being the surface tension γ in 2D and 2γ in 3D.

9.2 Free-Energy Lattice Boltzmann Model

In this section we will focus on the free-energy lattice Boltzmann models, covering both multiphase and multicomponent systems [39, 40]. The free-energy approach has a *top-down* philosophy: we start with a free-energy functional that contains the thermodynamics of the intended systems, and then other relevant physical quantities can be derived from this functional. Thus, an attractive feature of free-energy LB models is that, by design, they are always thermodynamically consistent.[7] This is in contrast to the Shan-Chen method covered in Sect. 9.3, where we begin by postulating interactions between the lattice fluids, and the thermodynamics of the multiphase and multicomponent systems emerge from these interactions.

So, what information is contained in the free energy functional? It prescribes the free energy that a given system has in a particular arrangement. For particle-based models, the energy depends on the position and orientation of the particles. For continuum models, such as the ones we have here, the situation is similar, except that the energy now depends on collective, coarse-grained variables. For example, density is a suitable collective variable for multiphase flows; the relative concentration (order parameter) is appropriate for multicomponent flows. In thermodynamic equilibrium,

[7] Thermodynamic consistency is defined in Sect. 9.1.1. See also Appendix A.7 where this is shown explicitly for the Landau multiphase model.

the free energy functional is minimised. If the system is out of equilibrium, e.g. due to external influence, the free energy is not minimised and there is a *thermodynamic force* driving the system towards equilibrium. In the context of the Navier-Stokes equation, such thermodynamic force can be equivalently represented as a body force or as gradient in the fluid pressure tensor.

For multiphase and multicomponent flows, the free energy functional usually consists of three terms:

$$\Psi = \int_V \left[\psi_\mathrm{b} + \psi_\mathrm{g}\right] \mathrm{d}V + \int_A \psi_\mathrm{s} \, \mathrm{d}A \tag{9.19}$$

where ψ_b, ψ_g and ψ_s are functions of space and time. The first term, ψ_b, describes the bulk free energy. This term, most importantly, must lead to an equation of state that allows for the coexistence of several fluid phases and/or components. The equation of state for an isothermal ideal gas, $p_\mathrm{b} = c_\mathrm{s}^2 \rho$, does not have this capacity. A wide range of models have been proposed in the literature for the bulk free energy. The simplest models correspond to Landau free-energy models [41–43], which are essentially Taylor expansions in terms of the order parameters. These models are very popular due to their simplicity. However, more complex and realistic bulk free energies, such as the van der Waals [39, 40, 44] or Peng-Robinson models [45], may also be used.

The second term, ψ_g, is a gradient term which penalises any variation in the order parameter, be it the fluid density for multiphase flows or the relative concentration for multicomponent flows. This term captures the free energy of the interface between two fluid phases or components. Its form can be adjusted to handle surface tension and/or bending energy of the interface.

The last term, ψ_s, describes the interaction between the fluid and the surrounding solid. This term is required when the physics of wetting phenomena are relevant.

In the following, we will demonstrate how the equation of state, the pressure tensor and the chemical potential can be written down. We will show how suitable LB schemes can be devised to solve the hydrodynamic equations of motion for multiphase (cf. Sect. 9.2.1) and multicomponent flows (cf. Sect. 9.2.2).

9.2.1 Liquid-Gas Model

Here we will focus on the multiphase free-energy LBM. Following the *top-down* philosophy, we will start by describing the bulk thermodynamics of the multiphase fluid, followed by how the thermodynamics enter the fluid equations of motion, and subsequently the LB algorithm. For many applications of multiphase LBM, the wettability of the surface confining the fluid is also important. We will discuss how suitable surface thermodynamics can be introduced, and show that it enters our LB algorithm as a boundary condition.

9.2.1.1 Bulk Thermodynamics

We start by investigating the bulk properties far away from any solid boundaries, i.e. ψ_s does not play a role. The simplest multiphase model is a two-phase system where a liquid is in coexistence with its own vapour.

For pedagogical reasons, we will use a **model based on Landau theory** [41] so that we can derive all relevant quantities analytically:

$$\Psi = \int_V \left[\psi_b + \psi_g\right] \mathrm{d}V, \tag{9.20}$$

$$\psi_b = p_c \left(\nu_\rho^2 - \beta\tau_w\right)^2 + \mu_0\rho - p_0, \tag{9.21}$$

$$\psi_g = \frac{\kappa}{2}(\nabla\rho)^2 \tag{9.22}$$

where we have defined the reduced density $\nu_\rho = (\rho - \rho_c)/\rho_c$ and the reduced temperature $\tau_w = (T_c - T)/T_c$. The subscript c indicates the critical point of the liquid-gas system, such that p_c, ρ_c and T_c describe the pressure, density and temperature at the critical point. β is a constant which can be tuned to control the liquid-gas density ratio, and κ is a constant which controls the magnitude of the surface tension. The constants μ_0 and p_0 are the reference chemical potential and pressure of the fluids. We will describe the relevance of these parameters in more detail below.

Other bulk free energy functionals, leading to more realistic equations of state, can be used instead for ψ_b. The machineries for deriving the pressure tensor, surface tension and LB schemes are the same as the ones we will show below for the Landau model. The form for the gradient free energy functional, ψ_g, is the one most commonly used to capture surface tension, but once again, it is not unique. Additional terms can be introduced, e.g. to account for the bending energy of the interface [46]. In standard LB methods, we also have total mass conservation such that (9.20) is subject to the constraint $\int_V \rho\,\mathrm{d}V = \text{const}$.

The Landau free energy functional is written such that, below the critical temperature T_c (for positive τ_w), the system will favour two bulk solutions corresponding to $\nu_\rho^2 - \beta\tau_w = 0$. The positive branch $\nu_l = (\rho - \rho_c)/\rho_c = +\sqrt{\beta\tau_w}$ is the liquid state, while the negative branch $\nu_g = (\rho - \rho_c)/\rho_c = -\sqrt{\beta\tau_w}$ is the gas state. Above the critical temperature, the system cannot exhibit liquid-gas coexistence. Mathematically speaking, the solution for ν_ρ becomes imaginary above T_c in this model. ρ_c and p_c are the density and pressure at the critical point of the material, where the liquid and gas phases are indistinguishable. In this model, the liquid and gas densities can be varied by tuning the value of $\beta\tau_w$, as shown in Fig. 9.5.

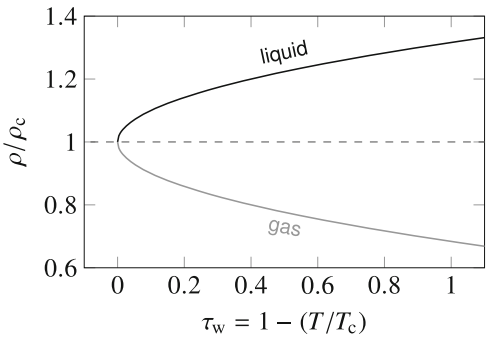

Fig. 9.5 The bulk liquid and gas densities for the Landau model given in (9.21) as a function of the reduced temperature τ_w. We have used $\beta = 0.1$ for this plot. Above the critical temperature T_c (i.e. for $\tau_w < 0$) the liquid and gas phases are indistinguishable

The gradient term in (9.22) penalises changes in the density. This is key to the formulation of surface tension in this model. To appreciate this statement, let us first derive the *chemical potential*.

The chemical potential is defined as the free energy cost (gain) for adding (removing) materials to (from) the system. Mathematically, this is given by

$$\mu \equiv \frac{\delta(\psi_b + \psi_g)}{\delta\rho} = \frac{4p_c}{\rho_c}\nu_\rho\left(\nu_\rho^2 - \beta\tau_w\right) + \mu_0 - \kappa\Delta\rho. \tag{9.23}$$

In thermodynamic equilibrium, the chemical potential is constant everywhere in space. If it is not constant, there will be a free energy gain by transferring fluid material from one part of the system to another. In other words, there will be a *thermodynamic force*.

When the system is in one of the bulk free energy minimum solutions, either in the liquid or in the gas phase, then $\nu_\rho^2 - \beta\tau_w = 0$ and the gradient term in (9.23) also vanishes. Therefore, we find $\mu = \mu_0$ in the liquid and gas bulk phases. Now, our statement that the chemical potential is constant everywhere in space includes the liquid-gas interface where the density varies. For simplicity, let us assume the interface is flat and is located at $x = 0$. The differential equation in (9.23), after setting $\mu = \mu_0$, thus reads

$$\frac{4p_c}{\rho_c}\nu_\rho\left(\nu_\rho^2 - \beta\tau_w\right) - \kappa\rho_c\Delta\nu_\rho = 0 \tag{9.24}$$

with boundary conditions $\nu_\rho = \pm\sqrt{\beta\tau_w}$ (corresponding to the liquid and gas bulk densities) for $x = \pm\infty$.

Equation (9.24) has the following solution for the **liquid-gas interface profile**:

$$\nu_\rho = \sqrt{\beta\tau_w}\tanh\left(\frac{x}{\sqrt{2}\xi}\right) \tag{9.25}$$

(continued)

where $\xi = \sqrt{\kappa\rho_c^2/(4\beta\tau_w p_c)}$ is defined as the interface width, as shown in Fig. 9.4. While ξ can take any value in the analytical model, to have a good numerical resolution in LBM, ξ is usually chosen to be a few lattice spacings.

Furthermore, the **surface tension of the liquid-gas interface** can then be calculated by integrating the free energy density across the interface:

$$\gamma_{lg} = \int_{-\infty}^{\infty} \left[p_c \left(v_\rho^2 - \beta\tau_w \right)^2 + \frac{\kappa}{2}(\nabla\rho)^2 \right] \mathrm{d}x = \frac{4}{3}\sqrt{2\kappa p_c}(\beta\tau_w)^{3/2}\rho_c. \tag{9.26}$$

We can ignore the terms $\mu_0\rho$ and p_0 from the above integral because they only contribute to a constant in the free energy. An alternative derivation for the liquid-gas interfacial profile is also given in Appendix A.7 for the free-energy model.

9.2.1.2 Equations of Motion

In a multiphase model, the continuum equations of motion for the fluid are described by the continuity and Navier-Stokes equations (in the absence of external forces):

$$\partial_t\rho + \partial_\beta\left(\rho u_\beta\right) = 0, \tag{9.27}$$

$$\partial_t(\rho u_\alpha) + \partial_\beta\left(\rho u_\alpha u_\beta\right) = -\partial_\beta P_{\alpha\beta} + \partial_\beta\eta\left(\partial_\beta u_\alpha + \partial_\alpha u_\beta\right). \tag{9.28}$$

The thermodynamics of the multiphase system, including the description of the surface tension, enter the equations of motion through the pressure tensor $P_{\alpha\beta}$.

The **pressure tensor** $P_{\alpha\beta}$ can be derived (up to a constant contribution in space throughout the simulation domain) by requiring [47]

$$\partial_\beta P_{\alpha\beta} = \rho\partial_\alpha\mu. \tag{9.29}$$

This equation states that the presence of a thermodynamic force leads to a pressure tensor gradient for the fluids. This statement is general, not only for Landau models. For our specific Landau model, using the definition of the chemical potential μ in (9.23), it follows that

$$P_{\alpha\beta} = \left(p_b - \frac{\kappa}{2}(\partial_\gamma\rho)^2 - \kappa\rho\partial_\gamma\partial_\gamma\rho \right)\delta_{\alpha\beta} + \kappa(\partial_\alpha\rho)(\partial_\beta\rho), \tag{9.30}$$

$$p_b = p_c(v_\rho + 1)^2\left(3v_\rho^2 - 2v_\rho + 1 - 2\beta\tau_w\right). \tag{9.31}$$

(continued)

Equation (9.31) is the **equation of state** for this model. It relates the bulk pressure of the fluid to other thermodynamic quantities such as density and temperature.

Exercise 9.2 Starting from the equation of state in (9.31), show that the pressures at the bulk liquid and gas densities, $\nu_\rho = (\rho - \rho_c)/\rho_c = \pm\sqrt{\beta\tau_w}$, for the free-energy model in (9.20) are equal and satisfy

$$p_0 = p_c(1 - \beta\tau_w)^2. \tag{9.32}$$

Exercise 9.3 In (9.14) we defined the surface tension as the integral of the mismatch between the normal and transversal components of the pressure tensor. By evaluating the integral using (9.30), show that we can recover the same expression for the liquid-gas surface tension as in (9.26).

Exercise 9.4 An alternative approach to derive the pressure tensor is by exploiting equation (9.13) and the standard relation for the equation of state [40, 41]

$$p_b = \rho\partial_\rho\psi_b - \psi_b. \tag{9.33}$$

Verify that the pressure tensor derived using this approach is the same as in (9.30). Furthermore, by substituting the expressions for the pressure tensor and the chemical potential, show that (9.29) is satisfied.

9.2.1.3 The Lattice Boltzmann Algorithm

The thermodynamics of the multiphase flow is encoded in the modified pressure tensor. Therefore, the next step in free-energy LBM is to translate the description of the pressure tensor into the LB equation. This can be done either through a forcing term[8] F_i, a pressure tensor term G_i, or a mix between the two [48]:

$$\begin{aligned} f_i(\boldsymbol{x} + \boldsymbol{c}_i\Delta t, t + \Delta t) = f_i(\boldsymbol{x}, t) - \frac{f_i(\boldsymbol{x}, t) - f_i^{eq}(\boldsymbol{x}, t)}{\tau}\Delta t \\ + \left(1 - \frac{\Delta t}{2\tau}\right) F_i(\boldsymbol{x}, t)\Delta t + G_i(\boldsymbol{x}, t)\Delta t. \end{aligned} \tag{9.34}$$

Here we will limit our discussion to the BGK collision operator. The extension to multiple relaxation times is straightforward.

[8] We note that our convention here follows that of Chap. 6. In the literature, sometimes the prefactor $\left(1 - \frac{1}{2\tau}\right)$ is included in the definition of F_i itself.

The properties of the forcing term F_i have been discussed in detail in Chap. 6. The moments of the pressure tensor term G_i have the following properties:

$$\begin{aligned} \sum_i G_i &= 0, \\ \sum_i G_i c_{i\alpha} &= 0, \\ \sum_i G_i c_{i\alpha} c_{i\beta} &= A_{\alpha\beta}, \\ \sum_i G_i c_{i\alpha} c_{i\beta} c_{i\gamma} &= 0. \end{aligned} \tag{9.35}$$

It is important that only the second moment of the pressure tensor term is non-zero. It does not change the density or momentum of the fluid.

Pressure tensor approach: In the original free-energy LBM, the thermodynamics of the multiphase system is completely accounted for through a pressure tensor term, such that $A_{\alpha\beta} = P_{\alpha\beta} - c_s^2 \rho \delta_{\alpha\beta}$. This term corresponds to how the pressure tensor departs from the ideal gas scenario. The forcing term F_i is then set to zero, unless there is an additional external body force (e.g. gravity), which can be dealt with as in the usual way (cf. Chap. 6).

In the literature, it is further customary to absorb the **pressure tensor term** G_i into the the **equilibrium distribution** f_i^{eq}. Its resulting form for $i \neq 0$ is given by

$$\begin{aligned} f_i^{\mathrm{eq}} = w_i \rho \left(1 + \frac{c_{i\alpha} u_\alpha}{c_s^2} + \frac{u_\alpha u_\beta \left(c_{i\alpha} c_{i\beta} - c_s^2 \delta_{\alpha\beta} \right)}{2 c_s^4} \right) \\ + \frac{w_i}{c_s^2} \left(p_b - c_s^2 \rho - \kappa \rho \Delta \rho \right) + \kappa \sum_{\alpha,\beta} w_i^{\alpha\beta} (\partial_\alpha \rho)(\partial_\beta \rho). \end{aligned} \tag{9.36}$$

The corresponding expression for f_0^{eq} is given in (9.39). The first line in (9.36) is identical to that for standard single-phase and single-component equilibrium distribution functions. The second line accounts for surface tension (the gradient terms) and the deviation of the equation of state p_b from the ideal gas case, which must allow for a coexistence between the liquid and gas phases.

The density gradients can be computed using finite difference schemes. We strongly recommend to choose stencils which are at least second-order accurate. Inexactness in computing these derivatives is one of the main reasons for the appearance of spurious velocities that affect the accuracy of LBM, and in some

cases its stability. Improving the stencil isotropy of the numerical derivatives has been shown to strongly reduce spurious velocities close to the liquid-gas interface [49–51].

The coefficients $w_i^{\alpha\beta}$ in (9.36) are chosen to minimise the spurious velocities at the interface. For example, following the work of Furtado and Pooley [51], for D3Q19 we can use

$$\begin{aligned}
w_{1,2}^{xx} = w_{3,4}^{yy} = w_{5,6}^{zz} &= \tfrac{5}{12}, \\
w_{3\text{–}6}^{xx} = w_{1,2,5,6}^{yy} = w_{1\text{–}4}^{zz} &= -\tfrac{1}{3}, \\
w_{1\text{–}6}^{xy} = w_{1\text{–}6}^{yz} = w_{1\text{–}6}^{zx} &= 0, \\
w_{7\text{–}10,13\text{–}16}^{xx} = w_{7\text{–}8,11\text{–}14,17\text{–}18}^{yy} = w_{9\text{–}12,15\text{–}18}^{zz} &= -\tfrac{1}{24}, \\
w_{11,12,17,18}^{xx} = w_{9,10,15,16}^{yy} = w_{7,8,13,14}^{zz} &= \tfrac{1}{12}, \\
w_{7,8}^{xy} = w_{11,12}^{yz} = w_{9,10}^{zx} &= \tfrac{1}{4}, \\
w_{13,14}^{xy} = w_{17,18}^{yz} = w_{15,16}^{zx} &= -\tfrac{1}{4}, \\
w_{9\text{–}12,15\text{–}18}^{xy} = w_{7\text{–}10,13\text{–}16}^{yz} = w_{7,8,11\text{–}14,17,18}^{zx} &= 0.
\end{aligned} \tag{9.37}$$

Similarly, for D2Q9 we have

$$\begin{aligned}
w_{1,2}^{xx} = w_{3,4}^{yy} &= \tfrac{1}{3}, \\
w_{3,4}^{xx} = w_{1,2}^{yy} &= -\tfrac{1}{6}, \\
w_{5\text{–}8}^{xx} = w_{5\text{–}8}^{yy} &= -\tfrac{1}{24}, \\
w_{1\text{–}4}^{xy} &= 0, \\
w_{5\text{–}8}^{xy} &= \tfrac{1}{4}.
\end{aligned} \tag{9.38}$$

The expression for the equilibrium distribution function for $i = 0$ is quite lengthy, but in practice we can exploit conservation of mass to write

$$f_0^{\text{eq}} = \rho - \sum_{i \neq 0} f_i^{\text{eq}}. \tag{9.39}$$

Force approach: The thermodynamics of the multiphase system can be equivalently taken into account through a forcing term.

The appropriate **force density** due to the thermodynamics of a multiphase system is the divergence of the non-ideal terms in the pressure tensor

(continued)

$F_\alpha = -\partial_\beta (P_{\alpha\beta} - c_s^2 \rho \delta_{\alpha\beta})$. Additional external forces (e.g. gravity) can also be added to the definition of the total force if they are present. We set $G_i = 0$ in (9.34) and the equilibrium distribution functions take identical forms as those for single-phase flow:

$$f_i^{\mathrm{eq}} = w_i \rho \left(1 + \frac{c_{i\alpha} u_\alpha}{c_s^2} + \frac{u_\alpha u_\beta \left(c_{i\alpha} c_{i\beta} - c_s^2 \delta_{\alpha\beta} \right)}{2 c_s^4} \right), \tag{9.40}$$

$$F_i = w_i \left(\frac{\boldsymbol{c}_i - \boldsymbol{u}}{c_s^2} + \frac{(\boldsymbol{c}_i \cdot \boldsymbol{u})\, \boldsymbol{c}_i}{c_s^4} \right) \cdot \boldsymbol{F}, \tag{9.41}$$

$$\rho \boldsymbol{u} = \sum_i f_i \boldsymbol{c}_i + \frac{\boldsymbol{F} \Delta t}{2}. \tag{9.42}$$

Here we have used the method of Guo et al. [52] to implement the body force. More detailed explanations of the forcing term in LBM are discussed in Chap. 6.

At the level of numerical implementation, the forcing approach can be implemented in two different ways. First, in the so-called *pressure form* (not to be confused with the pressure tensor approach), the force density at every time step is computed as

$$F_\alpha = -\partial_\beta P_{\alpha\beta} + \partial_\alpha c_s^2 \rho, \tag{9.43}$$

as we have written above. Secondly, in the *potential form*, the force density is

$$F_\alpha = -\rho \partial_\alpha \mu + \partial_\alpha c_s^2 \rho. \tag{9.44}$$

Analytically the two forms are of course equivalent, cf. (9.29). However, upon discretisation, they are not exactly identical since the derivatives are usually approximated using finite difference schemes [53, 54]. Numerical evidence suggests that schemes which employ the potential form have lower spurious velocities [49, 55]. However, an important caveat is that the potential form is no longer written in a conservative form (i.e. as a divergence). This means momentum conservation is no longer satisfied exactly for the discretised potential form [53]. In his implementation, Wagner [55] also introduced a small amount of numerical viscosity to render the simulations stable.

As we shall see below, the pressure tensor approach as currently stated is inadequate for most applications because it does not satisfy Galilean invariance. The pressure tensor approach generally also produces higher spurious velocities [51, 55]. However, an advantage of using the pressure tensor approach is that we do

not need to compute the third-order derivative in ρ, which is unavoidable in the force approach (potential form). Computing third-order derivatives require information from more neighbours, which affect parallelisation, and are more expensive to compute. In this context, to avoid computing third derivatives, a possible hybrid approach is to rewrite (9.29) as

$$\partial_\beta P_{\alpha\beta} = \rho\partial_\alpha\mu = \partial_\alpha(\mu\rho) - \mu\partial_\alpha\rho. \tag{9.45}$$

The first term can be absorbed in the equilibrium distribution, by defining a modified isotropic pressure $\tilde{p}_\mathrm{b} = \mu\rho$, while the second term is introduced as a forcing term $F_\alpha = -\mu\partial_\alpha\rho$. The suitable equilibrium distribution function for $i > 0$ in the hybrid approach is then

$$f_i^{\mathrm{eq}} = w_i\rho\left(\frac{\mu}{c_\mathrm{s}^2} + \frac{c_{i\alpha}u_\alpha}{c_\mathrm{s}^2} + \frac{u_\alpha u_\beta\left(c_{i\alpha}c_{i\beta} - c_\mathrm{s}^2\delta_{\alpha\beta}\right)}{2c_\mathrm{s}^4}\right). \tag{9.46}$$

9.2.1.4 Galilean Invariance

The original free-energy LB algorithm was shown to break Galilean invariance [48, 56, 57]. This is a serious limitation as real physical phenomena do not depend on the frame of reference. To appreciate this issue, let us consider a Chapman-Enskog analysis of (9.34). The analysis results in the continuity equation and the following momentum conservation equation [48]:

$$\begin{aligned}\partial_t(\rho u_\alpha) + \partial_\beta\left(\rho u_\alpha u_\beta\right) = &-\partial_\beta\left(A_{\alpha\beta} + c_\mathrm{s}^2\rho\delta_{\alpha\beta}\right) + F_\alpha\\ &+\partial_\beta\rho\nu\left(\partial_\beta u_\alpha + \partial_\alpha u_\beta + \partial_\gamma u_\gamma\delta_{\alpha\beta}\right)\\ &-\nu\partial_\beta\left(u_\alpha\partial_\gamma A_{\beta\gamma} + u_\beta\partial_\gamma A_{\alpha\gamma} + \partial_\rho A_{\alpha\gamma}\partial_\gamma(\rho u_\gamma)\right)\\ &+\nu\partial_\beta\partial_\gamma(\rho u_\alpha u_\beta u_\gamma).\end{aligned} \tag{9.47}$$

We remember that $A_{\alpha\beta} = P_{\alpha\beta} - c_\mathrm{s}^2\rho\delta_{\alpha\beta}$ and $F_\alpha = 0$ for the pressure tensor approach, while $A_{\alpha\beta} = 0$ and $F_\alpha = -\partial_\beta(P_{\alpha\beta} - c_\mathrm{s}^2\rho\delta_{\alpha\beta})$ for the forcing approach, as described above. The first two rows on the right-hand side of (9.47) correspond to the desired Navier-Stokes equation. The last term is an error term which is also present for standard LBM, cf. Sect. 4.1. This term is negligible for $\mathrm{Ma}^2 \ll 1$, which is usually the case for multiphase flow.

Thus, the problematic terms are those in the third row. They break Galilean invariance in the free-energy multiphase model. To restore it, we need to add appropriate correction terms. As an example, let us consider the pressure tensor approach where $A_{\alpha\beta} = P_{\alpha\beta} - c_\mathrm{s}^2\rho\delta_{\alpha\beta}$. To restore Galilean invariance, one option is to introduce a body force

$$F_\alpha = \nu\partial_\beta\left(u_\alpha\partial_\gamma A_{\beta\gamma} + u_\beta\partial_\gamma A_{\alpha\gamma} + \partial_\rho A_{\alpha\gamma}\partial_\gamma(\rho u_\gamma)\right) \tag{9.48}$$

which cancels all the leading error terms in (9.47). Another option is to modify $A_{\alpha\beta}$ such that

$$A_{\alpha\beta} = P_{\alpha\beta} - c_s^2 \rho \delta_{\alpha\beta} - \nu \left(\partial_\alpha (\rho u_\beta) + \partial_\beta (\rho u_\alpha) + \partial_\gamma (\rho u_\gamma) \delta_{\alpha\beta} \right). \tag{9.49}$$

This approach cancels most of the error terms, leaving terms which are proportional to the second derivatives of the fluid pressure, which are usually small for systems close to equilibrium and for moderate Reynolds number.

9.2.1.5 A Practical Guide to Simulation Parameters

The Landau free-energy model is originally designed to describe physical multiphase systems close to the critical point beyond which the liquid and gas phases are no longer distinguishable. However, in practice the Landau model has been exploited for liquid-gas systems far from the critical point. This assumption is valid for cases where the details of the equation of state are irrelevant for the problems at hand. For more realistic equations of state, the van der Waals [39, 40, 44] or Peng-Robinson models [45] should be used.

In the Landau model there are effectively four free parameters to tune the thermodynamics of the liquid-gas system: $\beta\tau_w$, κ, p_c and ρ_c. As a starting point, the following **parameters** are often chosen **for the multiphase Landau model**, all in lattice units: $\beta\tau_w = 0.03$, $\kappa = 0.004$, $p_c = 0.125$ and $\rho_c = 3.5$ [41, 58]. These parameters can be modified with considerations as detailed below.

- $\beta\tau_w$ is important for adjusting the liquid-gas density ratio, since $\rho_l/\rho_g = (1 + \sqrt{\beta\tau_w})/(1 - \sqrt{\beta\tau_w})$. Theoretically, $\beta\tau_w$ can be chosen such that the density ratio is ~ 1000, which is the case for most liquid-gas systems. In practice, however, this is not possible with the algorithms described thus far. The highest density ratio is limited to ~ 10. This is due to spurious velocities which act to destabilise the simulations. We will discuss this issue in Sect. 9.4.1 and Sect. 9.4.2, together with approaches that have been developed to reduce these spurious velocities, and hence achieve realistic density ratios.
- Combined with $\beta\tau_w$, we can choose ρ_c to tune the actual values of the liquid and gas densities, since $\rho_{l,g} = \rho_c(1 \pm \sqrt{\beta\tau_w})$.
- Given the choices for $\beta\tau_w$ and ρ_c, we can use κ and p_c to control two physically meaningful variables: the interface width $\xi = \sqrt{\kappa\rho_c^2/(4\beta\tau_w p_c)}$ and the surface tension $\gamma_{lg} = \frac{4}{3}\sqrt{2\kappa p_c}(\beta\tau_w)^{3/2}\rho_c$. In LBM we usually want the interface width ξ to be $\sim 2 - 3$ lattice spacings. Anything smaller will result in the interfacial profile being resolved very poorly. Larger ξ is in principle better, but this makes

the simulation very expensive, since any relevant physical length scale in the simulation should be at least an order of magnitude larger. Similar to the density ratio, the possible values of the surface tension are usually limited by spurious velocities. As a rule of thumb, the generated spurious velocity increases with the chosen surface tension. In the Landau model, the surface tension (in lattice units) is usually taken to be $\gamma_{\mathrm{lg}} \sim O(10^{-2})$ or less.

It is worth noting that one useful advantage of the Landau free-energy model is that we can compute all equilibrium quantities analytically. This allows us to initialise the desired liquid and gas domains with appropriate densities given by $\rho_{\mathrm{l,g}} = \rho_{\mathrm{c}}(1 \pm \sqrt{\beta\tau_{\mathrm{w}}})$. Furthermore, rather than a step density change, it is advisable to implement a smooth interface, following the tanh profile[9] given in (9.25), with an interface width $\xi = \sqrt{\kappa\rho_{\mathrm{c}}^2/(4\beta\tau_{\mathrm{w}}p_{\mathrm{c}})}$.

Exercise 9.5 Perform the Young-Laplace test as presented in Sect. 9.1.4. Prepare a liquid droplet of radius R surrounded by the gas phase in a periodic system. After the system has equilibriated, measure the bulk liquid and gas densities. Compute the corresponding bulk pressures from (9.31). You will notice that bulk liquid and gas densities deviate slightly from $\rho = \rho_c(1 \pm \sqrt{\beta\tau_{\mathrm{w}}})$. This is because the interface is no longer flat, and the deviation is necessary to account for the Laplace pressure. Make sure you compute these values far from the liquid-gas interface. Repeat this calculation for several values of droplet radius R and plot the pressure difference as function of $1/R$. Note the differences between 2D and 3D as pointed out in (9.18). You should reproduce a similar result to Fig. 9.10 as obtained with the Shan-Chen method.

9.2.1.6 Surface Thermodynamics

In multiphase flows we are often interested in cases where the fluids are in contact with solid surfaces. In general, the liquid and gas phases can interact differently with the surface, which results in the liquid phase wetting or dewetting the surface. The degree of affinity for the liquid and gas phases is often described by the contact angle, as defined in (9.9).

Similar to the bulk thermodynamics, we have different options to represent the **surface thermodynamics**. Following Cahn [59], we choose a surface energy term

$$\Psi_{\mathrm{s}} = \int_A \psi_s \,\mathrm{d}A = -\int_A h\rho_{\mathrm{s}} \,\mathrm{d}A \tag{9.50}$$

(continued)

[9] In fact, the tanh profile provides a good initial interfacial profile for most multiphase and multicomponent models.

where ρ_s is the value of the density at the surface and the integral is taken over the solid surface in our simulation domain. The parameter h is an effective interaction potential between the fluid and the solid surface, which we take to be constant. If h is positive, the fluid molecules interact favourably with the surface, and as such the liquid phase will be preferred over the gas phase close to the surface, as it lowers the free energy of the system more than the gas phase. If h is negative, the solid-fluid interaction is unfavourable, and the gas phase is preferably close to the solid surface. We will see later in (9.65) that the parameter h enters the LB equation as a boundary condition for the density gradient.

To derive an explicit relation between the variable h and the contact angle θ, we will use techniques from calculus of variation. First we will obtain the liquid and gas densities at the solid surface, followed by the solid-liquid and solid-gas surface tensions. Then, using Young's formula in (9.9), we can relate the surface tensions to the contact angle.

Let us start by computing the free energy changes upon variation in the fluid density in (9.19). The rationale behind this is that the contact angle is an equilibrium material parameter, and at equilibrium, the free energy functional is minimised. We find that

$$\begin{aligned}
\delta\Psi &= \int_V \left[\frac{4p_c}{\rho_c}\nu_\rho\left(\nu_\rho^2 - \beta\tau_w\right) + \mu_0\right]\delta\rho\,\mathrm{d}V + \int_V \kappa(\nabla\rho)\cdot(\nabla\delta\rho)\,\mathrm{d}V \\
&\quad - \int_A h\delta\rho_s\,\mathrm{d}A \\
&= \int_V \left[\frac{4p_c}{\rho_c}\nu_\rho\left(\nu_\rho^2 - \beta\tau_w\right) + \mu_0 - \kappa\Delta\rho\right]\delta\rho\,\mathrm{d}V + \int_V \kappa\nabla\cdot(\delta\rho\nabla\rho)\,\mathrm{d}V \\
&\quad - \int_A h\delta\rho_s\,\mathrm{d}A \\
&= \int_V \left[\frac{4p_c}{\rho_c}\nu_\rho\left(\nu_\rho^2 - \beta\tau_w\right) + \mu_0 - \kappa\Delta\rho\right]\delta\rho\,\mathrm{d}V \\
&\quad + \int_A \kappa\left[(\nabla\rho\cdot\hat{\boldsymbol{n}}) - h\right]\delta\rho_s\,\mathrm{d}A. \qquad (9.51)
\end{aligned}$$

To derive (9.51), we have used the divergence theorem to convert one of the volume integrals into a surface integral. We have also used the convention that $\hat{\boldsymbol{n}}$ is the unit vector normal to the surface (pointing outward, not inward). Now the integrand for the volume integral is nothing but our definition for the chemical potential in (9.23). The new term in the presence of a solid surface is the surface integral. Setting

$\delta\Psi/\delta\rho_s = 0$, which is valid for an equilibrium solution, we obtain

$$\kappa(\nabla\rho\cdot\hat{\boldsymbol{n}}) = \kappa\nabla_\perp\rho = h. \tag{9.52}$$

This sets the gradient of the density normal to the solid surface.

To compute the liquid and gas densities at the solid surface, we will exploit the so-called *Noether theorem* [60]. In our context, this allows us to compute a quantity which is conserved across the spatial dimension at equilibrium:

$$\frac{\delta(\psi_b+\psi_g)}{\delta(\nabla\rho)}\cdot\nabla\rho - (\psi_b+\psi_g) + \mu_0\rho = \text{const} \tag{9.53}$$

and therefore

$$\frac{\kappa}{2}(\nabla\rho)^2 - p_c\left(\nu_\rho^2-\beta\tau_w\right)^2 = \text{const} = 0. \tag{9.54}$$

For the last equality, we have used the fact that far from the interface (in the bulk), $\nu_\rho = \pm\sqrt{\beta\tau_w}$ and $\nabla\rho = \mathbf{0}$. Substituting (9.52) into (9.54), we find that the values of the density at the surface may take four possible values corresponding to

$$\nu_{\rho,s} = \frac{\rho_s-\rho_c}{\rho_c} = \pm\sqrt{\beta\tau_w \pm h\sqrt{\frac{1}{2\kappa p_c}}}. \tag{9.55}$$

To decide which solutions are physically admissible, let us consider the following argument. If $h > 0$, we argued above that the fluid molecules have favourable interactions with the solid surface. As such, we expect to have a local increase in the fluid density close to the surface. The relevant solutions for the liquid and gas phases are thus

$$\nu_{sl} = \sqrt{\beta\tau_w}\sqrt{1+\frac{h}{\beta\tau_w\sqrt{2\kappa p_c}}} = \sqrt{\beta\tau_w}\sqrt{1+\Omega}, \tag{9.56}$$

$$\nu_{sg} = -\sqrt{\beta\tau_w}\sqrt{1-\frac{h}{\beta\tau_w\sqrt{2\kappa p_c}}} = -\sqrt{\beta\tau_w}\sqrt{1-\Omega} \tag{9.57}$$

where we have defined $\Omega = h/(\beta\tau_w\sqrt{2\kappa p_c})$. It is also straightforward to see that for $h < 0$ the above solutions give us a local decrease in fluid density close to the surface.

The solid-liquid and solid-gas surface tensions can be calculated similarly to the liquid-gas surface tension in (9.26), except that now we also have to take into account the contributions from the surface energy term. For the solid-liquid surface tension, assuming a flat solid interface at $x = 0$, we find

$$\gamma_{sl} = -h\rho_{sl} + \int_0^\infty\left[p_c\left(\nu_\rho^2-\beta\tau_w\right)^2 + \frac{\kappa}{2}(\nabla\rho)^2\right]\mathrm{d}x. \tag{9.58}$$

To evaluate this integral, we take advantage of Noether's theorem given in (9.54) and use a change of variables such that

$$\int_0^\infty \left[p_c \left(v_\rho^2 - \beta\tau_w \right)^2 + \frac{\kappa}{2} \left(\frac{d\rho}{dx} \right)^2 \right] dx = \int_{v_{sl}}^{v_l} \left[\rho_c \sqrt{2\kappa p_c} \left(\beta\tau_w - v_\rho^2 \right) \right] dv_\rho. \tag{9.59}$$

After some algebra, it is then possible to show that

$$\gamma_{sl} = -h\rho_c + \frac{\gamma_{lg}}{2} - \frac{\gamma_{lg}}{2}(1+\Omega)^{3/2} \tag{9.60}$$

with γ_{lg} given in (9.26).

The solid-gas surface tension can be derived in a similar way, and we obtain

$$\gamma_{sg} = -h\rho_c + \frac{\gamma_{lg}}{2} - \frac{\gamma_{lg}}{2}(1-\Omega)^{3/2}. \tag{9.61}$$

The contact angle follows from substituting the values of the surface tensions into Young's law in (9.9) to give

$$\cos\theta = \frac{\gamma_{sg} - \gamma_{sl}}{\gamma_{lg}} = \frac{(1+\Omega)^{3/2} - (1-\Omega)^{3/2}}{2}. \tag{9.62}$$

Equation (9.62) can be inverted to give a relation between the phenomenological parameter Ω and the equilibrium contact angle θ:

$$\Omega(\theta) = 2\,\mathrm{sgn}(\pi/2 - \theta)\sqrt{\cos(\alpha/3)[1 - \cos(\alpha/3)]} \tag{9.63}$$

where $\alpha(\theta) = \arccos(\sin^2\theta)$ and the function $\mathrm{sgn}(x)$ returns the sign of x. Figure 9.6 shows how Ω depends on the contact angle θ in (9.63).

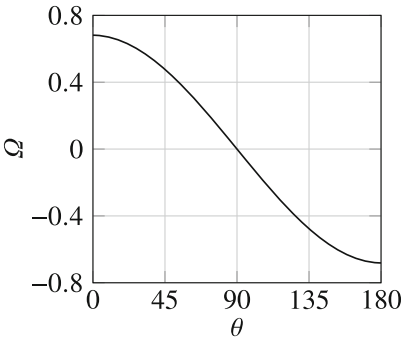

Fig. 9.6 The phenomenological parameter $\Omega = h/(\beta\tau_w\sqrt{2\kappa p_c})$ as a function of the contact angle θ, corresponding to (9.63)

9.2.1.7 Wetting Boundary Condition

At this point, we have elaborated on the surface thermodynamics required to introduce preferential wetting between the liquid and gas phases on the solid surface. When dealing with multiphase flow (similarly multicomponent flow) using free-energy LBM, in addition to standard no-slip boundary condition for the fluid velocity, we also need an additional wetting boundary condition.

To realise the **wetting condition in the LB equation**, we need **two key equations**. First, from (9.63) we have an analytical expression relating the desired contact angle θ to the parameter h which is an input in our model:

$$h = \beta\tau_w\sqrt{2\kappa p_c}\Omega = 2\beta\tau_w\sqrt{2\kappa p_c}\,\mathrm{sgn}(\pi/2-\theta)\sqrt{\cos(\alpha/3)[1-\cos(\alpha/3)]}. \tag{9.64}$$

Secondly, the parameter h enters the LB equation through the wetting boundary condition in (9.52), which sets the gradient of the density normal to the solid surface:

$$\nabla\rho\cdot\hat{\boldsymbol{n}} = \nabla_\perp\rho = \frac{h}{\kappa}. \tag{9.65}$$

The unit normal vector $\hat{\boldsymbol{n}}$ points outward, i.e. into the solid.

We note that the boundary condition in (9.65) specifies the normal gradient of the density at the solid surface. If we use the bounce-back approach to implement the no-slip boundary condition, then the position of the solid wall is usually halfway between two lattice nodes, with a fluid (subscript f below) and a solid (subscript s) node on each side of the wall. A common implementation of the wetting boundary condition is to assign appropriate density values to the solid nodes neighbouring the boundary. For example, we can use a standard finite difference scheme to write

$$\nabla_\perp\rho = \frac{\rho_s-\rho_f}{\Delta x} = \frac{h}{\kappa}, \tag{9.66}$$

and as such,

$$\rho_s = \rho_f + \frac{h}{\kappa}\Delta x. \tag{9.67}$$

An advantage of this approach is that higher order gradients can be calculated in the same way as in the bulk, since neighbouring solid nodes are assigned appropriate density values. For more complex geometries, for example surfaces which do not follow a lattice axis, the wetting boundary conditions can be implemented in a similar way. This typically gives a set of linear equations that must be solved

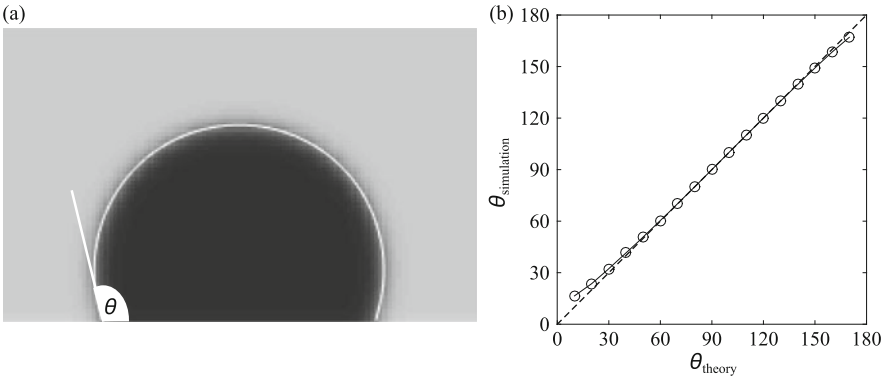

Fig. 9.7 (**a**) A typical simulation result for the contact angle test, as discussed in Exercise 9.6. The white line marks the contour where the local density assumes the value $(\rho_l + \rho_g)/2$. The contact angle is measured locally at the contact line where the liquid-gas interface meets the solid. (**b**) The comparison between the prescribed and the measured contact angles. Excellent agreement is obtained apart from very small and very large contact angles. This discrepancy is due to the finite width of the interface

simultaneously. Furthermore, if a solid node is surrounded by several fluid nodes (e.g. a corner), its density value can be defined in multiple ways via (9.67). In this case, we usually then take the average value.

Exercise 9.6 Implement the wetting boundary condition. Following (9.64), compute the suitable value of h for a given contact angle θ. This effectively sets the value of the density gradient normal to the solid surface, as discussed in (9.65). To set up the simulation, prepare solid nodes at the top and bottom of your simulation box, as shown in Fig. 9.7a. You may use periodic boundary conditions in the other directions. Then place a liquid droplet of radius R (use e.g. $R = 30\Delta x$) surrounded by the gas phase next to one of the solid planes, and let the system equilibrate. After the simulation reaches a steady state, measure the contact angle the droplet forms with the solid surface and compare the result with the prescribed contact angle. This is best done by fitting the interfacial profile of the droplet to the equation for a circle (in 2D) or a sphere (in 3D). The contact angle is the angle formed by the liquid-gas interface and the solid surface. Repeat the simulation for contact angles ranging from 0° to 180°. You should obtain excellent agreement to within 2–3° for $\theta = 20$–160°. Larger deviations are observed for very small and very large contact angles, as shown in Fig. 9.7b.

9.2.2 Binary Fluid Model

We will now move on to a multicomponent system. For simplicity, we will consider a binary fluid where the fluid is a mixture of two distinct fluid components. Similar

to the multiphase model, we will start from the thermodynamics of the model and then discuss how they translate to the LBM. The techniques to implement the multicomponent model are largely the same as for the multiphase model. For this reason, it may be useful for the readers to first read the multiphase free energy section. The main difference is the need to introduce a new equation of motion for the order parameter.

9.2.2.1 Bulk Thermodynamics

As introduced in (9.1), we will use the relative concentration ϕ to distinguish the bulk of one fluid from another. We will use the convention where $\phi = 1$ signifies fluid 1 (e.g. water) and $\phi = -1$ fluid 2 (e.g. oil). The isosurface $\phi = 0$ then corresponds to the interface between the two fluids (e.g. oil-water interface). Given these conventions, we want to construct a free energy functional that has two minima at $\phi = \pm 1$ and provides an energy penalty which scales with the area of the fluid-fluid interfaces. The proportionality constant is the surface tension. We will start with the bulk properties far away from any solid boundary.

The **simplest model for a multicomponent system** which captures the physics mentioned above is given by the following **Landau free energy** [42, 61]:

$$\Psi = \int_V \left[\psi_\mathrm{b} + \psi_\mathrm{g}\right] \mathrm{d}V = \int_V \left[c_\mathrm{s}^2 \rho \ln \rho + \frac{A}{4}\left(\phi^2 - 1\right)^2 + \frac{\kappa}{2}(\nabla\phi)^2\right] \mathrm{d}V. \tag{9.68}$$

The first term in the bracket is the ideal gas free energy, and we will assume here that the density of the two fluids are the same. Otherwise we would need terms that couple the density ρ and the order parameter ϕ. For the multicomponent Landau model, the second term is key, and it is easy to see that it has two bulk minima at $\phi \pm 1$ for $A > 0$. When $A < 0$ the two fluids are miscible. Extensions to more than two fluid components have also been proposed, in particular for ternary systems [43, 62, 63]. The final term, the gradient term, accounts for surface tension.

Let us consider the fluid-fluid interface and derive an analytical expression for both the surface tension and the interface width. Taking the functional derivative of the free energy in (9.68) with respect to ϕ leads to an equation for the *chemical potential*:

$$\mu \equiv \frac{\delta(\psi_\mathrm{b} + \psi_\mathrm{g})}{\delta\phi} = -A\phi + A\phi^3 - \kappa\Delta\phi = \text{const.} \tag{9.69}$$

We know that in equilibrium the chemical potential must be constant in space. Otherwise there would be a thermodynamic force density corresponding to $\boldsymbol{F} = -\phi\nabla\mu$. We can set the constant in the above equation to zero, $\mu = 0$, by taking the bulk behaviour of fluids 1 or 2, where $\phi = \pm 1$ and $\Delta\phi = 0$.

For simplicity, we shall now assume that the interface between the two fluids is flat and located at $x = 0$. The bulk behaviour at $x = \pm\infty$ is such that $\phi = \pm 1$, respectively.

Equation (9.69) allows an **interface solution** of the form

$$\phi = \tanh\left(\frac{x}{\sqrt{2}\xi}\right) \tag{9.70}$$

where $\xi = \sqrt{\kappa/A}$ is defined as the **interface width**. The **surface tension** of the interface between fluids 1 and 2 can then be calculated by integrating the free energy density across the interface. Using (9.70) for the order parameter profile, we obtain

$$\gamma_{12} = \int_{-\infty}^{\infty}\left[\frac{A}{4}\left(\phi^2 - 1\right)^2 + \frac{\kappa}{2}(\nabla\phi)^2\right]\mathrm{d}x = \sqrt{\frac{8\kappa A}{9}}. \tag{9.71}$$

9.2.2.2 Surface Thermodynamics

To account for the interactions between the fluids and the solid, here we can prescribe a surface energy contribution given by [59]

$$\Psi_\mathrm{s} = \int_A \psi_\mathrm{s}\,\mathrm{d}A = -\int_A h\phi_\mathrm{s}\,\mathrm{d}A \tag{9.72}$$

where ϕ_s is the value of the order parameter at the surface and the integral is taken over the system's solid surface. The readers will notice that this has the same form as for the liquid-gas model, except that ψ_s now depends on the order parameter ϕ, and not the density.

Minimisation of the total free energy functional with respect to ϕ at the solid boundary leads to a Neumann boundary condition in the gradient of order parameter ϕ:

$$\kappa(\nabla\phi\cdot\hat{\boldsymbol{n}}) = \kappa\nabla_\perp\phi = h. \tag{9.73}$$

The important consequence of this equation is that the contact angle of the surface can be implemented by setting the perpendicular derivative of the order parameter. In our convention, the normal unit vector is pointing outward, into the solid. We

leave the derivation of (9.73) to the readers since the mathematical steps are identical to those for the liquid-gas model in Sect. 9.2.1.

The variable h can be used to tune the contact angle. For $h > 0$, fluid 1 interacts favourably with the solid (more wetting) compared to fluid 2. The opposite is true for $h < 0$. To derive an explicit relation between the variable h and the contact angle θ, we can exploit Noether's theorem [60]

$$\frac{\delta(\psi_\mathrm{b} + \psi_\mathrm{g})}{\delta(\nabla\phi)} \cdot \nabla\phi - (\psi_\mathrm{b} + \psi_\mathrm{g}) = \text{const} \tag{9.74}$$

to show that

$$\frac{\kappa}{2}(\nabla\phi)^2 - \frac{A}{4}\left(\phi^2 - 1\right)^2 = \text{const} = 0. \tag{9.75}$$

In the last step, we have used the fact that far from the interface (in the bulk), $\phi = \pm 1$ and $\nabla\phi = \mathbf{0}$.

Substituting (9.73) into (9.75), we find that the values of the order parameter at the surface may take four possible values: $\phi_\mathrm{s} = \pm(1 \pm (2h^2/\kappa A)^{1/2})^{1/2}$. To decide which solutions are physically admissible, let us consider the following arguments. For fluid 1, the bulk solution is given by $\phi = 1$. If $h > 0$, there is an energy gain for having higher concentration of fluid 1 at the solid surface such that the order parameter for fluid 1 at the solid surface $\phi_{\mathrm{s}1} > 1$. On the other hand, if $h < 0$, it is favourable to have $\phi_{\mathrm{s}1} < 1$. A solution satisfying this requirement is

$$\phi_{\mathrm{s}1} = +\sqrt{1 + \sqrt{\frac{2}{\kappa A}}h}. \tag{9.76}$$

Using similar arguments, we can conclude that for fluid 2, the order parameter at the solid surface is

$$\phi_{\mathrm{s}2} = -\sqrt{1 - \sqrt{\frac{2}{\kappa A}}h}. \tag{9.77}$$

The fluid-solid surface tensions can be calculated in a similar way to the fluid-fluid surface tension, except that now we also have to take into account the contributions from the surface energy term. For the tension between fluid 1 and the solid surface, assuming a flat interface at $x = 0$, we have

$$\gamma_{\mathrm{s}1} = -h\phi_{\mathrm{s}1} + \int_0^\infty \left[\frac{A}{4}\left(\phi^2 - 1\right)^2 + \frac{\kappa}{2}(\nabla\phi)^2\right] \mathrm{d}x. \tag{9.78}$$

To evaluate this integral, we take advantage of Noether's theorem in (9.75) and introduce a change of variables:

$$\int_0^\infty \left[\frac{A}{4}\left(\phi^2 - 1\right)^2 + \frac{\kappa}{2}\left(\frac{\mathrm{d}\phi}{\mathrm{d}x}\right)^2\right] \mathrm{d}x = \int_{\phi_{\mathrm{s}1}}^1 \left[\sqrt{\frac{A\kappa}{2}}\left(1 - \phi^2\right)\right] \mathrm{d}\phi. \tag{9.79}$$

Using the definition of ϕ_{s1} given in (9.76), it is straightforward to show that

$$\gamma_{s1} = \frac{\gamma_{12}}{2}\left[1 - (1+\Omega)^{3/2}\right] \tag{9.80}$$

where $\Omega = h\sqrt{2/(\kappa A)}$ and $\gamma_{12} = \sqrt{8\kappa A/9}$. The surface tension between fluid 2 and the solid can be derived in a similar way, and we obtain

$$\gamma_{s2} = \frac{\gamma_{12}}{2}\left[1 - (1-\Omega)^{3/2}\right]. \tag{9.81}$$

The contact angle follows from substituting the values of the surface tensions into Young's law, (9.9), to give (with θ defined as the contact angle of fluid 1)

$$\cos\theta = \frac{\gamma_{s2} - \gamma_{s1}}{\gamma_{12}} = \frac{(1+\Omega)^{3/2} - (1-\Omega)^{3/2}}{2}. \tag{9.82}$$

Equation (9.82) can be inverted to give a relation between the phenomenological parameter Ω and the equilibrium contact angle θ:

$$\Omega = 2\,\mathrm{sgn}(\pi/2 - \theta)\sqrt{\cos(\alpha/3)\left[1 - \cos(\alpha/3)\right]} \tag{9.83}$$

where $\alpha(\theta) = \arccos(\sin^2\theta)$ and the function $\mathrm{sgn}(x)$ returns the sign of x. This is exactly the same equation as in (9.63), except for the definition of $\Omega = h\sqrt{2/(\kappa A)}$ in the multicomponent model.

9.2.2.3 Equations of Motion

Before we write down the LB equations for a binary fluid, let us review the corresponding continuum equations of motion. The fluid motion is described by the continuity and Navier-Stokes equations, as described in (9.27) and (9.28). The key additional physics due to the thermodynamics of a binary fluid is contained in the *pressure tensor*. The pressure tensor needs to satisfy the condition

$$\partial_\beta P_{\alpha\beta} = \rho\partial_\alpha\left[\frac{\delta(\psi_b + \psi_g)}{\delta\rho}\right] + \phi\partial_\alpha\left[\frac{\delta(\psi_b + \psi_g)}{\delta\phi}\right]. \tag{9.84}$$

This is a generalisation of (9.29), where in principle we now have two variables, the density ρ and the order parameter ϕ, which can vary in space. This equation can be simplified to

$$\partial_\beta P_{\alpha\beta} = \partial_\alpha(c_s^2\rho) + \phi\partial_\alpha\mu. \tag{9.85}$$

The first term has the same form as the hydrodynamic pressure for the standard lattice Boltzmann model. The thermodynamic of the multicomponent model is contained in the second term. We remind the reader that, in thermodynamic equilibrium, the chemical potential has to be the same everywhere. Any inhomogeneity leads to a body force proportional to the gradient of the chemical potential, driving the system to equilibrium. Using the definition of μ in (9.69), it follows that

$$P_{\alpha\beta} = \left(p_\mathrm{b} - \frac{\kappa}{2}(\partial_\gamma \phi)^2 - \kappa\phi\partial_\gamma\partial_\gamma\phi\right)\delta_{\alpha\beta} + \kappa(\partial_\alpha\phi)(\partial_\beta\phi), \tag{9.86}$$

$$p_\mathrm{b} = c_\mathrm{s}^2\rho + A\left(-\frac{1}{2}\phi^2 + \frac{3}{4}\phi^4\right). \tag{9.87}$$

Equation (9.87) is the *equation of state* for the binary fluid model. p_b can be interpreted as the bulk pressure far from the interface, where the gradient terms are zero. In this model, the value of ϕ usually deviates slightly from ± 1 in the bulk when there is a Laplace pressure difference between the two fluid domains.

The order parameter itself evolves through the **Cahn-Hilliard equation**

$$\frac{\partial\phi}{\partial t} + \nabla\cdot(\phi\boldsymbol{u}) = \nabla\cdot\left(M\nabla\mu\right). \tag{9.88}$$

This equation is also sometimes called the *interface-capturing equation* in multicomponent flows. The second term on the left-hand side is an advection term, where the order parameter moves along with the fluid. The diffusive term on the right-hand side accounts for the motion of the order parameter due to inhomogeneities in the chemical potential. In many cases, the mobility parameter M is taken to be constant, although in general it is a function of the fluid order parameter [64, 65]. The mobility parameter is also important in the context of contact line motion, as it controls the effective contact line slip length [66].

9.2.2.4 The Lattice Boltzmann Algorithm

We now describe an LB algorithm that solves (9.27), (9.28), and (9.88). For a binary fluid, we need to define two distribution functions, $f_i(\boldsymbol{x}, t)$ and $g_i(\boldsymbol{x}, t)$, corresponding to the density and relative concentration of the two fluids. The physical variables are related to the distribution functions by

$$\rho = \sum_i f_i, \quad \rho u_\alpha = \sum_i f_i c_{i\alpha} + \frac{F_\alpha \Delta t}{2}, \quad \phi = \sum_i g_i, \tag{9.89}$$

Here we have chosen to evolve both the density and the order parameter using LBM. This is not a requirement at all. It is possible to solve the continuity and Navier-Stokes equations using LBM (via the $f_i(\boldsymbol{x}, t)$ only), and solve the Cahn-Hilliard equation using a different method (e.g. finite difference).

The equations of motion for multicomponent flows are similar to those for advection-diffusion systems described in Chap. 8. As usual, the LB algorithm for multicomponent flows can be broken into two steps. For simplicity, we here use the BGK collision operator. Extensions to the MRT collision operator follow the same route as described in Chap. 10. The collision and propagation steps read

$$\begin{aligned} f_i^\star(\boldsymbol{x}, t) &= f_i(\boldsymbol{x}, t) - \frac{\Delta t}{\tau}(f_i(\boldsymbol{x}, t) - f^{\mathrm{eq}_i}(\boldsymbol{x}, t)) + \left(1 - \frac{\Delta t}{2\tau}\right) F_i(\boldsymbol{x}, t)\Delta t, \\ g_i^\star(\boldsymbol{x}, t) &= g_i(\boldsymbol{x}, t) - \frac{\Delta t}{\tau_\phi}\left(g_i(\boldsymbol{x}, t) - g_i^{\mathrm{eq}}(\boldsymbol{x}, t)\right). \end{aligned} \tag{9.90}$$

and

$$\begin{aligned} f_i(\boldsymbol{x} + \boldsymbol{c}_i\Delta t, t + \Delta t) &= f_i^\star(\boldsymbol{x}, t), \\ g_i(\boldsymbol{x} + \boldsymbol{c}_i\Delta t, t + \Delta t) &= g_i^\star(\boldsymbol{x}, t). \end{aligned} \tag{9.91}$$

f_i^{eq} and g_i^{eq} are local equilibrium distribution functions. The relaxation parameters τ and τ_ϕ are related to the transport coefficients ν and M in the hydrodynamic equations through

$$\nu = c_{\mathrm{s}}^2\left(\tau - \frac{\Delta t}{2}\right), \tag{9.92}$$

$$M = \Gamma\left(\tau_\phi - \frac{\Delta t}{2}\right) \tag{9.93}$$

where Γ is a tunable parameter that appears in the equilibrium distribution as shown below. Since ν and M are positive quantities, the values of the relaxation times τ and τ_ϕ have to be larger than $\Delta t/2$.

Like for the one-component multiphase flows, the physics of surface tension can be implemented in two different ways. The first approach is to modify the equilibrium distribution functions f_i^{eq} to fully represent the pressure tensor. The suitable form of f_i^{eq} for $i \neq 0$ is given by

$$\begin{aligned} f_i^{\mathrm{eq}} = w_i\rho\left(1 + \frac{c_{i\alpha}u_\alpha}{c_{\mathrm{s}}^2} + \frac{u_\alpha u_\beta\left(c_{i\alpha}c_{i\beta} - c_{\mathrm{s}}^2\delta_{\alpha\beta}\right)}{2c_{\mathrm{s}}^4}\right) \\ + \frac{w_i}{c_{\mathrm{s}}^2}\left(p_{\mathrm{b}} - c_{\mathrm{s}}^2\rho - \kappa\phi\Delta\phi\right) + \kappa\sum_{\alpha,\beta} w_i^{\alpha\beta}(\partial_\alpha\phi)(\partial_\beta\phi). \end{aligned} \tag{9.94}$$

The form of (9.94) is similar to that of the equivalent equation for the liquid-gas model in (9.36). The difference is that now p_{b} is given by (9.87), and the

relevant gradient terms are for the order parameter ϕ rather than for the density ρ. The derivatives are usually approximated through finite difference schemes. The equilibrium distribution function for $i = 0$ can be obtained by exploiting conservation of mass, such that

$$f_0^{\text{eq}} = \rho - \sum_{i \neq 0} f_i^{\text{eq}}. \tag{9.95}$$

The second approach is to implement a forcing term. As already discussed in Sect. 9.2.1 for a multiphase fluid, this can be done by either using the pressure form, $F_\alpha = -\partial_\beta (P_{\alpha\beta} - c_s^2 \rho \delta_{\alpha\beta})$, or the potential form, $F_\alpha = -\phi \partial_\alpha \mu$. Remember that $\partial_\beta P_{\alpha\beta} = \partial_\alpha c_s^2 \rho + \phi \partial_\alpha \mu$, as given in (9.85). Since the derivatives of the order parameter (mostly obtained through a finite difference scheme) are only approximate, these two forms are not exactly identical numerically, therefore resulting in a loss of exact momentum conservation in the LB scheme.

The potential form requires the computation of third-order derivatives of the order parameter which are expensive to compute if we want to maintain accuracy. To alleviate this issue, a common mathematical trick is to rewrite the derivative of the pressure tensor as [13, 67]

$$\partial_\beta P_{\alpha\beta} = \partial_\alpha c_s^2 \rho + \phi \partial_\alpha \mu = \partial_\alpha \left(c_s^2 \rho + \phi \mu \right) - \mu \partial_\alpha \phi. \tag{9.96}$$

Thus, a possible hybrid approach is (i) to modify the equilibrium distribution functions to account for the bulk pressure term corresponding to $c_s^2 \rho + \phi \mu$ and (ii) to introduce a forcing term given by $F_\alpha = \mu \partial_\alpha \phi$. In this case, the suitable equilibrium distribution functions for $i \neq 0$ are

$$f_i^{\text{eq}} = w_i \rho \left(1 + \frac{\phi \mu}{\rho c_s^2} + \frac{c_{i\alpha} u_\alpha}{c_s^2} + \frac{u_\alpha u_\beta \left(c_{i\alpha} c_{i\beta} - c_s^2 \delta_{\alpha\beta} \right)}{2 c_s^4} \right). \tag{9.97}$$

For the equilibrium distribution function g_i^{eq} of the order parameter, a comparison with (8.29) is appropriate. The key difference between the advection-diffusion equation in Chap. 8 and the Cahn-Hilliard equation is in the form of the diffusion term. For the latter, we have a term that is proportional to $\Delta \mu$, whereas for the former ΔC where C is the concentration. As such, the equilibrium distribution function g_i^{eq} has to obey

$$\begin{aligned} \sum_i g_i^{\text{eq}} &= \phi, \\ \sum_i g_i^{\text{eq}} c_{i\alpha} &= \phi u_\alpha, \\ \sum_i g_i^{\text{eq}} c_{i\alpha} c_{i\beta} &= \Gamma \mu \delta_{\alpha\beta} + \phi u_\alpha u_\beta. \end{aligned} \tag{9.98}$$

The form of g_i^{eq} that satisfies these conditions is

$$g_i^{\mathrm{eq}} = w_i \left(\frac{\Gamma \mu}{c_\mathrm{s}^2} + \frac{\phi u_\alpha c_{i\alpha}}{c_\mathrm{s}^2} + \frac{\phi u_\alpha u_\beta \left(c_{i\alpha} c_{i\beta} - c_\mathrm{s}^2 \delta_{\alpha\beta} \right)}{2 c_\mathrm{s}^4} \right) \quad (i \neq 0) \tag{9.99}$$

and

$$g_0^{\mathrm{eq}} = \phi - \sum_{i \neq 0} g_i^{\mathrm{eq}}. \tag{9.100}$$

Compared to (8.26), the key difference is the term $\Gamma \mu / c_\mathrm{s}^2$ in (9.99). For the Cahn-Hilliard equation, we have $\Gamma \mu$ rather than the concentration C in the advection-diffusion equation.

9.2.2.5 A Practical Guide to Simulation Parameters

The Landau free-energy model for a binary fluid is simple. There are only two free parameters: κ and A. They can be varied to tune the interface width $\xi = \sqrt{\kappa / A}$ and the surface tension $\gamma_{12} = \sqrt{(8\kappa A)/9}$. Similar to the liquid-gas model, the interface width is usually chosen to be $\sim 2 - 3$ lattice spacings, and the surface tension (in lattice units) is limited to $\gamma_{12} = O(10^{-2})$ or less due to the presence of spurious velocities.

For the binary model, we also have to choose the values of Γ and τ_ϕ which control the mobility parameter M in the Cahn-Hilliard equation via $M = \Gamma (\tau_\phi - \Delta t/2)$. A common practice is to set $\tau_\phi = \Delta t$ such that the distribution functions for $g_i(\boldsymbol{x}, t)$ are always relaxed to equilibrium, which simplifies the algorithm. The parameter Γ can be varied across a wide range of values, typically $\Gamma = 10^{-2} - 10$, while keeping the simulation stable.

Exercise 9.7 Repeat the Laplace pressure and contact angle benchmarks, as discussed in Exercises 9.5 and 9.6, for the binary fluid model.

9.3 Shan-Chen Pseudopotential Method

As we have discussed in Sect. 9.1, there are several ways to model multiphase or multicomponent flows within the LBM. For example, in Sect. 9.2 we described the commonly used free-energy method, a "top-down" approach. We started with a *macroscopic* concept, the free energy, and ended up with a force that can lead to phase separation.

Another way is to introduce a "bottom-up" approach by, e.g., postulating a *microscopic* interaction between fluid elements. This could be in the form of

interaction potentials that eventually lead to the macroscopic separation of phases. Historically, this is how the *Shan-Chen (SC) model* was presented [68, 69].

The advantage of the SC approach is its intrinsic simplicity and mesoscopic nature. Surface tension is an emergent effect. This is akin to the LBM itself: LBM is based on simple mesoscopic rules with emergent transport coefficients, in particular the fluid viscosity. Additionally, for the multicomponent model, each of several different population sets directly represents a fluid component. This is a very intuitive approach to multicomponent physics, perhaps more so than the phase order parameters for free energy.

To keep this overview accessible also to an inexperienced audience, we omit technical details and refer to the literature instead. For example, for a deep explanation of the bottom-up approach, we encourage the reader to study [70]. We also recommend going through general SC review articles, such as [12, 13]. The earlier articles about the method, e.g. [68, 69, 71], are well worth reading.

We will start by explaining the general SC concepts in Sect. 9.3.1. Then we will distinguish between the two most important special cases: SC for a single-component multiphase system (e.g. liquid water and water vapour) in Sect. 9.3.2 and SC for a multicomponent system without phase change (e.g. a water-oil mixture) in Sect. 9.3.3. An overview of limitations and available extensions of the SC method (and the free-energy method), such as spurious currents and limited density ratio, will be discussed in Sect. 9.4.

9.3.1 General Considerations

In the following we will motivate the SC model and show fundamental concepts and equations. We will provide the basis for both the multiphase and the multicomponent cases that are covered in Sect. 9.3.2 and Sect. 9.3.3, respectively.

As a multiphase example, the coexistence of a liquid and a gas phase is caused by an attractive force between molecules in the liquid phase. The strength of this intermolecular force is tightly related to the boiling point and the vapour pressure of the liquid. For example, the dipolar molecules of water show a strong intermolecular interaction that leads to a relatively high boiling point of 100°C at normal pressure. Methane molecules, on the other hand, do not have a permanent dipole, and the attraction between CH_4 molecules is much weaker. As such, the boiling point of methane at -162°C is much lower compared to water.

Furthermore, different molecules in a multicomponent mixture (e.g. oil and water) interact differently with each other: the interaction between two water molecules is different from the interaction of two oil molecules or even between a water and an oil molecule.

These considerations raise the question of whether it is possible to simulate liquid-vapour or multicomponent systems by introducing a suitable local interaction force between fluid elements. In fact, this is exactly the underlying idea of the SC model. We will see shortly that the addition of a relatively simple interaction force

defined at lattice nodes can be used to model both multiphase and multicomponent systems with or without surface tension. Of course, not every interaction force is suitable for this purpose.

Ideally, for multiphase systems, the force should have a thermodynamically consistent form, i.e. the values of the pressure and the equilibrium densities for a given temperature should be the same as those derived from thermodynamic principles using the Maxwell area construction rule (cf. Sect. 9.1). We will get back to this in Sect. 9.3.2.

Even if we find a suitable force in terms of thermodynamic consistency, it is not guaranteed that its discretised form allows for stable simulations. It is known that large surface tensions or large liquid-gas density ratios can lead to numerically "stiff" forces that cause negative LB populations and therefore instability [12].

In what follows we focus on a multiphase system for simplicity, but the results can be extended to multicomponent problems. In order to find a functional form for the interaction force, we have to consider its origin. We can assume that intermolecular forces act between pairs of molecules and are additive. Therefore, a higher density of molecules will lead to stronger forces. As a consequence, we expect that the magnitude of the interaction between fluid elements at $\boldsymbol{x}$ and $\tilde{\boldsymbol{x}} \neq \boldsymbol{x}$ is proportional to $\rho(\boldsymbol{x})\rho(\tilde{\boldsymbol{x}})$. Additionally, the interaction is a strong function of the distance between the fluid elements. We can thus introduce a kernel function $G(\boldsymbol{x}, \tilde{\boldsymbol{x}})$ that carries the information about the spatial dependency of the force. Also, the total force acting on a fluid element at $\boldsymbol{x}$ is the integral over all possible interaction sites $\tilde{\boldsymbol{x}}$. We can finally write the interaction force density at $\boldsymbol{x}$ as [68, 72]

$$\boldsymbol{F}^{\mathrm{SC}}(\boldsymbol{x}) = -\int (\tilde{\boldsymbol{x}} - \boldsymbol{x})\, G(\boldsymbol{x}, \tilde{\boldsymbol{x}})\psi(\boldsymbol{x})\psi(\tilde{\boldsymbol{x}})\, \mathrm{d}^3\tilde{x}. \tag{9.101}$$

Here we have replaced the density ρ by an effective density function ψ that is also called the *pseudopotential*. The prefix "pseudo" indicates that ψ represents an effective density, rather than the fluid density ρ.

The reason for using ψ rather than ρ is the possible numerical instability mentioned earlier. A widely accepted and often used form of the pseudopotential is

$$\psi(\rho) = \rho_0 \left[1 - \exp(-\rho/\rho_0)\right] \tag{9.102}$$

with a reference density ρ_0 that in simulation units is mostly set to unity. The pseudopotential in (9.102) is bounded between 0 and ρ_0 for any value of the density ρ. Therefore, the interaction force in (9.101) remains finite, even for large densities.

Exercise 9.8 By performing a Taylor expansion, show that $\psi(\rho) \approx \rho$ for $\rho \ll \rho_0$.

Another common form of the pseudopotential is simply the fluid density itself:

$$\psi(\rho) = \rho. \tag{9.103}$$

In this case there is no bound, and the interaction force in (9.101) can diverge for large ρ. There are even more functional forms in use throughout the literature (cf. Sect. 9.4).

The next step is the spatial discretisation of (9.101). This means that we want to restrict $\boldsymbol{x}$ and $\tilde{\boldsymbol{x}}$ to lattice nodes. Furthermore, we claim that the interaction force is short-ranged, i.e. fluid elements at $\boldsymbol{x}$ only interact with other fluid elements at $\tilde{\boldsymbol{x}}$ that are in the vicinity. Therefore, $G(\boldsymbol{x}, \tilde{\boldsymbol{x}}) = 0$ for sufficiently large $|\boldsymbol{x} - \tilde{\boldsymbol{x}}|$. Finally, $G(\boldsymbol{x}, \tilde{\boldsymbol{x}})$ should be isotropic and therefore a function of $|\boldsymbol{x} - \tilde{\boldsymbol{x}}|$ only.

There exist different discretisations for $G(\boldsymbol{x}, \tilde{\boldsymbol{x}})$ [72, 73], but the most common involves interactions between lattice nodes that are connected by one of the vectors $\boldsymbol{c}_i \Delta t$ [74, 75]:

$$G(\boldsymbol{x}, \tilde{\boldsymbol{x}}) = \begin{cases} w_i G & \text{for } \tilde{\boldsymbol{x}} = \boldsymbol{x} + \boldsymbol{c}_i \Delta t, \\ 0 & \text{otherwise.} \end{cases} \tag{9.104}$$

The simplest form of the **discretised Shan-Chen force for a single component** is represented through a sum of pseudopotential interactions with nearest lattice neighbours [68]:

$$\boldsymbol{F}^{\mathrm{SC}}(\boldsymbol{x}) = -\psi(\boldsymbol{x}) G \sum_i w_i \psi(\boldsymbol{x} + \boldsymbol{c}_i \Delta t) \boldsymbol{c}_i \Delta t. \tag{9.105}$$

The sum runs over all velocities $\boldsymbol{c}_i$ of the underlying lattice (e.g. D2Q9 or D3Q19, as illustrated in Fig. 9.8) and the w_i are the usual lattice weights. The pseudopotential $\psi(\boldsymbol{x})$ is given by (9.102) or (9.103). The coefficient G is a simple scalar that controls the strength of the interaction. It is attractive for negative and repulsive for positive G. A more mathematical and thermodynamic rationale for this force will be provided in Sect. 9.3.2.

Exercise 9.9 The SC model violates *local momentum* conservation as the interaction force is not local. Show that the *global momentum* is conserved when the system is fully periodic. Use the fact that the interaction force between two fluid elements at $\boldsymbol{x}$ and $\tilde{\boldsymbol{x}}$ satisfies Newton's third law.

The SC model can be easily extended to systems with S fluid components. In this case, we label different components (e.g. water and oil) with the indices $1 \leq \sigma, \tilde{\sigma} \leq S$ and write

$$\boldsymbol{F}^{\mathrm{SC}(\sigma)}(\boldsymbol{x}) = -\psi^{(\sigma)}(\boldsymbol{x}) \sum_{\tilde{\sigma}} G_{\sigma\tilde{\sigma}} \sum_i w_i \psi^{(\tilde{\sigma})}(\boldsymbol{x} + \boldsymbol{c}_i \Delta t) \boldsymbol{c}_i \Delta t \tag{9.106}$$

for the force density acting on component σ at location $\boldsymbol{x}$. The new sum runs over all S values of $\tilde{\sigma}$, including $\tilde{\sigma} = \sigma$. The coefficients $G_{\sigma\tilde{\sigma}} = G_{\tilde{\sigma}\sigma}$ with $\tilde{\sigma} \neq \sigma$

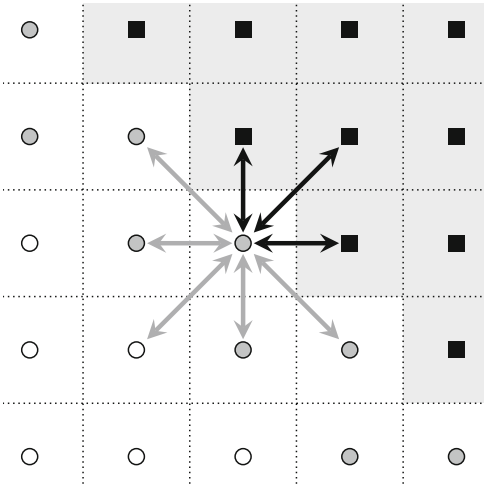

Fig. 9.8 The Shan-Chen force is often implemented along node pairs that are connected through one of the lattice vectors $\boldsymbol{c}_i \Delta t$. In D2Q9, the central node interacts with its eight neighbours, as indicated by the *arrows*. These nodes can be in the fluid region (*circles*) or in the solid region (*squares*; cf. Sect. 9.3.2 and Sect. 9.3.3 for more details about the treatment of solid boundaries). To be consistent with the remainder of this book, we distinguish between fluid nodes (*white*) and boundary nodes (*grey*), the latter being neighbours of at least one solid node

denote the molecular *interactions between different fluid components*. Those are often repulsive. Each of the fluid components can potentially self-interact; this is captured by the coefficients $G_{\sigma\sigma}$. The SC model in (9.106) may thus be used to model a mixture of two (or more) fluids that could all exist in the liquid and gas phases, i.e. a multicomponent-multiphase system.

In Sect. 9.3.2 we will discuss in more detail how to use the SC model to simulate a multiphase system with a single component (i.e. $S = 1$ and $G = G_{11} \neq 0$), while in Sect. 9.3.3 we will discuss multicomponent systems without phase change (i.e. $S > 1$ and $G_{\sigma\sigma} = 0$). We will not consider multicomponent-multiphase problems in this book (i.e. problems with $S > 1$ *and* $G_{\sigma\sigma} \neq 0$). Those systems are investigated in [76] and reviewed in section 6 in [12].

9.3.2 Multiphase Model for Single Component

Here we deal with a single fluid component that can coexist in two phases, e.g. liquid water and water vapour. First we will investigate the physical content of the SC model in (9.105) and show how it can lead to phase separation and surface tension. We will then take a closer look at a planar interface and discuss the issue of thermodynamic consistency within the SC model. Later we will present how solid boundaries with given wetting properties can be simulated. After providing a

summary of the algorithm for SC multiphase systems, we show a classical example: the Young-Laplace test to obtain the surface tension from the pressure jump across the interface of a droplet.

9.3.2.1 Physical Interpretation and Equation of State

In Sect. 9.3.1 we argued that the liquid-vapour coexistence is caused by an attractive interaction between fluid molecules. The SC model in (9.105) is one possible realisation of an attractive interaction (for negative G) between neighbouring lattice nodes. Since the equation of state dictates the physical behaviour of the liquid-vapour system, the key question is which equation of state corresponds to the SC force.

In the original works of Shan and Chen [68, 72], the equilibrium distribution f_i^{eq} is taken in its usual form from (3.54). This means that the bulk pressure, i.e. far away from any interfaces, obeys the isothermal form of the ideal equation of state, $p_{\mathrm{b}} = c_{\mathrm{s}}^2 \rho$ (cf. Sect. 1.1.3). From thermodynamics we know that the ideal equation of state cannot invoke liquid-vapour coexistence. Therefore, the SC equation of state must include additional terms. In fact, the desired phase separation is linked to the SC force, as we will now investigate in more detail.

Let us first Taylor-expand the pseudopotential $\psi(\boldsymbol{x} + \boldsymbol{c}_i \Delta t)$ about $\boldsymbol{x}$:

$$\psi(\boldsymbol{x} + \boldsymbol{c}_i \Delta t) = \psi(\boldsymbol{x}) + c_{i\alpha} \Delta t \partial_\alpha \psi(\boldsymbol{x}) + \frac{1}{2} c_{i\alpha} c_{i\beta} \Delta t^2 \partial_\alpha \partial_\beta \psi(\boldsymbol{x}) + \frac{1}{6} c_{i\alpha} c_{i\beta} c_{i\gamma} \Delta t^3 \partial_\alpha \partial_\beta \partial_\gamma \psi(\boldsymbol{x}) + \ldots \tag{9.107}$$

Substituting this into (9.105) gives

$$\boldsymbol{F}^{\mathrm{SC}}(\boldsymbol{x}) = -G\psi(\boldsymbol{x}) \sum_i w_i \boldsymbol{c}_i \Delta t \Big(\psi(\boldsymbol{x}) + c_{i\alpha} \Delta t \partial_\alpha \psi(\boldsymbol{x}) + \frac{1}{2} c_{i\alpha} c_{i\beta} \Delta t^2 \partial_\alpha \partial_\beta \psi(\boldsymbol{x}) + \ldots \Big). \tag{9.108}$$

Due to the symmetry of the velocity sets, shown in (3.60), the terms $\sum_i w_i \boldsymbol{c}_i$ and $\sum_i w_i \boldsymbol{c}_i c_{i\alpha} c_{i\beta}$ vanish.

Including expansion terms from (9.107) up to third order, the **continuum form of the Shan-Chen force** becomes [77]

$$\boldsymbol{F}^{\mathrm{SC}}(\boldsymbol{x}) = -G\psi(\boldsymbol{x}) \left(c_{\mathrm{s}}^2 \Delta t^2 \nabla \psi(\boldsymbol{x}) + \frac{c_{\mathrm{s}}^4 \Delta t^4}{2} \nabla \Delta \psi(\boldsymbol{x}) \right). \tag{9.109}$$

Exercise 9.10 Derive (9.109) by taking advantage of (3.60) for the moments of the weights w_i. Note that the result in (9.109) generally depends on the underlying lattice structure.

The first term on the right-hand side of (9.109) has the form of a gradient:

$$-c_s^2 \Delta t^2 G \psi(\boldsymbol{x}) \nabla \psi(\boldsymbol{x}) = -\frac{c_s^2 \Delta t^2 G}{2} \nabla \psi^2(\boldsymbol{x}). \tag{9.110}$$

Therefore we can include it in the equation of state.

The **equation of state of the multiphase SC model** in (9.105) is

$$p_b(\rho) = c_s^2 \rho + \frac{c_s^2 \Delta t^2 G}{2} \psi^2(\rho). \tag{9.111}$$

The SC contribution leads to a non-ideal term that allows for the coexistence of a liquid and a vapour phase.

Exercise 9.11 Plot the bulk pressure $p_b(\rho)$ from (9.111) with the pseudopotential in (9.102). For the sake of simplicity, set $\rho_0 = 1$, $c_s^2 = 1/3$ and $\Delta t = 1$. Show that, if $G < -4$, there exist two distinct density values for a given pressure value, i.e. gas and liquid with respective densities ρ_g and ρ_l can coexist. What happens for $G \geq -4$?

The second term proportional to $G\psi \nabla \Delta \psi$ in (9.109) looks nearly like the surface tension term $k\rho \nabla \Delta \rho$ in (9.12). Obviously, we expect deviations when $\psi \neq \rho$.

One can show that the SC pressure tensor $\boldsymbol{P}^{SC}$, which is defined by $\nabla \cdot \boldsymbol{P}^{SC} = \nabla(c_s^2 \rho) - \boldsymbol{F}^{SC}$ and has been introduced in Sect. 9.1, assumes the form (setting $\Delta t = 1$ for simplicity) [77]

$$P_{\alpha\beta}^{SC} = \left(c_s^2 \rho + \frac{c_s^2 G}{2} \psi^2 + \frac{c_s^4 G}{4} (\nabla \psi)^2 + \frac{c_s^4 G}{2} \psi \Delta \psi \right) \delta_{\alpha\beta} - \frac{c_s^4 G}{2} (\partial_\alpha \psi)(\partial_\beta \psi). \tag{9.112}$$

This pressure tensor differs from the thermodynamically consistent pressure tensor in (9.30). However, the resulting surface tension behaviour and the density profiles are acceptable for many practical purposes. Furthermore, there exist modifications of the SC model that allow for improved thermodynamic consistency (cf. Sect. 9.4).

The **Shan-Chen force** from (9.105) introduces two terms in the Navier-Stokes equation: one leads to a **non-ideal equation of state**, (9.111), the other acts

(continued)

like a **surface tension** from (9.12). The single parameter G, which appears in both terms, can be changed to control the phase separation. This is the reason why G is sometimes referred to as a **temperature-like parameter**.

9.3.2.2 Planar Interface and Thermodynamic Consistency

A suitable test for checking thermodynamical consistency is the planar interface between phases. For the free-energy liquid-gas model, the density profile across the interface satisfies the Maxwell area construction rule, cf. Appendix A.7. Yet, we have to investigate thermodynamic consistency in the context of the SC model. Below we collect the final results of the calculations, with algebraic details shown in Appendix A.8.

For the **Shan-Chen model**, there is an expression similar to the **Maxwell area construction rule** that allows to obtain the phase transition densities. The coexistence pressure is

$$p_0 = c_s^2 \rho_g + \frac{c_s^2 \Delta t^2 G}{2} \psi^2(\rho_g) = c_s^2 \rho_l + \frac{c_s^2 \Delta t^2 G}{2} \psi^2(\rho_l). \tag{9.113}$$

where the liquid and gas densities ρ_l and ρ_g obey

$$\int_{\rho_g}^{\rho_l} \left(p_0 - c_s^2 \tilde{\rho} - \frac{c_s^2 \Delta t^2 G}{2} \psi^2(\tilde{\rho}) \right) \frac{\psi'(\tilde{\rho})}{\psi^2(\tilde{\rho})} \mathrm{d}\tilde{\rho} = 0. \tag{9.114}$$

Instead of having the multiplier $1/\tilde{\rho}^2$ in the thermodynamically consistent model in (9.7), we now have an expression depending on the pseudopotential and its derivative, $\psi'(\rho)/\psi^2(\rho)$, with $\psi' = \mathrm{d}\psi/\mathrm{d}\rho$.

The obvious choice to satisfy the thermodynamic consistency is $\psi \propto \rho$. However, for large liquid-gas density ratios this leads to large gradients and eventually numerical instability. In Sect. 9.4.2 we show how to choose different equations of state. For the van der Waals equation of state, for example, the achievable liquid-gas density ratio with $\psi \propto \rho$ is around 10. However, reverting to the exponential pseudopotential in (9.102) for the same equation of state allows increasing the liquid-gas density ratio by an additional factor of 3–5.

Although the expressions for the Maxwell area construction rule and its SC equivalent are different, the phase separation densities ρ_l and ρ_g for the particular equation of state in (9.111) are *similar* to their thermodynamically consistent

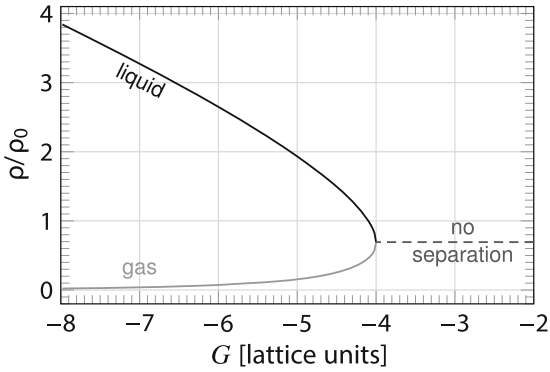

Fig. 9.9 Phase separation densities for (9.111) with the pseudopotential in (9.102) versus the temperature-like parameter G (in lattice units). The densities represent the solution of (9.114)

counterparts in many situations. More particular examples of possible equations of state are given in [78]. The Peng-Robinson and Carnahan-Sterling equations of state give practically the same gas and liquid density values while the results obtained from the van der Waals equation of state are significantly different.

In Fig. 9.9 we present the gas and liquid densities from (9.114) as function of the temperature-like parameter G. We do not present the thermodynamically consistent Maxwell-area reconstruction curve, as both curves would be indistinguishable in this figure.[10] We can see that phase separation occurs only for $G < -4$. The point at which the liquid and gas densities become equal ($G = -4$) is called *critical point*. For the equation of state in (9.111) with the pseudopotential in (9.102), the critical density is $\rho_{\text{crit}}/\rho_0 = \ln 2$. Figure 9.9 is widely used to initialise simulations consistently, i.e. by setting the initial density as ρ_{l} and ρ_{g} in the liquid and gas phases, respectively. For example, for $G = -6$ the initial densities are $\rho_{\text{g}} = 0.056$ and $\rho_{\text{l}} = 2.659$ with the associated liquid-gas density ratio 47.

For the original SC model with the equation of state $p = c_{\text{s}}^2\rho + c_{\text{s}}^2\Delta t^2 G\psi^2(\rho)/2$, simulations can be stable for G as low as ≈ -7. This defines the achievable liquid-gas density ratio around 60–80 and the maximum surface tension of 0.1 (in lattice units) [79]. To reach higher liquid-gas density ratios, one needs to revert to extensions as covered in Sect. 9.4.

Exercise 9.12 Derive the values of the critical parameters (G and ρ_{crit}). Use the fact that for a phase transition the first and second derivatives of the equation of state $p_{\text{b}}(\rho)$ with respect to density vanish at the critical point.

Finally, we can compute the SC liquid-gas surface tension at the planar interface and compare it with its thermodynamic consistent form. The surface tension for an

[10] Differences usually become visible at low densities when the density is plotted logarithmically.

assumed planar interface at $x = 0$ can be derived from (9.14). Using the pressure tensor in (9.112), we get

$$\gamma^{\mathrm{SC}} = \int_{-\infty}^{\infty} \left(P_{xx}^{\mathrm{SC}} - P_{yy}^{\mathrm{SC}} \right) \mathrm{d}x = -\frac{c_{\mathrm{s}}^4 G}{2} \int_{-\infty}^{\infty} \left(\frac{\mathrm{d}\psi}{\mathrm{d}x} \right)^2 \mathrm{d}x. \tag{9.115}$$

The **Shan-Chen surface tension** for the multiphase model is different from the thermodynamically consistent one. This reflects the difference between the SC and the thermodynamically consistent density profiles. However, the equilibrium bulk density values are often sufficiently similar for practical applications. Moreover, in reality the interface width is extremely thin (nanometres), and computational tools such as LBM are not able to resolve them properly. The diffuse interface method is just a way to describe multiphase physics numerically. Researchers are mainly interested in macroscopic parameters, such as the bulk densities and surface tension, rather than the exact shape of the interface between phases.

It is not feasible to express the pseudopotential gradient in (9.115) analytically and derive an expression for the surface tension. Instead, the Young-Laplace test yields the surface tension without evaluating the integral. We show the Young-Laplace results for the multiphase model in Sect. 9.3.2.5.

9.3.2.3 Boundary Conditions and Contact Angle

In the fluid domain, the velocity and pressure boundary conditions for the multiphase SC model are the same as for the standard LBM (cf. Chap. 5). In addition to pressure and velocity boundary conditions, we also have to consider multiphase effects near the boundary.

As pointed out in Sect. 9.1 and Sect. 9.2, fluid interfaces in contact with a solid boundary will assume a certain contact angle. The easiest way to include solid nodes with a given wetting behaviour is the introduction of a SC-like interaction force between solid nodes and boundary nodes (i.e. fluid nodes near solid nodes) as illustrated in Fig. 9.8:

$$\boldsymbol{F}^{\mathrm{SC,s}}(\boldsymbol{x}) = -G\psi(\boldsymbol{x}) \sum_{i}^{\mathrm{solid}} w_i \psi(\rho_{\mathrm{s}}) \boldsymbol{c}_i \Delta t. \tag{9.116}$$

This force acts on a fluid node at $\boldsymbol{x}$. The sum runs over all directions $\boldsymbol{c}_i$ for which $\boldsymbol{x} + \boldsymbol{c}_i \Delta t$ is a solid node. Solid nodes are assigned an effective density ρ_{s}. The contact angle at the solid boundary is indirectly controlled by the value of ρ_{s}.

The standard SC force in (9.105) continues to act between neighbouring fluid nodes. Therefore, we can write the total SC force at a fluid node at $\boldsymbol{x}$ as

$$\boldsymbol{F}^{\mathrm{SC}}(\boldsymbol{x}) = -G\psi(\boldsymbol{x})\left(\sum_{i}^{\text{fluid}} w_i\psi(\boldsymbol{x}+\boldsymbol{c}_i\Delta t)\boldsymbol{c}_i\Delta t + \sum_{i}^{\text{solid}} w_i\psi(\rho_{\mathrm{s}})\boldsymbol{c}_i\Delta t\right). \tag{9.117}$$

Solid and fluid nodes are treated on an equal footing; the only difference is that the density is prescribed at solid nodes. Therefore, the solid treatment is straightforward and easy to implement.

One needs to be attentive to avoid unnecessary condensation or evaporation near those boundaries. It is required to have densities consistent with the value for G from Fig. 9.9. For example, if the effective density is above the critical density ρ_{crit}, then the density in the fluid near this boundary will be driven towards the liquid density ρ_{l}, thus giving condensation (that may be undesired).

In order to achieve full wetting (contact angle 0°), we choose the bulk liquid density for the solid density: $\rho_{\mathrm{s}} = \rho_{\mathrm{l}}$. For a completely hydrophobic surface (contact angle 180°), we select $\rho_{\mathrm{s}} = \rho_{\mathrm{g}}$. All other contact angles can be realised by taking a solid density value between these two extremes.

For the free-energy model, the contact angle depends on the order parameter gradient (cf. (9.65)). A similar expression may be developed for SC involving the pseudopotential integrals [80]. However, it is difficult to apply in simulations due to its integral form.

9.3.2.4 Algorithm and Forcing Schemes

We briefly describe the relevant steps of the numerical algorithm for multiphase SC simulations. The choice of the forcing scheme is particularly important.

One should initialise the domain with gas and liquid densities obtained from (9.113) (or from Fig. 9.9) for a specific value of G. A common situation is a single liquid drop in vapour (or a single gas bubble in a liquid). It is recommended to implement an initially smooth interface. Starting with a density step change at the interface can cause instability for large liquid-gas density ratios. If the simulation involves solid boundaries with certain wetting properties, one may initialise a droplet as a spherical cap at a wall with a contact angle close to its expected value.

Another situation occurs if one is interested in phase separation, i.e. growth of liquid domains over time. To achieve his, the initial density is taken between ρ_{g} and ρ_{l}, and a small random fluctuation is imposed. For example, if the chosen average density of the system is $\bar{\rho}$, one could initialise the density with random values in the interval $\bar{\rho}(1 \pm 0.001)$, i.e. with a 0.1% perturbation. The tendency of the system to minimise its interface area will lead to an amplification of these perturbations and phase separation eventually.

In the following we will only consider the LBGK algorithm. For a short discussion of the MRT collision operator for multiphase and multicomponent models, see Sect. 9.4.

Each time step of the LB simulation after successful initialisation can be written as follows:

1. Find the fluid density $\rho = \sum_i f_i$ everywhere.
2. Calculate the SC force density $\boldsymbol{F}^{\mathrm{SC}}$ from (9.105). For fluid sites interacting with a solid wall, apply (9.116) to satisfy the wetting condition. If additional forces, such as gravity, act on the fluid, sum up all force contributions.
3. Compute the equilibrium distributions f_i^{eq} as usual. This involves the fluid velocity

$$\boldsymbol{u} = \frac{1}{\rho}\left(\sum_i f_i \boldsymbol{c}_i + \frac{\boldsymbol{F}\Delta t}{2}\right) \tag{9.118}$$

   where $\boldsymbol{F}$ includes all forces acting on the fluid. The velocity $\boldsymbol{u}$ is taken both as the equilibrium velocity $\boldsymbol{u}^{\mathrm{eq}}$ and as the physical velocity that solves the Navier-Stokes equation.
4. Use Guo's approach (cf. Sect. 6.3) to include the force in the collision step. See below for additional comments.
5. Collide and stream as usual. Hydrodynamic boundary conditions, such as bounce-back, are included in the normal way (cf. Chap. 5).
6. Go back to step 1.

In fact, the only novelty in this algorithm is the calculation of the SC force from the density; everything else is the standard LBM with forces. To the LB algorithm, the SC forces behave as every other external force.

Historically, the force density in the original SC works (and also in many more recent publications) was implemented *via* a modification of the equilibrium velocity without additional forcing terms in the LBE:

$$\boldsymbol{u}^{\mathrm{eq}} = \frac{1}{\rho}\left(\sum_i f_i \boldsymbol{c}_i + \tau \boldsymbol{F}\right). \tag{9.119}$$

Although this so-called Shan-Chen forcing approach, which is also discussed in Sect. 6.4, tends to be more stable, it leads to τ-dependent surface tension [81]. Therefore, we recommend to follow the algorithm as summarised above. See also [77] for a recent and careful discussion of forcing in the SC method.

Exercise 9.13 Perform the contact angle test similarly to that explained in Exercise 9.6. To control the contact angle in the SC model, vary the wall density ρ_{s} between ρ_{g} and ρ_{l}. In contrast to the free-energy model to which Exercise 9.6 applies, it is not possible to set the contact angle in the SC model directly. Measure the contact angle θ for different wall densities ρ_{s} and produce a diagram $\theta(\rho_{\mathrm{s}})$. As we cannot compare this curve with theoretical predictions in the SC model, we use the curve $\theta(\rho_{\mathrm{s}})$ as a constitutive law to find the appropriate wall density for a desired contact angle.

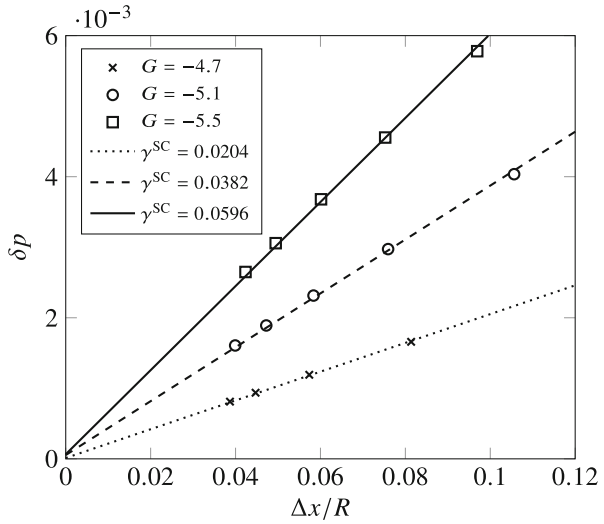

Fig. 9.10 Results of the Young-Laplace test for a liquid droplet in a gas phase. The pressure difference δp across the droplet interface is proportional to the inverse droplet radius R with the surface tension γ^{SC} as the proportionality factor. Simulations are shown for three different interaction parameters G. Pressure difference and surface tension are shown in lattice units. Simulations involve the standard SC model with the pseudopotential in (9.102) and Guo's forcing. The system size is $64\Delta x \times 64\Delta x$

9.3.2.5 Example: Young-Laplace Test

In Sect. 9.1.2 we have seen that in mechanical equilibrium the curved surface of a droplet leads to an increase of the interior pressure. For a 2D droplet, the pressure difference $\delta p = p_l - p_g$, the surface tension γ and the droplet radius R satisfy

$$\delta p = p_l - p_g = \frac{\gamma}{R}. \tag{9.120}$$

Instead of evaluating (9.115) to determine the SC surface tension γ^{SC}, we simulate a liquid droplet in the gas phase[11].

We define the droplet radius R as the radial position where the density profile reaches $(\rho_g + \rho_l)/2$. Due to the diffuse nature of the interface, other radius definitions are possible; this would lead to different interpretations of the surface tension. The pressure is computed from (9.111). We average the pressure over 4×4 grid nodes at the droplet centre and far away from the droplet surface, respectively.

It is common to simulate different droplet radii for fixed G to show that the measured pressure difference is indeed proportional to the inverse radius. The surface tension is then obtained from a linear fit. The results for different interaction parameters G are shown in Fig. 9.10. Note that the Young-Laplace test fails to work

[11] We could also simulate a gas bubble in a liquid.

in the limit of small radii (large $\Delta x/R$, not shown here). If the radius becomes comparable to the diffuse interface width, the droplet is not well-defined, and the pressure difference does not reach its expected value. This problem is more severe for smaller values of $|G|$ for which the interface width is larger.

9.3.3 Multicomponent Method Without Phase Change

In Sect. 9.3.2 we discussed how the SC model can be used to simulate a single-component multiphase system containing, e.g., liquid water and water vapour. In this section we discuss the SC model for miscible or immiscible mixtures of different fluids, e.g. oil and water. Although there are several similarities with the multiphase model, the simultaneous treatment of different fluids requires algorithmic extensions. We will first discuss these changes and then get back to the physics of multicomponent systems, followed by a revision of boundary conditions in the context of multicomponent fluids.

This section is mostly based on early works about the SC approach for multicomponent systems [68, 69, 71] with newer developments mentioned in passing. Shan [82] demonstrated how to derive this model from continuum kinetic theory. For recent review articles covering several extensions of the LBM for multicomponent flows we refer to [12, 13]. Also see Sect. 9.4 for a more detailed discussion of the limitations and extensions of the SC multicomponent method.

9.3.3.1 Shan-Chen Force and Algorithmic Implications

Let us take another look at the general SC interaction force for S components in (9.106). If we are only interested in the mixture of S ideal fluids, we can assume that each fluid component σ does not interact with itself. Therefore, the SC force only includes interactions between different fluid components, $\sigma \neq \tilde{\sigma}$:

$$\boldsymbol{F}^{\mathrm{SC}(\sigma)}(\boldsymbol{x}) = -\psi^{(\sigma)}(\boldsymbol{x}) \sum_{\tilde{\sigma}\neq\sigma} G_{\sigma\tilde{\sigma}} \sum_i w_i \psi^{(\tilde{\sigma})}(\boldsymbol{x} + \boldsymbol{c}_i \Delta t) \boldsymbol{c}_i \Delta t. \tag{9.121}$$

Here, $G_{\sigma\tilde{\sigma}} \equiv G_{\tilde{\sigma}\sigma}$ is the interaction strength of fluids σ and $\tilde{\sigma}$, and $\psi^{(\sigma)}$ is the pseudopotential of component σ, e.g. (9.102) or (9.103). Alternatively, we can allow the sum to run over all pairs, including $\tilde{\sigma} = \sigma$, and set $G_{\sigma\sigma} = 0$. In principle, there can be an arbitrary number of fluid components, but the SC model is mostly used for systems with two components ($S = 2$ as illustrated in Fig. 9.11). To achieve (partially) immiscible fluids, the interaction between components must be repulsive and hence the coupling strengths $G_{\sigma\tilde{\sigma}}$ positive. Different components can have different pseudopotentials.

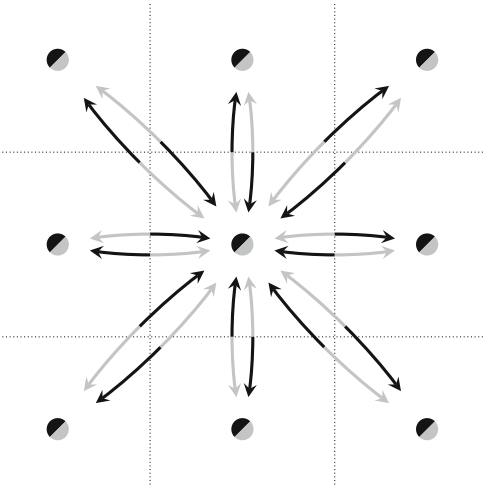

Fig. 9.11 Illustration of the interaction forces in a two-component system. At each lattice node, there exist two fluid components (*grey and black*). The black component interacts with the grey component at neighbouring cells and vice versa. These force pairs obey Newton's third law, illustrated by the *double-headed arrows*

In the multicomponent model, we need a set of populations $f_i^{(\sigma)}$ for each component σ. Each of these sets of populations obeys the standard LBGK equation

$$f_i^{(\sigma)}(\boldsymbol{x}+\boldsymbol{c}_i\Delta t, t+\Delta t) = f_i^{(\sigma)}(\boldsymbol{x},t) - \frac{f_i^{(\sigma)}(\boldsymbol{x},t) - f_i^{\mathrm{eq}(\sigma)}(\boldsymbol{x},t)}{\tau^{(\sigma)}}\Delta t + \left(1-\frac{\Delta t}{2\tau^{(\sigma)}}\right) F_i^{(\sigma)}(\boldsymbol{x},t)\Delta t \tag{9.122}$$

with its own relaxation time $\tau^{(\sigma)}$ (and therefore viscosity $\nu^{(\sigma)}$) and forcing terms $F_i^{(\sigma)}$ as defined below. We will briefly discuss the extension to the MRT collision operator in Sect. 9.4.

Now we have to discuss how to include the SC forces in the LBE and how to choose the equilibrium distributions when there is more than one LBGK equation.

9.3.3.2 Fluid Velocity in the Multicomponent Model

The most important change with respect to the single-component LBM involves the equilibrium distributions $f_i^{\mathrm{eq}(\sigma)}(\rho^{(\sigma)}, \boldsymbol{u}^{\mathrm{eq}(\sigma)})$. They are still given by (3.54) where the density ρ has to be replaced by the component density $\rho^{(\sigma)}$. However, it is not immediately clear which velocity $\boldsymbol{u}^{\mathrm{eq}(\sigma)}$ to use for the equilibrium distributions since we have more than one set of populations now.

We can define several velocities. The *bare component velocity* is given by

$$\boldsymbol{u}^{(\sigma)} = \frac{1}{\rho^{(\sigma)}}\sum_i f_i^{(\sigma)}\boldsymbol{c}_i, \quad \rho^{(\sigma)} = \sum_i f_i^{(\sigma)}. \tag{9.123}$$

The **barycentric velocity** of the fluid mixture reads [83]

$$\boldsymbol{u}_\mathrm{b} = \frac{1}{\rho}\sum_\sigma \left(\sum_i f_i^{(\sigma)} \boldsymbol{c}_i + \frac{\boldsymbol{F}^{\mathrm{SC}(\sigma)}\Delta t}{2} \right), \quad \rho = \sum_\sigma \rho^{(\sigma)}. \tag{9.124}$$

This velocity is force-corrected to achieve second-order time accuracy (cf. Sect. 6.3.2). It is also the physical velocity that has to be taken as the solution to the Navier-Stokes equation describing the fluid mixture [69].

Just as in the multiphase SC model in Sect. 9.3.2, there are essentially two different approaches for the multicomponent LB algorithm: Shan-Chen forcing and Guo forcing. The computation of the SC force density $\boldsymbol{F}^{\mathrm{SC}(\sigma)}$ itself is not affected by this choice. As this issue is generally not carefully addressed in the literature, we discuss it in more detail here.

Shan-Chen forcing: In the original works [68, 69, 71], the equilibrium velocity of component σ was chosen as

$$\boldsymbol{u}^{\mathrm{eq}(\sigma)} = \boldsymbol{u}' + \frac{\tau^{(\sigma)}\boldsymbol{F}^{\mathrm{SC}(\sigma)}}{\rho^{(\sigma)}} \tag{9.125}$$

with a *common velocity* $\boldsymbol{u}'$ that is given by the weighted average

$$\boldsymbol{u}' = \frac{\sum_\sigma \frac{\rho^{(\sigma)}\boldsymbol{u}^{(\sigma)}}{\tau^{(\sigma)}}}{\sum_\sigma \frac{\rho^{(\sigma)}}{\tau^{(\sigma)}}}. \tag{9.126}$$

This expression becomes particularly simple if all relaxation times are identical: $\boldsymbol{u}' = \sum_\sigma \rho^{(\sigma)}\boldsymbol{u}^{(\sigma)}/\rho$. The fluid components interact (i) through the SC force in (9.121) and (ii) by sharing the same velocity $\boldsymbol{u}'$ in (9.126).

Exercise 9.14 The common velocity $\boldsymbol{u}'$ has to assume the form in (9.126) to ensure momentum conservation during collision in the absence of forces [69]. Start from (9.122) and show that this is indeed the case.

If this so-called SC forcing approach is used, the additional forcing terms $F_i^{(\sigma)}$ in (9.122) have to be set to zero (see also Sect. 6.4). This forcing is easy to implement, in particular when all components have the same viscosity. In fact, most published works about SC-based multicomponent systems follow this approach.

The problem with the SC forcing is that it has been shown to lead to τ-dependent surface tension [81], which is clearly an unphysical effect.

Guo forcing: A forcing approach that leads to viscosity-independent surface tension is the extension of Guo's forcing to multiple components. Sega et al. [83] carefully derived the correct algorithm. The first ingredient is to use the barycentric

fluid velocity in (9.124) for *all* component equilibrium velocities:

$$\boldsymbol{u}^{\mathrm{eq}(\sigma)} = \boldsymbol{u}_{\mathrm{b}}. \tag{9.127}$$

Additionally, we have to specify the forcing terms $F_i^{(\sigma)}$ in (9.122). They are still given by (6.14), with the force replaced by the component SC force and the fluid velocity by the barycentric velocity [83]:

$$F_i^{(\sigma)} = w_i \left(\frac{c_{i\alpha}}{c_{\mathrm{s}}^2} + \frac{\left(c_{i\alpha} c_{i\beta} - c_{\mathrm{s}}^2 \delta_{\alpha\beta} \right) u_{\mathrm{b}\beta}}{c_{\mathrm{s}}^4} \right) F_\alpha^{\mathrm{SC}(\sigma)}. \tag{9.128}$$

Exercise 9.15 Show that (9.127) and (9.128) reduce to the standard Guo forcing presented in Sect. 6.3 if only a single fluid component exists ($S = 1$).

Shan-Chen and Guo forcing are equivalent to linear order in the force. Both methods differ by terms quadratic in $\boldsymbol{F}^{\mathrm{SC}(\sigma)}$. These terms are responsible for the τ-dependence of the surface tension of the SC forcing method.

9.3.3.3 Component Forces

So far we have considered systems that are only subjected to SC interaction forces. Each component σ feels the SC force $\boldsymbol{F}^{\mathrm{SC}(\sigma)}$ according to (9.121). Furthermore, there may be external forces $\boldsymbol{F}^{\mathrm{ext}}$ that act on all components, e.g. gravity. In this case, these forces are distributed to the components according to their concentration:

$$\boldsymbol{F}^{\mathrm{ext}(\sigma)} = \frac{\rho^{(\sigma)}}{\rho} \boldsymbol{F}^{\mathrm{ext}}, \quad \rho = \sum_\sigma \rho^{(\sigma)}. \tag{9.129}$$

The total force felt by component σ is then given by

$$\boldsymbol{F}^{(\sigma)} = \boldsymbol{F}^{\mathrm{SC}(\sigma)} + \boldsymbol{F}^{\mathrm{ext}(\sigma)}. \tag{9.130}$$

9.3.3.4 Immiscible and (Partially) Miscible Fluids, Surface Tension

To simplify the discussion, let us consider a system with two fluid components and interaction strength G_{12}. For $G_{12} = 0$, both fluids interact only through their common velocity $\boldsymbol{u}'$ (in case of SC forcing) or $\boldsymbol{u}_{\mathrm{b}}$ (in case of Guo forcing), but there is no interaction force and the system is an ideal fluid mixture and therefore completely miscible.

With increasing G_{12}, both components repel each other; above a critical value of G_{12}, both fluids finally separate and form an interface. The larger G_{12}, the thinner the interface region. This is shown in Fig. 9.12. If the repulsion was sufficiently

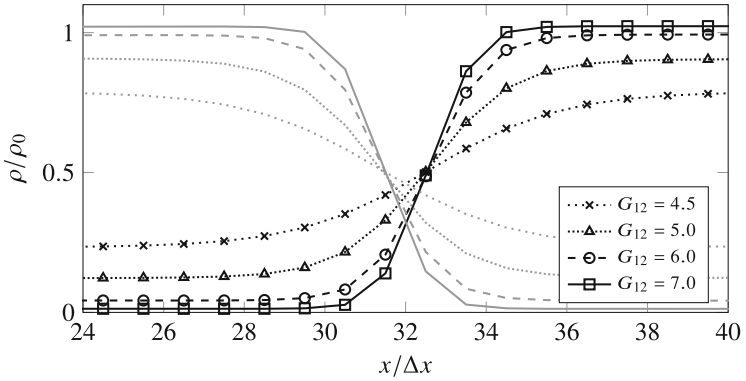

Fig. 9.12 Density profiles across the interface between two immiscible fluids. The interface is located at $x = 32\Delta x$. *Black curves* show the density of one component, *grey curves* the density of the other component. Symbols are only shown for the black lines to improve readability. Increasing G_{12} leads to a sharper interface and a more pronounced demixing of the components. No interface forms for values $G_{12} \approx 4$ or smaller. Although the total fluid density is not constant across the interface, the pressure according to (9.131) is constant up to finite difference approximation errors (both datasets not shown). Results have been obtained by using the pseudopotential in (9.102) and Guo's forcing

strong, the fluids would completely demix (completely immiscible). However, in reality there is always a small amount of fluid 1 in the domain of fluid 2 and the other way around (partially miscible). Particularly with diffuse interface methods, it is not possible to achieve completely immiscible fluids. In case of the SC model, the SC forces would become so large and numerically stiff at some point that component densities would become negative and the algorithm unstable [12].

In the miscible limit, where G_{12} is finite but sufficiently small, the system is characterised by mutual diffusion of the components. Shan and Doolen [69, 84] have thoroughly investigated the diffusion characteristics and the mixture viscosity in those systems. Miscible systems with a minority component, i.e. $\rho^{(\sigma)} \ll \rho^{(\tilde{\sigma})}$, can also be simulated with the methods presented in Chap. 8.

The SC model is particularly powerful when the components are immiscible. For sufficiently large G_{12}, when demixing occurs and interfaces between components appear, surface tension is an emergent feature of the SC model. Unfortunately, like in the multiphase model in Sect. 9.3.2, it is not clear *a priori* what the value of the surface tension γ is for a given choice of the interaction parameter G_{12}. We can pursue exactly the same strategy as in Sect. 9.3.2 and perform the Young-Laplace test to find the relation between G_{12} and γ for a given choice of pseudopotential. In order to undertake the Young-Laplace test, we need to know the pressure of the multicomponent fluid.

The **equation of state for the multicomponent SC model in the continuum limit** is [69]

$$p = c_s^2 \sum_{\sigma} \rho^{(\sigma)} + \frac{c_s^2 \Delta t^2}{2} \sum_{\sigma,\tilde{\sigma}} G_{\sigma\tilde{\sigma}} \psi^{(\sigma)} \psi^{(\tilde{\sigma})}. \tag{9.131}$$

The first term on the right-hand side reflects the ideal gas properties of the components while the second term denotes the interaction between them. It is this second term that can lead to phase separation of the components.

The Young-Laplace procedure is similar to that in Sect. 9.3.2. A droplet of one fluid is placed in the other fluid. Due to the surface tension and the curved droplet surface, the pressure from (9.131) in the droplet interior is larger then the exterior pressure. Measuring the pressure difference and the droplet radius allows us to obtain the surface tension in the usual way.

9.3.3.5 Boundary Conditions and Contact Angle

One of the most important applications of the multicomponent model is the simulation of flows in porous media where the flow behaviour is dominated by the interaction of the fluid components with the solid phase. These situations are commonly encountered in oil recovery and in the textile, pharmaceutical and food industries [13, 85, 86].

Like in the case of a multiphase fluid in Sect. 9.3.2, the interaction of a multicomponent fluid with a solid wall requires two main ingredients: (i) the no-slip condition and (ii) a wetting condition. The former is normally realised by the simple bounce-back method for all fluid components (cf. Sect. 5.3.3). For the latter we follow a similar approach as for a multiphase fluid in (9.116). In order to achieve the desired contact angle θ at the solid surface, different fluid components have to interact differently with the solid. The contact angle satisfies (9.9) where gas "g" and liquid "l" have to be replaced by fluid 1 and fluid 2.

Martys and Chen [71] proposed an interaction force between fluid and adjacent solid nodes:

$$\boldsymbol{F}^{s(\sigma)}(\boldsymbol{x}) = -G_{\sigma s} \rho^{(\sigma)}(\boldsymbol{x}) \sum_i w_i s(\boldsymbol{x} + \boldsymbol{c}_i \Delta t) \boldsymbol{c}_i \Delta t. \tag{9.132}$$

Here, $s(\boldsymbol{x})$ is an indicator function that assumes the values 0 and 1 for fluid and solid nodes, respectively, and $G_{\sigma s}$ is the interaction strength between fluid component σ and the solid boundary. For a wetting fluid, the interaction should be attractive and therefore $G_{\sigma s} < 0$ [87]. Accordingly, non-wetting fluids should have a positive value

of $G_{\sigma s}$. Taking a binary fluid with a given value of G_{12} as an example, the contact angle θ can be tuned by varying the two free parameters G_{1s} and G_{2s}.

We can find different fluid-surface force models in the literature, e.g. [12, 88, 89]. Chen et al. [12] proposed a form that is a direct extension of (9.116):

$$\boldsymbol{F}^{s(\sigma)}(\boldsymbol{x}) = -G_{\sigma s}\psi^{(\sigma)}(\boldsymbol{x})\sum_{i}^{\text{solid}} w_i \psi(\rho_s)\boldsymbol{c}_i \Delta t. \tag{9.133}$$

This model includes a "solid density" ρ_s as another degree of freedom. The solid density can be used to tweak the contact angle, see [88, 89] for example. If ρ_s is constant everywhere on the solid, it can be absorbed in the definition of $G_{\sigma s}$. In that case, and choosing $\psi^{(\sigma)} = \rho^{(\sigma)}$, (9.132) and (9.133) are equivalent.

Depending on the exact details of the chosen fluid-solid interaction model, it is generally necessary to run a series of simulations to establish the relation between the desired contact angle θ and the simulation parameters, i.e. G_{12}, G_{1s}, G_{2s} and ρ_s. Huang et al. [87] carefully investigated the behaviour of the contact angle in a binary system subject to the force in (9.132). They suggested a simple equation to predict the contact angle *a priori*. Their results indicate that the solid interaction parameters G_{1s} and G_{2s} should be similar in magnitude, $G_{1s} \approx -G_{2s}$, although it is in principle possible to choose different values.

To extract the contact angle from a simulation, we proceed in the same way as in Sect. 9.3.2. The only difference is that the number of free parameters controlling the wetting properties is larger in the multicomponent model.

9.4 Limitations and Extensions

All multiphase and multicomponent models are challenging to develop and usually show a number of limitations. We discuss the most common and most important limitations of the free-energy and Shan-Chen models and some remedies that have been suggested. These include spurious currents (cf. Sect. 9.4.1), restricted density ratio (cf. Sect. 9.4.2), limited surface tension range (cf. Sect. 9.4.3) and viscosity ratio restrictions (cf. Sect. 9.4.4). The section is concluded with a non-exhaustive list of extensions in Sect. 9.4.5, showing the breadth of applications that can be tackled with LB-based multiphase and multicomponent models. We treat the free energy and the Shan-Chen models side by side as their limitations are of a similar nature.

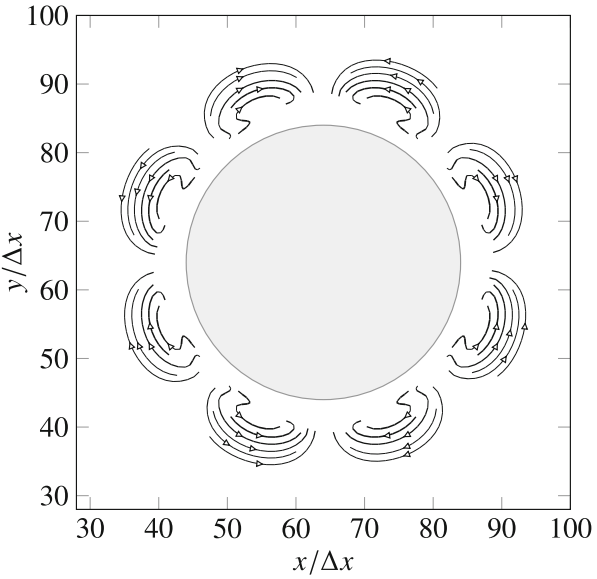

Fig. 9.13 Spurious currents appearing in the standard multiphase Shan-Chen model. A droplet with radius $20\Delta x$ is located at the centre of a 2D domain with size $128\Delta x \times 128\Delta x$. The interaction parameter is $G = -5.0$, and the relaxation time is $\tau = \Delta t$. The pseudopotential is $\psi = 1 - \exp(-\rho)$. Velocities with the magnitude less than $10^{-3}\Delta x/\Delta t$ are eliminated from the plot

9.4.1 Spurious Currents and Multirange Forces

When simulating a steady droplet, we expect zero fluid velocity everywhere. However, numerical simulations often reveal a different picture showing microcurrents (also *spurious* or *parasitic currents*) near the droplet interface. This is an unphysical and therefore undesirable effect. If the magnitude of the spurious currents is large, they can lead to numerical instability. Spurious currents are a well-known problem for LB and non-LB methods (see [11] and references therein). A recent review of spurious currents in LBM is available in [53].

Spurious currents appear both in the free-energy and the Shan-Chen models, both in multiphase and multicomponent applications [11]. Figure 9.13 shows the steady spurious currents near the surface of a droplet simulated with the Shan-Chen multiphase model. A similar profile for spurious currents is also observed for the free-energy model [51, 53].

Spurious currents are caused by numerical approximations of the surface tension force [12, 90]. For example, the surface tension force at the interface of a steady circular droplet should always point towards the centre of the droplet. If the numerical discretisation is not perfectly isotropic, we expect tangential force components that drive the spurious currents.

In many cases, the **characteristic flow** (e.g. due to droplet formation or phase separation) is significantly faster than the spurious currents. Those

(continued)

situations can usually be modelled well without taking additional care of the spurious currents. Simulations with large liquid-gas density ratios, however, usually require a special treatment of the spurious currents to avoid numerical instability.

It is also worth noting that all the strategies discussed in the following are analysed at equilibrium, with the key assumption that the spurious velocities are similarly reduced in transient simulations.

9.4.1.1 Shan-Chen Model

We can investigate the anisotropy of the Shan-Chen model analytically. Continuing the Taylor expansion in (9.107) to higher orders, we can write the Shan-Chen force on a D2Q9 lattice as a combination of dominating isotropic contributions and an anisotropic error term [74]:

$$\boldsymbol{F}^{\mathrm{SC}}(\boldsymbol{x}) = \underbrace{-G\psi(\boldsymbol{x})\left(\frac{1}{3}\nabla\psi(\boldsymbol{x}) + \frac{1}{18}\nabla\Delta\psi(\boldsymbol{x}) + \frac{1}{216}\nabla\Delta^2\psi(\boldsymbol{x})\right)}_{\text{isotropic}} + \boldsymbol{F}^{\mathrm{aniso}}. \tag{9.134}$$

The isotropic terms (up to fourth order) lead to radial forces, while the anisotropic term (fifth order),

$$\boldsymbol{F}^{\mathrm{aniso}} \propto G\psi(\boldsymbol{x})\left(\hat{\boldsymbol{e}}_x\partial_x^5 + \hat{\boldsymbol{e}}_y\partial_y^5\right)\psi(\boldsymbol{x}), \tag{9.135}$$

gives rise to a tangential force component and therefore the spurious currents in Fig. 9.13.

As the spurious currents are caused by the discretisation of the force, possible improvements could aim at the Shan-Chen force and its discretisation. One approach is to use a special mean-value approximation of the surface tension force [91]. Another solution is to improve the force isotropy. This approach is called *multirange* as it involves larger numerical stencils involving lattice nodes at greater distances (cf. Fig. 9.14).

The simplest multirange interaction force can be written with two interaction parameters G_1 and G_2 [74]:

$$\boldsymbol{F}^{\mathrm{SC}}(\boldsymbol{x}) = -\psi(\boldsymbol{x})\left[G_1\sum_{i\in\mathrm{b1}} w_i\psi(\boldsymbol{x}+\boldsymbol{c}_i\Delta t)\boldsymbol{c}_i\Delta t + G_2\sum_{i\in\mathrm{b2}} w_i\psi(\boldsymbol{x}+\boldsymbol{c}_i\Delta t)\boldsymbol{c}_i\Delta t\right] \tag{9.136}$$

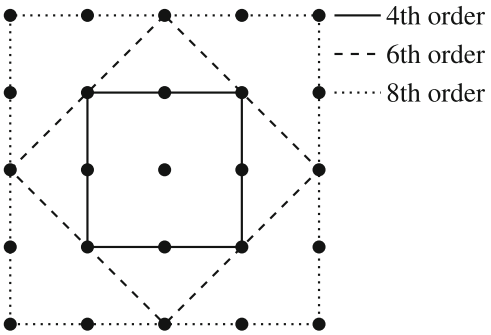

Fig. 9.14 Illustration of multirange stencils for a 2D Shan-Chen model. Increasing the range and therefore the number of interacting lattice nodes leads to an increasing isotropy order. The standard Shan-Chen model in (9.105) involves only the D2Q9 neighbours (4th order, *solid line*). The weights for the more isotropic numerical stencils are specified in [74]

where the first sum runs over belt 1 (b1, solid line in Fig. 9.14) and the second over belt 2 (b2, dotted line in Fig. 9.14). Including more and more belts of interacting lattice nodes decreases the magnitude of the spurious currents. We will come back to the multirange model in Sect. 9.4.3.

Despite its advantages, the multirange model is computationally more expensive. Also, boundary conditions need to be modified as there can now be several layers of solid nodes interacting with a fluid node. Apart from its primary function to increase isotropy, the multirange model has been employed to simulate emulsions with non-Newtonian rheology and non-coalescing droplets [92–94].

9.4.1.2 Free-Energy Model

Spurious currents appear in the free-energy model as well, and the root is the inexactness of discretised numerical stencils for approximating derivatives in the density or order parameter. Generally there are two common strategies which have been proposed to reduce spurious velocities in free-energy models. The first strategy, akin to the Shan-Chen model, is to improve the isotropy of the stencils for the derivatives [49–51], often at the expense of more computational time. Pooley and Furtado [51] showed that a good choice of stencil can lead to a reduction in spurious velocities by an order of magnitude.

As shown in Sect. 9.2, we have several choices to implement the non-ideal terms in the pressure tensor which account for the physics of surface tension. So the second strategy is to consider which form of the non-ideal terms can be discretised with least error. Numerical evidence shows that the forcing approach tends to perform better in comparison to the pressure tensor approach [51, 55]. For the forcing approach, we have seen that the non-ideal terms can be written either in the so-called *pressure* or *potential form*. While they are identical analytically,

their discretised forms are slightly different. The analysis by Jamet et al. [54] shows that the difference between the two forms is proportional to gradients of density, which are exacerbated at the interface. Using the potential form for implementing the non-ideal terms as a body force, and combining this with isotropic numerical derivatives for the density, Lee and Fischer [49] showed quite impressively that such a strategy can reduce the spurious velocities to essentially machine precision. One valid criticism on using the potential form is that momentum is no longer conserved exactly [95, 96].

9.4.2 Equation of State and Liquid-Gas Density Ratio

In some multiphase applications it is desirable to achieve large liquid-gas density ratios. Realistic density ratios seen in nature can be of the order of 10^3; this poses significant challenges for numerical stability. For example, the Shan-Chen multiphase model with its equation of state from (9.111) becomes unstable at $G \lesssim -7.0$ with a density ratio around 70 [79]. For the standard free-energy model, the situation is even worse because the surface tension force $k\rho\nabla\Delta\rho$ becomes unstable in the presence of large density differences, and the density ratio is limited to around 10. This instability is caused by the numerical stiffness of the forces.

The gas and liquid coexistence densites are determined by the equation of state through the Maxwell area construction rule (cf. Sect. 9.1.1). Thus, a key strategy to increasing the liquid-gas density ratio is by changing the equation of state. For the Shan-Chen model, the inclusion of an arbitrary equation of state requires redefinition of the pseudopotential function [78]. Starting from (9.111), we find

$$p_\mathrm{b}(\rho) = c_\mathrm{s}^2\rho + \frac{c_\mathrm{s}^2\Delta t^2 G}{2}\psi^2(\rho) \quad \Longrightarrow \quad \psi(\rho) = \sqrt{\frac{2}{c_\mathrm{s}^2\Delta t^2|G|}\left(p_\mathrm{b}(\rho) - c_\mathrm{s}^2\rho\right)}. \tag{9.137}$$

The interaction strength G effectively cancels when substituting the pseudopotential in (9.137) into the Shan-Chen force. One should especially make sure that the expression under the root remains always positive [12]. This is possible by adopting a special form of equilibrium functions [70].

In principle, any equation of state can be incorporated into the Shan-Chen model. However, it is usually suggested to use the Peng-Robinson or Carnahan-Starling equations of state because they can reach a density ratio up to 10^3 and the obtained densities have smaller deviations from their predicted values from the Maxwell area construction rule. The van der Waals equation of state usually yields a larger violation of thermodynamic consistency and is not generally recommended [78].

It is possible to make the Shan-Chen model thermodynamically consistent [97]. Such models, however, suffer from instability due to the discretisation of the term $k\rho\nabla\Delta\rho$. This term is potentially unstable when the liquid-gas density ratio (and therefore the density gradients) are large.

Recently, Lycett-Brown and Luo [77] showed that the liquid-gas coexistence behaviour of the Shan-Chen model can be significantly improved when additional forcing terms are considered. They performed a Chapman-Enskog analysis up to third order in the force and derived correction terms that remove or improve a number of shortcomings of the Shan-Chen model (see also Sect. 9.4.3).

For the free-energy model, different equations of state are easily integrated by modifying the equilibrium functions (cf. (9.36)) or by including the non-ideal terms as forcing terms (cf. (9.43) and (9.44)). Only changing the equation of state, however, is inadequate to reach density ratios of the order of 10^3.

To improve the stability of multiphase free-energy models, several successful approaches have been developed which share a common thread: they exploit two distribution functions. Inamuro et al. [98] used one distribution for the density and another distribution for the predicted velocity without pressure gradient. Every LB step is then followed by a pressure correction step which is relatively expensive computationally. Lee and Lin [44] also used two distribution functions to track the density and pressure, respectively. Lee and Lin's method does not require a pressure correction step. However, its implementation is quite complex as it requires discretisations of many first- and second-order derivatives, as well as different representations of the surface tension force. Zheng et al. [99] developed a scheme which is effectively a "hybrid" between the multiphase and multicomponent model. In their scheme, one distribution function is assigned to the density field and for solving the hydrodynamic equations of motion. The other distribution belongs to an order parameter for tracking the liquid-gas interface. In contrast to Sect. 9.2.2 for the standard binary model where the density is required to be a constant, the fluid density is allowed to vary between the phases in Zheng et al.'s method.

More recently, Karlin and co-workers [45, 100] developed an entropic LB scheme for multiphase flow and achieved large density ratios without the need to implement a pressure correction or an additional set of distribution functions. In entropic LBM, entropy balance is approximated in the relaxation step at each node, which helps stabilise the liquid-gas interface.

Multiphase flows are often characterised by **low capillary and low Reynolds numbers**. One example is Bretherton flow of long bubbles or fingers in a microchannel. In this case the liquid-gas density ratio is not the governing non-dimensional number. As a consequence, the **exact density ratio does not have to be matched** and a simple multiphase or a multicomponent model can be employed. In many situations, it is actually possible to **replace a multiphase model by a multicomponent model with much lower liquid-gas density ratio** [101, 102], thus avoiding numerical instability and undesirable condensation/evaporation.

9.4.3 Restrictions on the Surface Tension

In practical applications, the numerically accessible range of the surface tension is limited. Large surface tensions can lead to instability, and this issue often goes hand-in-hand with spurious velocities discussed in Sect. 9.4.1. The magnitude of the spurious velocities typically increases with the surface tension.

For standard multiphase and multicomponent free-energy models, the highest achievable surface tension is no more than 0.1 (lattice units). The standard Shan-Chen model also has a similar limitation; a surface tension of ~ 0.1 is achievable for $G \approx -7$ beyond which simulations become unstable.

In interface-governed flows, the important dimensionless parameters include the capillary number $\mathrm{Ca} = \eta u/\gamma$ (u is a characteristic velocity) and the Bond number $\mathrm{Bo} = \rho g \ell_\mathrm{S}^2/\gamma$ (g is the gravitational acceleration and ℓ_S is a characteristic length scale, e.g. the system size). While the numerical range of the surface tension in LBM is limited, the relevant dimensionless numbers can, to some extent, be varied by changing the other parameters (cf. Sect. 7.3.5).

In the context of surface tension, an advantage of free-energy models is that the equation of state, the surface tension, and the interface width can all be varied independently. This is not the case for the *original* Shan-Chen model where the parameter G determines both the equation of state in (9.111) and the surface tension force $\propto G\psi(\rho)\nabla\Delta\psi(\rho)$. As such, low values of the surface tension are often linked to a large interface width and loss of immiscibility (in case of multicomponent fluids).

To decouple the equation of the state from the surface tension, the Shan-Chen multirange approach from Sect. 9.4.1 can be used. Starting from (9.136) and a Taylor expansion as in Sect. 9.3.2, one can show that the equation of state and the surface tension change to [103]

$$\begin{aligned} p_\mathrm{b}(\rho) &= c_\mathrm{s}^2\rho + \frac{c_\mathrm{s}^2\Delta t^2 A_1}{2}\psi^2(\rho), \\ \gamma &= -\frac{c_\mathrm{s}^4 A_2}{2}\int\left(\frac{\mathrm{d}\psi}{\mathrm{d}x}\right)^2 \mathrm{d}x \end{aligned} \tag{9.138}$$

with $A_1 = G_1 + 2G_2$ and $A_2 = G_1 + 8G_2$. By changing G_1 and G_2 accordingly, the equation of state and surface tension can be modified independently.

Exercise 9.16 Show the validity of (9.138), following the derivation outlined in the previous paragraph.

Recent progress in understanding the role of the Shan-Chen force makes it possible to change the equation of state (and therefore the liquid-gas density ratio), surface tension and interface width independently and over a wider range than previously possible [77].

9.4.4 Viscosity Ratio and Collision Operator

Multicomponent problems often involve fluids with different kinematic viscosities (or densities). Miscible multicomponent fluids are characterised by their Schmidt number (ratio of mass and momentum diffusivity). Modelling these systems can be challenging [104]. The original Shan-Chen model, for example, is limited to a viscosity ratio of about 5 [105]. For mixtures with density ratios other than unity, section 6 in the review [12] contains an overview of recent progress in the field.

Due to the well-known restrictions of the BGK collision operator, it is generally recommended to use MRT for fluid mixtures with large viscosity ratio. Porter et al. [104] achieved a kinematic viscosity ratio of up to 1000 in the Shan-Chen model by using MRT and enhanced force isotropy. MRT also helps to reach higher Reynolds numbers in bubble simulations [106]. While the BGK operator leads to a fixed Schmidt number, the MRT collision operator can be employed to change mass and momentum diffusivity independently [107]. Other works involving the MRT collision operator (both for multicomponent and multiphase, and free energy and Shan-Chen) include [81, 108–111].

It is worth mentioning that Zu and He [112] suggested a multi*component* model with density ratio; a feature that is usually neglected in other works.

9.4.5 What Else Can Be Done with These Models?

In this chapter we have deliberately focussed on two-phase and two-component flows, both using the free-energy and the Shan-Chen approaches. The ideas developed here can be extended in many different directions, and these are areas of current active research. We will now highlight some examples, inevitably selective, of interesting problems.

The simplest extension to models described here is to introduce *more fluid components*, and in recent years particularly ternary systems [6, 43, 113, 114] have attracted growing interest. In fact, we are not limited to "normal" fluids. It is also possible to extend the model to include *surfactants* [115, 116]. Surfactants are amphiphilic molecules; one end of the molecule is hydrophilic (likes water; dislikes oil), the other hydrophobic (dislikes water; likes oil). Thus, surfactants tend to sit at the interface between water and oil, and they tend to reduce the water-oil surface tension. Surfactants are foundational for many industries, from oil recovery to food and consumer products.

The complexity of fluid dynamical problems is tightly related to the *boundary conditions*. There is a large literature base covering systems with, e.g., free surfaces [117–119], droplet spreading on solid surfaces [120, 121] and Leidenfrost droplets [122]. The LBM is excellent for handling tortuous boundary conditions, such as for flow in porous materials [123, 124]. The wetting boundary conditions can also be

extended to cases where the solid surfaces are mobile, thus allowing the simulation of colloidal particles and polymers at fluid-fluid interfaces [83, 89, 125–128].

Many investigations only focus on steady droplets for which conditions at the domain boundaries do not play an important role. Contrarily, despite some progress [129], *open boundary conditions* for multiphase flows have not yet been thoroughly investigated. Those conditions are important for problems such as droplet formation and manipulation in microfluidic channels [130, 131]. Pressure boundary conditions pose a particular challenge as they have to be combined with the modified pressure due to the non-ideal equation of state. In simulations this can manifest as unexpected condensation or evaporation.

Throughout this chapter we have mostly neglected *phase change*. LB models have been successfully applied to systems with evaporation [132, 133], solidification [134, 135] and even chemical reactions, e.g. at liquid interfaces [136].

The free-energy approach is particularly popular in the physics community. Different choices for the free energy can allow for *new physics*, and there is a wide range of problems in complex fluids where hydrodynamics is important. Including curvature energy into the gradient terms allow the study of lamellar phases [137] and vesicles [138, 139]. The bulk free energy can be modified as well to add more complex equations of state, e.g. for liquid crystals [140]. The descriptions of these physical phenomena enter the Navier-Stokes equation through the pressure tensor, which in turn can be implemented in the LBE through the equilibrium distribution functions or forcing terms.

9.5 Showcases

We discuss two common multiphase/multicomponent applications and explain how to simulate them using LB simulations: droplet collisions in Sect. 9.5.1 and wetting on structured surfaces in Sect. 9.5.2. Both applications are of great relevance for today's engineering challenges, such as inkjet printing and functional surfaces.

9.5.1 Droplet Collisions

One important application of multiphase LBM is the collision of droplets, in particular in an ambient gas phase. This phenomenon occurs in nature, e.g. cloud formation, and in many industrial areas, such as ink-jet printing and spray combustion in internal combustion engines. A better understanding of droplet collision helps improving these industrial processes. For example, the coalescence of droplets impinging on paper affects the quality of ink-jet printing. There are many experimental works

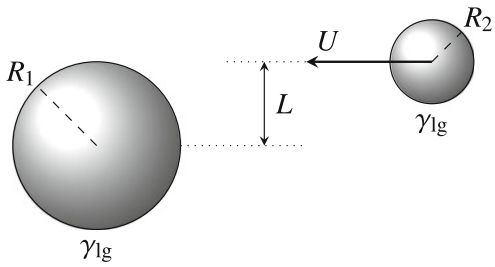

Fig. 9.15 Sketch of two colliding droplets with radii R_1 and R_2. This collision is shown in the rest frame of the larger droplet, having the smaller droplet approaching with velocity U. Collisions usually happen with a finite off-centre distance L

studying droplet collisions [141, 142]. It was found that this phenomenon exhibits a rich map of collision modes as detailed below.

Collisions of two droplets are characterised by a number of physical parameters, such as the droplet radii R_1 and R_2, impact velocity U, off-centre distance L, density ρ and viscosity η of both the liquid droplets (denoted by "l") and the surrounding gas (denoted by "g"), and surface tension γ (cf. Fig. 9.15). From those physical parameters we can construct relevant non-dimensional groups [141, 143]:

$$\begin{aligned}
\mathrm{We} &= \frac{U^2(m_1+m_2)}{4\pi\gamma\left(R_1^2+R_2^2\right)}, && \text{(symmetric Weber number)}\\
\mathrm{Re} &= \frac{\rho_\mathrm{l} U(R_1+R_2)}{\eta_\mathrm{l}}, && \text{(Reynolds number)}\\
\mathrm{B} &= \frac{L}{R_1+R_2}, && \text{(impact factor)}\\
&\frac{R_1}{R_2}, \frac{\eta_\mathrm{l}}{\eta_\mathrm{g}}, \frac{\rho_\mathrm{l}}{\rho_\mathrm{g}}. && \text{(radius, density and viscosity ratios)}
\end{aligned} \tag{9.139}$$

Many works concentrate on droplets with equal sizes ($R_1 = R_2 = R$). Thus, the Weber and Reynolds numbers simplify to $\mathrm{We} = \rho_\mathrm{l} R U^2/(3\gamma)$ and $\mathrm{Re} = 2\rho_\mathrm{l} R U/\eta_\mathrm{l}$, respectively.

Depending on the value of the collision parameters, different regimes can be identified [141, 144]. Figure 9.16 shows a droplet collision map obtained from a large number of experiments. This map can be explained by considering the roles of surface tension and inertia, and by using the illustrations in Fig. 9.17.

1. **Coalescence after minor deformation.** If the kinetic energy is small, the gas between droplets is able to drain and the droplet deformation is small. Thus, the gas film does not lead to a strong repulsion between the droplets. When the droplets are close enough, coalescence happens through the van der Waals force.
2. **Bouncing.** Increasing the kinetic energy (higher Weber number), the gas between the droplets is not able to drain in time. A high pressure builds up between the droplets, and the kinetic energy is temporarily stored in the deformed surfaces. The droplets are pushed back and bounce before coalescence can occur.

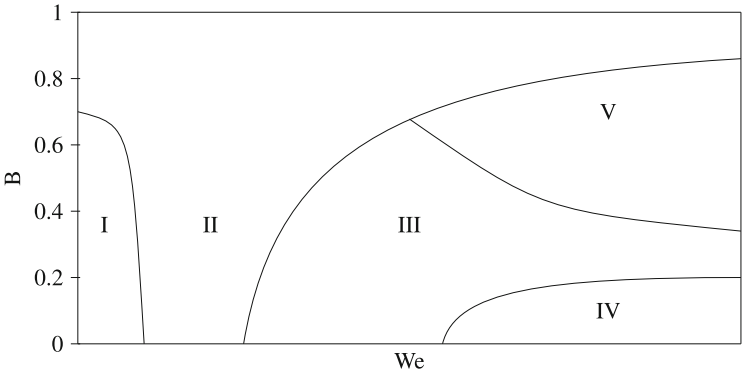

Fig. 9.16 Collision map for droplets of equal size. Depending on the Weber number and the impact parameter B, the following regimes can be found: (I) coalescence after minor deformation, (II) bouncing, (III) coalescence after substantial deformation, (IV) reflective separation and (V) stretching separation. See the text for more explanation and Fig. 9.17 for illustrations

3. **Coalescence after substantial deformation.** With further increase of the kinetic energy, the droplets are substantially deformed. The pressure at the centre of the film between the droplets is higher than at the outer film region, and it pushes gas out of the gap. After the gas in the film has sufficiently drained, the droplets coalesce. At the initial stage of coalescence, the newly formed droplet has a torus-like shape. Surface tension drives the droplet towards a spherical shape. This leads to droplet oscillations that are eventually damped by viscous dissipation.
4. **Reflexive separation.** For even higher Weber number, the droplet oscillation is not efficiently damped. Due to the large kinetic energy in the system, two liquid pockets form at opposite ends that drive the droplet apart along the original collision axis. Surface tension is too weak to balance the inertial force, and the droplet breaks up into two smaller droplets. Sometimes more droplets are formed as the filament between the droplets becomes unstable and breaks up into several satellite droplets.
5. **Stretching separation.** If the impact parameter B is large, droplet separation can happen without oscillations as significant parts of the droplets do not interact with each other. Instead, these droplet parts continue moving in their original directions. While moving, a filament forms between the droplets. Depending on the droplet parameters, the filament can either stabilise or disintegrate by forming small satellite droplets.

The collision map in Fig. 9.16 does not include the viscosity and density ratios; in fact, these parameters also have a strong effect on the collision outcome. For example, there is no bouncing regime for water droplets colliding in air, but bouncing exists for hydrocarbon droplets in air [141]. For more detailed parameter studies we refer to experimental works [141–143] and numerical studies [144–146].

To conclude this section, we now focus on the role of LBM in droplet collisions. Numerical studies allow us to obtain important information that is difficult to

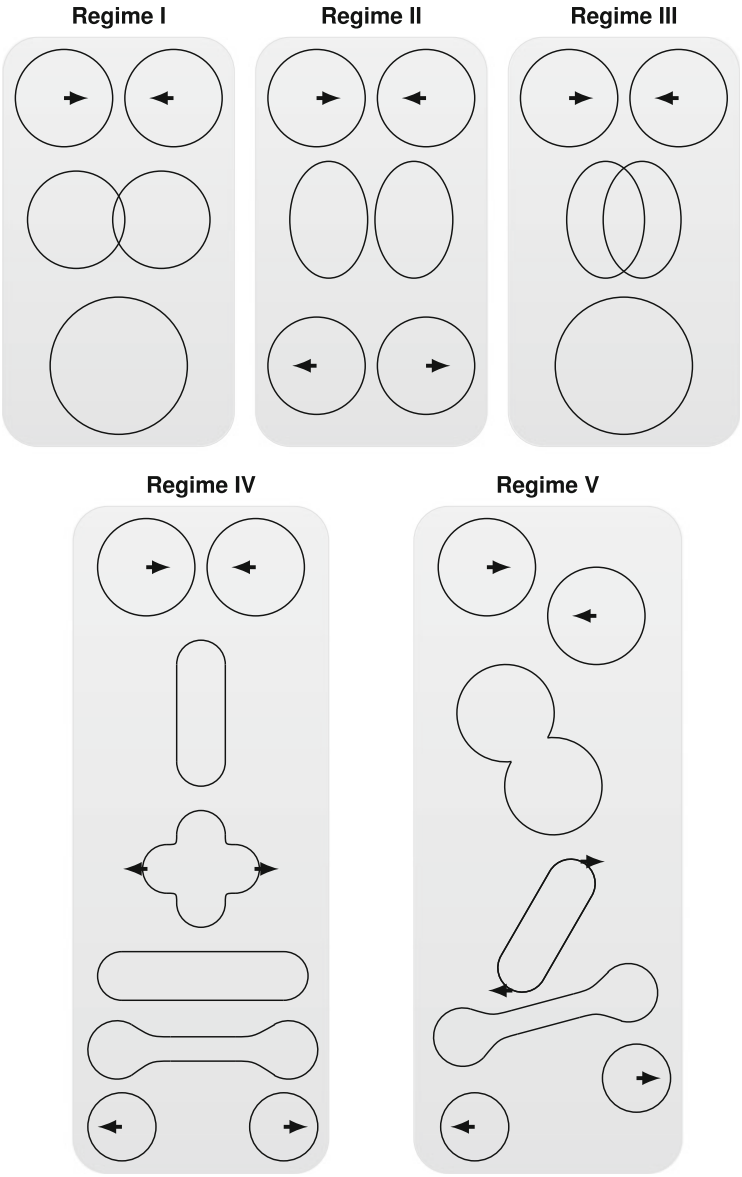

Fig. 9.17 Droplet collision regimes and mechanisms. See Fig. 9.16 for more details

observe experimentally, e.g. mixing of the liquids during droplet collisions. Also, it is possible to study the influence of viscosity and density ratios which are usually neglected in experimental works. However, there are several challenges that LB users need to consider in order to perform successful droplet collision simulations:

- To realise the droplets' *collision velocity*, body forces based on the density difference between phases acting on the liquid regions are often employed [147].
- The *liquid-gas density ratio* in experiments is around 500–1000 (e.g. oil or water droplets in air). To reach such density ratios in simulations, special equations of state are usually employed (cf. Sect. 9.4), such as Peng-Robinson [146] or Carnahan-Sterling [144].
- Real-world *Weber numbers* are usually between ~ 0 and 100. It is hard to achieve large values in simulations due to intrinsic velocity and liquid density limitations. Usually, one needs to reduce the surface tension accordingly, cf. (9.139).
- Diffuse interface methods often lead to problems with droplet coalescence. If the droplets are close enough, they "feel" each other due to their diffuse interface shapes. This can lead to *premature coalescence*. Physical coalescence happens within the range of the van der Waals force, i.e. 10 nm and therefore orders of magnitude smaller than the interface thickness in simulations. This issue has been examined carefully in the context of droplet collisions and the conditions for coalescence in liquid-liquid systems through high-resolution simulations having droplet radii up to 200 lattice nodes [148, 149]. It has been suggested that premature coalescence is one of the possible reasons for the difficulty of simulating the bouncing regime [144]. Another resolution problem manifests in the dissolution of thin liquid filaments, such as the lamina between droplets. This can lead to premature droplet breakup [146].

Overall, droplet collision is an interesting phenomenon with a rich parameter space. It is a suitable benchmark for multiphase models. Limitations caused by the diffuse interface method are challenging and often lead to deviations between experimental and numerical results. More research is still required.

9.5.2 Wetting on Structured Surfaces

One of the primary advantages of the LBM is its ability to handle complex boundary conditions. This advantage remains for multiphase and multicomponent flows. Variation in the surface wettability can be implemented easily by applying different values of the phenomenological parameter h in (9.64) and (9.83) for the free-energy multiphase and multicomponent models, or by varying the solid density ρ_s and the solid-fluid interaction parameters $G_{\sigma s}$ for the Shan-Chen models at different surface lattice sites.

Here we will highlight how LBM can be used to model drops spreading on chemically and topographically patterned surfaces. There are two complementary

perspectives why such modelling is of great scientific interest. First, any real surface is never perfectly smooth and chemically homogeneous; indeed, surface heterogeneities are an important consideration in many areas, including oil recovery, fluid filtration and capillary action in plants [150, 151]. Secondly, it is becoming increasingly feasible to fabricate surfaces with roughness and heterogeneities in a controlled and reproducible manner. Thus, instead of being viewed as a problem, surface patterning has now become a versatile part of a designer toolbox to control the shapes and dynamics of liquid droplets and interfacial flows [152, 153].

9.5.2.1 Chemical Patterning

We first look at a drop spreading on a chemically patterned surface. For a homogeneous surface, the droplet's final state is a spherical cap with a contact angle equalling the Young angle, as illustrated in Exercise 9.6. This is not the case for heterogeneous surfaces, however.

Figure 9.18 shows simulation results of drops on a chemically patterned substrate. The surface is lined with hydrophilic and hydrophobic stripes with Young angles of 45° and 105° and widths of $8\Delta x$ and $24\Delta x$, respectively. The drop volumes have been chosen so that their final diameters were comparable to the stripe width.

Simulations and experiments show that the final drop shape is selected by the initial impact position and velocity. If the drop can touch two neighbouring hydrophilic stripes as it spreads, it will reach the "butterfly" configuration, Fig. 9.18a. Otherwise, it will retract back to the "diamond" pattern, spanning a single stripe, Fig. 9.18b. Both states are free energy minima but one of the two is a metastable minimum: which one is metastable depends on the exact choice of the physical parameters. For more detailed discussion we refer the readers to dedicated articles on this topic [32, 154, 155].

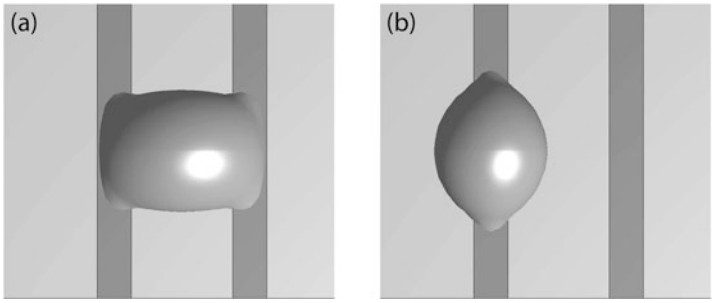

Fig. 9.18 Drops spreading on chemically striped surfaces. Hydrophilic (45°) and hydrophobic (105°) stripes are shown in *dark and light grey*, respectively. The drop shapes depend on the initial impact position and velocity, either spanning across (**a**) two or (**b**) one hydrophilic stripes

More complex chemical heterogeneities can be modelled in LB simulations. Such strategies have been proposed, for example, to control drop position in inkjet printing [156] or to control flow in open microfluidic platforms [157].

9.5.2.2 Topographical Patterning: Superhydrophobic Surfaces

In addition to chemical heterogeneities, surface roughness is important for determining the wetting properties of a solid surface. A prime example is the so-called *superhydrophobic* surface [158]. On a smooth hydrophobic surface, the highest contact angle that can be achieved is of the order of 120°, which is attainable for fluorinated solids (e.g. teflon). When the hydrophobic surface is made rough, however, higher contact angles are possible. The most famous example of a superhydrophobic surface is the lotus leaf (superhydrophobicity is often called the *lotus effect*) [159], but many other natural materials, such as butterfly wings, water strider legs, and duck feathers also exhibit this property. We are also now able to fabricate synthetic superhydrophobic surfaces [160, 161].

It is possible to distinguish two ways in which a drop can behave on a rough surface. One possibility is for the drop to be suspended on top of the surface roughness, as shown in Fig. 9.19a. The droplet effectively sees a composite of liquid-solid and liquid-gas areas. We use Φ to denote the area fraction of the liquid-solid contact (and hence $1 - \Phi$ is the area fraction of the liquid-gas contact). If the length scale of the patterning is much smaller than the drop size, the effective liquid-solid surface tension is the weighted average $\Phi\,\gamma_{\mathrm{sl}} + (1 - \Phi)\,\gamma_{\mathrm{lg}}$. The gas-solid surface tension is $\Phi\,\gamma_{\mathrm{sg}}$. Substituting these into Young's equation, (9.9), gives us the *Cassie-Baxter formula* [162]

$$\cos\theta_{\mathrm{CB}} = \Phi\cos\theta - (1 - \Phi) \tag{9.140}$$

where θ is the contact angle if the surface was smooth, and θ_{CB} is the effective contact angle. This equation provides an important insight: the presence of the second term means $\theta_{\mathrm{CB}} > \theta$. When the droplet is suspended on top of what is

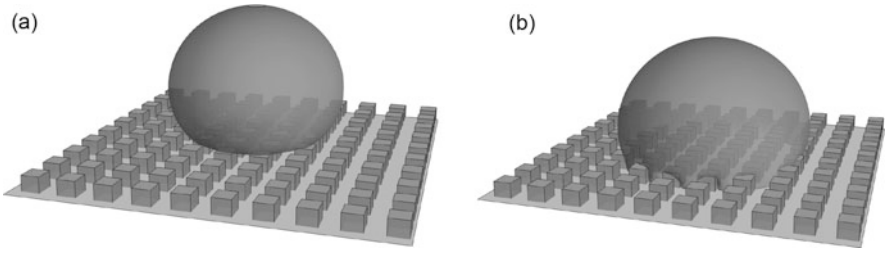

Fig. 9.19 Final states of drops spreading on topographically patterned surfaces. The material (if the surface was smooth) contact angle is 120° and 80° for panels (**a**) and (**b**) respectively. In (**a**) the drop is suspended on top of the corrugations, while it penetrates the posts in (**b**)

effectively an air mattress, it slides very easily across the surface. The drag reduction property of superhydrophobic surfaces is also highly superior. Slip lengths as high as several microns have been reported [163].

The suspended state is not always stable. For example, as we lower the material's contact angle, the liquid usually penetrates the corrugation and fills the space in between the posts, as shown in Fig. 9.19b. In such a case, both the liquid-solid and gas-solid contact areas are increased by a roughness factor r, which is the ratio of total area of the textured surface to its projected area. The effective contact angle θ_W is therefore given by the *Wenzel equation* [164]

$$\cos\theta_W = r\cos\theta. \tag{9.141}$$

This equation suggests that a hydrophilic surface will appear more hydrophilic in the presence of roughness, and similarly a hydrophobic surface will appear more hydrophobic. Compared to the case where the liquid is suspended, fluid drag is strongly increased when liquid penetrates the corrugation. In this collapsed state, the fluid interface is also strongly pinned by the surface corrugations.

Let us end this section by discussing typical considerations for simulating wetting on structured surfaces using LBM:

- It is important to get the hierarchy of length scales correctly. Both for chemically and topographically patterned surfaces, we have (i) the interface width, (ii) the pattern size, and (iii) the drop radius. Ideally we want to make sure that drop radius $\gg$ pattern size $\gg$ interface width, which can be demanding computationally. In practice, a separation of length scales by an order of magnitude is adequate.
- There is, in fact, a fourth length scale corresponding to mechanisms for which the contact line can move. In diffuse interface models, the contact line moves due to an evaporation-condensation mechanism for the multiphase model [41, 165], and due to a diffusive mechanism for the multicomponent model [42, 88]. We refer the readers to [66] for a detailed analysis on the effect of varying the contact line slip length against the interface width.
- Similar to the previous subsection, capturing realistic density ratios of 500–1000 can be critical for the accuracy of the simulations, and it is therefore desirable. However, depending on the applications, we can often get away with much smaller density ratios, for example when we are only interested in equilibrium/final configurations, or when the inertial terms in the Navier-Stokes equation are irrelevant for the problem at hand. For the latter, usually getting the viscosity ratio right is more important.

References

1. A.K. Gunstensen, D.H. Rothman, S. Zaleski, G. Zanetti, Phys. Rev. A **43**(8), 4320 (1991)
2. D. Grunau, S. Chen, K. Eggert, Phys. Fluids A **5**(10), 2557 (1993)

3. M.M. Dupin, I. Halliday, C.M. Care, J. Phys. A: Math. Gen. **36**(31), 8517 (2003)
4. M. Latva-Kokko, D.H. Rothman, Phys. Rev. E **71**(5), 056702 (2005)
5. H. Liu, A.J. Valocchi, Q. Kang, Phys. Rev. E **85**(4), 046309 (2012)
6. S. Leclaire, M. Reggio, J.Y. Trépanier, J. Comput. Phys. **246**, 318 (2013)
7. P. Asinari, Phys. Rev. E **73**(5), 056705 (2006)
8. S. Arcidiacono, I.V. Karlin, J. Mantzaras, C.E. Frouzakis, Phys. Rev. E **76**(4), 046703 (2007)
9. T.J. Spencer, I. Halliday, Phys. Rev. E **88**(6), 063305 (2013)
10. J. Tölke, G.D. Prisco, Y. Mu, Comput. Math. Appl. **65**(6), 864 (2013)
11. L. Scarbolo, D. Molin, P. Perlekar, M. Sbragaglia, A. Soldati, F. Toschi, J. Comput. Phys. **234**, 263 (2013)
12. L. Chen, Q. Kang, Y. Mu, Y.L. He, W.Q. Tao, Int. J. Heat Mass Transfer **76**, 210 (2014)
13. H. Liu, Q. Kang, C.R. Leonardi, S. Schmieschek, A. Narváez, B.D. Jones, J.R. Williams, A.J. Valocchi, J. Harting, Comput. Geosci. pp. 1–29 (2015)
14. H. Huang, M.C. Sukop, X.Y. Lu, *Multiphase Lattice Boltzmann Methods: Theory and Applications* (Wiley-Blackwell, Hoboken, 2015)
15. C.E. Brennen, *Fundamentals of Multiphase Flows* (Cambridge University Press, Cambridge, 2005)
16. J. Bibette, F.L. Calderon, P. Poulin, Reports Progress Phys. **62**(6), 969 (1999)
17. M.J. Blunt, Current Opinion Colloid Interface Sci. **6**(3), 197 (2001)
18. A. Faghri, Y. Zhang, *Transport Phenomena in Multiphase Systems* (Elsevier, Amsterdam, 2006)
19. C.D. Han, *Multiphase Flow in Polymer Processing* (Academic Press, New York, 1981)
20. A. Gunther, K.F. Jensen, Lab Chip **6**, 1487 (2006)
21. C. Wang, P. Cheng, Int. J. Heat Mass Transfer **39**(17), 3607 (1996)
22. S. Blundell, K.M. Blundell, *Concepts in Thermal Physics* (Oxford University Press, Oxford, 2006)
23. M. Doi, T. Ohta, J. Chem. Phys. **95**(2), 1242 (1991)
24. T.G. Mason, Current Opinion Colloid Interface Sci. **4**(3), 231 (1999)
25. R. Osserman, *A Survey of Minimal Surfaces* (Dover Publications, New York, 1986)
26. L.D. Landau, E.M. Lifshitz, *Fluid Mechanics* (Pergamon Press, Oxford, 1987)
27. P.G. de Gennes, F. Brochard-Wyart, D. Quéré, *Capillarity and Wetting Phenomena: Drops, Bubbles, Pearls, Waves* (Springer, New York, 2004)
28. J.S. Rowlinson, B. Widom, *Molecular Theory of Capillarity* (Oxford University Press, Oxford, 1989)
29. J.L. Barrat, L. Bocquet, Phys. Rev. Lett. **82**, 4671 (1999)
30. D.M. Huang, C. Sendner, D. Horinek, R.R. Netz, L. Bocquet, Phys. Rev. Lett. **101**, 226101 (2008)
31. A. Lafuma, Quéré, Nat. Mat. **2**, 457–460 (2003)
32. J. Léopoldés, A. Dupuis, D.G. Bucknall, J.M. Yeomans, Langmuir **19**(23), 9818 (2003)
33. Z. Wang, J. Yang, B. Koo, F. Stern, Int. J. Multiphase Flow **35**(3), 227 (2009)
34. G. Tryggvason, B. Bunner, A. Esmaeeli, D. Juric, N. Al-Rawahi, W. Tauber, J. Han, S. Nas, Y.J. Jan, J. Comput. Phys. **169**(2), 708 (2001)
35. C.S. Peskin, Acta Numerica **11**, 479–517 (2002)
36. J. van der Walls, J. Stat. Phys. **20**(2), 197 (1979)
37. D. Anderson, G. McFadden, A. Wheeler, Annu. Rev. Fluid Mech. **30**, 139 (1998)
38. J.G. Kirkwood, F.P. Buff, J. Chem. Phys. **17**(3), 338 (1949)
39. M.R. Swift, W.R. Osborn, J.M. Yeomans, Phys. Rev. Lett. **75**, 830 (1995)
40. M.R. Swift, E. Orlandini, W.R. Osborn, J.M. Yeomans, Phys. Rev. E **54**, 5041 (1996)
41. A.J. Briant, A.J. Wagner, J.M. Yeomans, Phys. Rev. E **69**, 031602 (2004)
42. A.J. Briant, J.M. Yeomans, Phys. Rev. E **69**, 031603 (2004)
43. C. Semprebon, T. Krüger, H. Kusumaatmaja, Phys. Rev. E **93**(3), 033305 (2016)
44. T. Lee, C.L. Lin, J. Comput. Phys. **206**(1), 16 (2005)
45. A. Mazloomi M., S.S. Chikatamarla, I.V. Karlin, Phys. Rev. E **92**(2), 023308 (2015)
46. G. Gompper, S. Zschocke, Europhys. Lett. **16**(8), 731 (1991)

47. V.M. Kendon, M.E. Cates, I. Pagonabarraga, J.C. Desplat, P. Bladon, J. Fluid Mech. **440**, 147 (2001)
48. A. Wagner, Q. Li, Physica A Stat. Mech. Appl. **362**(1), 105 (2006)
49. T. Lee, P.F. Fischer, Phys. Rev. E **74**, 046709 (2006)
50. T. Seta, K. Okui, JFST **2**(1), 139 (2007)
51. C.M. Pooley, K. Furtado, Phys. Rev. E **77**, 046702 (2008)
52. Z. Guo, C. Zheng, B. Shi, Phys. Rev. E **65**, 46308 (2002)
53. K. Connington, T. Lee, J. Mech. Sci. Technol. **26**(12), 3857 (2012)
54. D. Jamet, D. Torres, J. Brackbill, J. Comput. Phys. **182**(1), 262 (2002)
55. A.J. Wagner, Int. J. Modern Phys. B **17**(01n02), 193 (2003)
56. T. Inamuro, N. Konishi, F. Ogino, Comput. Phys. Commun. **129**(1), 32 (2000)
57. D.J. Holdych, D. Rovas, J.G. Georgiadis, R.O. Buckius, Int. J. Modern Phys. C **09**(08), 1393 (1998)
58. H. Kusumaatmaja, J. Léopoldés, A. Dupuis, J. M. Yeomans, Europhys. Lett. **73**(5), 740 (2006)
59. J.W. Cahn, J. Chem. Phys. **66**(8), 3667 (1977)
60. K.F. Riley, M.P. Hobson, S.J. Bence, *Mathematical Methods for Physics and Engineering (3rd edition): A Comprehensive Guide* (CUP, Cambridge, 2006)
61. H. Kusumaatmaja, J.M. Yeomans, in *Simulating Complex Systems by Cellular Automata*, ed. by J. Kroc, P.M. Sloot, A.G. Hoekstra, Understanding Complex Systems (Springer, New York, 2010), chap. 11, pp. 241–274
62. A. Lamura, G. Gonnella, J.M. Yeomans, Europhys. Lett. **45**(3), 314 (1999)
63. Q. Li, A.J. Wagner, Phys. Rev. E **76**(3), 036701 (2007)
64. J.W. Cahn, C.M. Elliott, A. Novick-Cohen, Eur. J. Appl. Math. **7**, 287 (1996)
65. J. Zhu, L.Q. Chen, J. Shen, V. Tikare, Phys. Rev. E **60**, 3564 (1999)
66. H. Kusumaatmaja, E.J. Hemingway, S.M. Fielding, J. Fluid Mech. **788**, 209 (2016)
67. J.J. Huang, C. Shu, Y.T. Chew, Phys. Fluids **21**(2) (2009)
68. X. Shan, H. Chen, Phys. Rev. E **47**(3), 1815 (1993)
69. X. Shan, G. Doolen, J. Stat. Phys. **81**(1), 379 (1995)
70. J. Zhang, F. Tian, Europhys. Lett. **81**(6), 66005 (2008)
71. N.S. Martys, H. Chen, Phys. Rev. E **53**(1), 743 (1996)
72. X. Shan, H. Chen, Phys. Rev. E **49**(4), 2941 (1994)
73. M.C. Sukop, D.T. Thorne, *Lattice Boltzmann Modeling: An Introduction for Geoscientists and Engineers* (Springer, New York, 2006)
74. M. Sbragaglia, R. Benzi, L. Biferale, S. Succi, K. Sugiyama, F. Toschi, Phys. Rev. E **75**(026702), 1 (2007)
75. M. Sbragaglia, H. Chen, X. Shan, S. Succi, Europhys. Lett. **86**(2), 24005 (2009)
76. J. Bao, L. Schaefer, Appl. Math. Model. **37**(4), 1860 (2013)
77. D. Lycett-Brown, K.H. Luo, Phys. Rev. E **91**, 023305 (2015)
78. P. Yuan, L. Schaefer, Phys. Fluids **18**(042101), 1 (2006)
79. A. Kuzmin, A. Mohamad, S. Succi, Int. J. Mod. Phys. C **19**(6), 875 (2008)
80. R. Benzi, L. Biferale, M. Sbragaglia, S. Succi, F. Toschi, Phys. Rev. E **74**(2), 021509 (2006)
81. Z. Yu, L.S. Fan, Phys. Rev. E **82**(4), 046708 (2010)
82. X. Shan, Phys. Rev. E **81**(4), 045701 (2010)
83. M. Sega, M. Sbragaglia, S.S. Kantorovich, A.O. Ivanov, Soft Matter **9**(42), 10092 (2013)
84. X. Shan, G. Doolen, Phys. Rev. E **54**(4), 3614 (1996)
85. J. Yang, E.S. Boek, Comput. Math. Appl. **65**(6), 882 (2013)
86. H. Liu, Y. Zhang, A.J. Valocchi, Phys. Fluids **27**(5), 052103 (2015)
87. H. Huang, D.T. Thorne, M.G. Schaap, M.C. Sukop, Phys. Rev. E **76**(6), 066701 (2007)
88. S. Chibbaro, Eur. Phys. J. E **27**(1), 99 (2008)
89. F. Jansen, J. Harting, Phys. Rev. E **83**(4), 046707 (2011)
90. I. Ginzburg, G. Wittum, J. Comp. Phys. **166**(2), 302 (2001)
91. A. Kupershtokh, D. Medvedev, D. Karpov, Comput. Math. Appl. **58**(5), 965 (2009)
92. R. Benzi, M. Sbragaglia, S. Succi, M. Bernaschi, S. Chibbaro, J. Chem. Phys. **131**(10), 104903 (2009)

93. R. Benzi, M. Bernaschi, M. Sbragaglia, S. Succi, Europhys. Lett. **91**(1), 14003 (2010)
94. S. Chibbaro, G. Falcucci, G. Chiatti, H. Chen, X. Shan, S. Succi, Phys. Rev. E **77**(036705), 1 (2008)
95. Z. Guo, C. Zheng, B. Shi, Phys. Rev. E **83**, 036707 (2011)
96. D. Chiappini, G. Bella, S. Succi, F. Toschi, S. Ubertini, Commun. Comput. Phys. **7**, 423 (2010)
97. A. Kuzmin, A. Mohamad, Comp. Math. Appl. **59**, 2260 (2010)
98. T. Inamuro, T. Ogato, S. Tajima, N. Konishi, J. Comp. Phys. **198**, 628 (2004)
99. H. Zheng, C. Shu, Y. Chew, J. Comput. Phys. **218**(1), 353 (2006)
100. A. Mazloomi M, S.S. Chikatamarla, I.V. Karlin, Phys. Rev. Lett. **114**, 174502 (2015)
101. A. Kuzmin, M. Januszewski, D. Eskin, F. Mostowfi, J. Derksen, Chem. Eng. J. **171**, 646 (2011)
102. A. Kuzmin, M. Januszewski, D. Eskin, F. Mostowfi, J. Derksen, Chem. Eng. J. **178**, 306 (2011)
103. A. Kuzmin, Multiphase simulations with lattice Boltzmann scheme. Ph.D. thesis, University of Calgary (2010)
104. M.L. Porter, E.T. Coon, Q. Kang, J.D. Moulton, J.W. Carey, Phys. Rev. E **86**(3), 036701 (2012)
105. Q. Kang, D. Zhang, S. Chen, Adv. Water Resour. **27**(1), 13 (2004)
106. Z. Yu, H. Yang, L.S. Fan, Chem. Eng. Sci. **66**(14), 3441 (2011)
107. M. Monteferrante, S. Melchionna, U.M.B. Marconi, J. Chem. Phys. **141**(1), 014102 (2014)
108. K. Premnath, J. Abraham, J. Comput. Phys. **224**, 539 (2007)
109. Z.H. Chai, T.S. Zhao, Acta. Mech. Sin. **28**(4), 983 (2012)
110. D. Zhang, K. Papadikis, S. Gu, Int. J. Multiphas. Flow **64**, 11 (2014)
111. K. Yang, Z. Guo, Sci. Bull. **60**(6), 634 (2015)
112. Y.Q. Zu, S. He, Phys. Rev. E **87**(4), 043301 (2013)
113. H. Liang, B.C. Shi, Z.H. Chai, Phys. Rev. E **93**(1), 013308 (2016)
114. Y. Fu, S. Zhao, L. Bai, Y. Jin, Y. Cheng, Chem. Eng. Sci. **146**, 126 (2016)
115. H. Chen, B.M. Boghosian, P.V. Coveney, M. Nekovee, Proc. R. Soc. Lond. A **456**, 2043 (2000)
116. M. Nekovee, P.V. Coveney, H. Chen, B.M. Boghosian, Phys. Rev. E **62**(6), 8282 (2000)
117. S. Bogner, U. Rüde, Comput. Math. Appl. **65**(6), 901 (2013)
118. D. Anderl, S. Bogner, C. Rauh, U. Rüde, A. Delgado, Comput. Math. Appl. **67**(2), 331 (2014)
119. S. Bogner, R. Ammer, U. Rüde, J. Comput. Phys. **297**, 1 (2015)
120. M. Gross, F. Varnik, Int. J. Mod. Phys. C **25**(01), 1340019 (2013)
121. X. Frank, P. Perré, H.Z. Li, Phys. Rev. E **91**(5), 052405 (2015)
122. Q. Li, Q.J. Kang, M.M. Francois, A.J. Hu, Soft Matter **12**(1), 302 (2015)
123. C. Pan, M. Hilpert, C.T. Miller, Water Resour. Res. **40**(1), W01501 (2004)
124. E.S. Boek, M. Venturoli, Comput. Math. Appl. **59**(7), 2305 (2010)
125. J. Onishi, A. Kawasaki, Y. Chen, H. Ohashi, Comput. Math. Appl. **55**(7), 1541 (2008)
126. A.S. Joshi, Y. Sun, Phys. Rev. E **79**(6), 066703 (2009)
127. T. Krüger, S. Frijters, F. Günther, B. Kaoui, J. Harting, Eur. Phys. J. Spec. Top. **222**(1), 177 (2013)
128. K.W. Connington, T. Lee, J.F. Morris, J. Comput. Phys. **283**, 453 (2015)
129. Q. Luo, Z. Guo, B. Shi, Phys. Rev. E **87**(063301), 1 (2013)
130. Z. Yu, O. Hemminger, L.S. Fan, Chem. Eng. Sci. **62**, 7172 (2007)
131. H. Liu, Y. Zhang, J. Appl. Phys. **106**(3), 1 (2009)
132. T. Munekata, T. Suzuki, S. Yamakawa, R. Asahi, Phys. Rev. E **88**(5), 052314 (2013)
133. R. Ledesma-Aguilar, D. Vella, J.M. Yeomans, Soft Matter **10**(41), 8267 (2014)
134. D. Sun, M. Zhu, S. Pan, D. Raabe, Acta Mater. **57**(6), 1755 (2009)
135. R. Rojas, T. Takaki, M. Ohno, J. Comput. Phys. **298**, 29 (2015)
136. P.R. Di Palma, C. Huber, P. Viotti, Adv. Water Resour. **82**, 139 (2015)
137. G. Gonnella, E. Orlandini, J.M. Yeomans, Phys. Rev. E **58**, 480 (1998)
138. Q. Du, C. Liu, X. Wang, J. Comput. Phys. **198**(2), 450 (2004)

139. J.S. Lowengrub, A. Rätz, A. Voigt, Phys. Rev. E **79**, 031926 (2009)
140. C. Denniston, E. Orlandini, J.M. Yeomans, Phys. Rev. E **63**, 056702 (2001)
141. J. Qian, C. Law, J. Fluid Mech. **331**, 59 (1997)
142. N. Ashgriz, J. Poo, J. Fluid Mech. **221**, 183 (1990)
143. C. Rabe, J. Malet, F. Feuillebois, Phys. Fluids **22**(047101), 1 (2010)
144. D. Lycett-Brown, K. Luo, R. Liu, P. Lv, Phys. Fluids **26**(023303), 1 (2014)
145. T. Inamuro, S. Tajima, F. Ogino, Int. J. Heat Mass Trans. **47**, 4649 (2004)
146. A. Moqaddam, S. Chikatamarla, I. Karlin, Phys. Fluids **28**(022106), 1 (2016)
147. A.E. Komrakova, D. Eskin, J.J. Derksen, Phys. Fluids **25**(4), 042102 (2013)
148. O. Shardt, J.J. Derksen, S.K. Mitra, Langmuir **29**, 6201 (2013)
149. O. Shardt, S.K. Mitra, J.J. Derksen, Langmuir **30**, 14416 (2014)
150. H. Kusumaatmaja, C.M. Pooley, S. Girardo, D. Pisignano, J.M. Yeomans, Phys. Rev. E **77**, 067301 (2008)
151. J. Murison, B. Semin, J.C. Baret, S. Herminghaus, M. Schröter, M. Brinkmann, Phys. Rev. Appl. **2**, 034002 (2014)
152. A.A. Darhuber, S.M. Troian, Annu. Rev. Fluid Mech. **37**(1), 425 (2005)
153. H. Gau, S. Herminghaus, P. Lenz, R. Lipowsky, Science **283**(5398), 46 (1999)
154. M. Brinkmann, R. Lipowsky, J. Appl. Phys. **92**(8), 4296 (2002)
155. H.P. Jansen, K. Sotthewes, J. van Swigchem, H.J.W. Zandvliet, E.S. Kooij, Phys. Rev. E **88**, 013008 (2013)
156. A. Dupuis, J. Léopoldés, D.G. Bucknall, J.M. Yeomans, Appl. Phys. Lett. **87**(2), 024103 (2005)
157. S. Wang, T. Wang, P. Ge, P. Xue, S. Ye, H. Chen, Z. Li, J. Zhang, B. Yang, Langmuir **31**(13), 4032 (2015)
158. D. Quéré, Annu. Rev. Mater. Res. **38**(1), 71 (2008)
159. W. Barthlott, C. Neinhuis, Planta **202**(1), 1 (1997)
160. J. Bico, C. Marzolin, D. Quéré, Europhys. Lett. **47**(2), 220 (1999)
161. A. Tuteja, W. Choi, M. Ma, J.M. Mabry, S.A. Mazzella, G.C. Rutledge, G.H. McKinley, R.E. Cohen, Science **318**(5856), 1618 (2007)
162. A.B.D. Cassie, S. Baxter, Trans. Faraday Soc. **40**, 546 (1944)
163. C.H. Choi, C.J. Kim, Phys. Rev. Lett. **96**, 066001 (2006)
164. R.N. Wenzel, J. Phys. Colloid Chem. **53**(9), 1466 (1949)
165. F. Diotallevi, L. Biferale, S. Chibbaro, G. Pontrelli, F. Toschi, S. Succi, Euro. Phys. J. Special Topics **171**(1), 237 (2009)